Photoluminescence, photophysics, and photochemistry of the V_B^- defect in hexagonal boron nitride

Jeffrey R. Reimers[1,2], Jun Shen,[3] Mehran Kianinia,[2] Carlo Bradac,[2] Igor Aharonovich,[2] Michael J. Ford,[2] and Piotr Piecuch[3,4]

[1] *International Centre for Quantum and Molecular Structures and Department of Physics, Shanghai University, Shanghai 200444, China.*

[2] *University of Technology Sydney, School of Mathematical and Physical Sciences, Ultimo, New South Wales 2007, Australia.*

[3] *Department of Chemistry, Michigan State University, East Lansing, Michigan 48824, United States of America.*

[4] *Department of Physics and Astronomy, Michigan State University, East Lansing, Michigan 48824, United States of America.*

Email: jeffrey.reimers@uts.edu.au; jun@chemistry.msu.edu; mike.ford@uts.edu.au; piecuch@chemistry.msu.edu

Abstract

Extensive photochemical and spectroscopic properties of the V_B^- defect in hexagonal boron nitride are calculated, concluding that the observed photoemission associated with recently observed optically-detected magnetic resonance is most likely of $(1)^3E'' \rightarrow (1)^3A_2'$ origin. Rapid intersystem crossing from the defect's triplet to singlet manifolds explains the observed short excited-state lifetime and very low quantum yield. New experimental results reveal smaller intrinsic spectral bandwidths than previously recognized, interpreted in terms spectral narrowing and zero-phonon-line shifting induced by the Jahn-Teller effect. Different types of computational methods are applied to map out the complex triplet and singlet defect manifolds, including the doubly ionised formulation of the equation-of-motion coupled-cluster theory that is designed to deal with the open-shell nature of defect states, and mixed quantum-mechanics/molecular-mechanics schemes enabling 5763-atom simulations. Two other energetically feasible spectral assignments from amongst the singlet and triplet manifolds are considered, but ruled out based on inappropriate photochemical properties.

I. INTRODUCTION

Hexagonal boron nitride (h-BN) has become of great interest following the 2016 discovery of single-photon emission from atom-like defects in the material [1-4]. Of significance is the recent observation of optically detected magnetic resonance (ODMR) associated with (at least) two types of h-BN defects [5, 6]. This could enhance the use of h-BN defects in nanophotonic applications [7-10]. Much effort has been devoted to determining the chemical nature of different defects [11], including broad-based scans of possibilities [4] and detailed studies [12-14]. Prior to the detection of ODMR, no defect displaying photoluminescence had been assigned, only defects with observed magnetic properties [15, 16]; defects exhibiting ODMR facilitate measurement of both the magnetic and photoluminescence properties. For one defect displaying ODMR [5], comparison of the observed magnetic properties to expectations [12] strongly suggested that the ODMR arises from the V_B^- defect (a charged boron vacancy), an interpretation that was quickly supported quantitatively [17, 18]. Calculations have predicted that V_B^- has a triplet ground state [12, 19], with a variety of low-energy triplet excited states predicted, within likely error limits, to have energies consistent with the observed photoemission energy [17, 18].

The low-energy triplet manifold of V_B^- is very complex, and subtle changes in its capture by different computational methods can have profound consequences on the predicted spectra. A significant issue is that spectra predicted for the lowest-energy transitions are very broad and inconsistent with the experimental observations [18]. Further, the observed spectrum corresponds to an ensemble of emitters at high temperature and could therefore be considerably broader than that for a single emitter, as modelled in the calculations. A key unexplained property of the observed emission is that it is very weak, indicating that some, currently unknown, photochemical process(es) must act to reduce the quantum yield upon photoexcitation. Intersystem crossing to the singlet manifold is a possible mechanism for this reduction in quantum yield, raising the possibility that the observed emission occurs from within the singlet manifold. We also note that previous estimates of spectral bandwidth based on calculations have assumed that the spectra obey simple relationships such as those expected based on Huang-Rhys factors depicting transitions between non-interacting, non-degenerate electronic states. We remark that, in contrast, V_B^- is intrinsically a Jahn-Teller system involving many doubly degenerate electronic states supporting multiple isomeric forms, with the lowest-energy excited states also involving unmapped avoided crossings in the Franck-Condon region [18]. To understand how V_B^- sustains ODMR, in this work we address a series of outstanding challenges [18]:

- Improved measurements of spectral bandshape are obtained, including measurements of its temperature dependence.

- Accurate transition-energy calculations are obtained, with boundable error estimates, for both the singlet and triplet manifolds.
- Accurate calculations of photoluminescence band shapes and intensities are performed, taking into effect long-range acoustic phonons, the Jahn-Teller effect, and the Herzberg-Teller effect.
- Useful estimates of many photochemical reaction rates are obtained, taking into account isomerization and other reaction transition states, as well as the influence of Jahn-Teller and other conical intersections.
- Verification of the consistency of our computational predictions against experimental spectroscopy measurement from samples showing the ODMR photo-dynamics, focusing on transition energies, bandwidths, emission lifetimes, quantum yields, and their temperature dependencies.

The V_B^- defect has intrinsic D_{3h} local point-group symmetry, when isolated within the bulk of an h-BN sheet [12, 19-21]. All modelling reported herein is applied to the model compounds shown in Fig. 1 that can all display this symmetry. The observed ODMR properties are suggestive of D_{3h} symmetry, although some observed properties require slight symmetry lowering [5]. Note that V_B^- defects are created by neutron/ion irradiation of h-BN, which can lead to damage in the crystalline structure and thus to lowering of symmetry. To date, symmetry lowering induced by local strain, [17] or by the defect being located at the edge [11, 22, 23] of a h-BN sheet [18], have been considered. Whereas some calculated properties may change dramatically based on these variations, the basic spectral properties are insensitive to such effects—which at any rate tend to generally broaden the spectra rather than to narrow them [18].

We have previously considered other defects in h-BN, seeking calibrated computational quantum chemistry methods and the conditions in which these methods can deliver accurate results [24]. We identified a number of issues, summarised in Table I, that must be addressed in any computational work to model reliably the defect and its properties. A critical aspect is that many of the states of interest are open-shell in nature. We remark that none of the widely-used density functional theory (DFT) and *ab initio* wavefunction methods in traditional software packages are capable of accurately characterizing all defect properties of interest. The development of a reliable computational protocol for the prediction of defect properties should thus stem from the thorough, comparative analysis of a wider variety of feasible approaches than that considered in our previous work [24], including newer generations of *ab initio* quantum chemistry methods.

The electronic-structure computational methods used are listed in the Methods section, with their strengths and limits of applicability being discussed in the Supplemental Material (SM) [25]

Section S1 and summarised in Table II. Most methods are well known, but we add one new approach that is particularly well-suited to address defect spectroscopy and the singlet manifold of V_B^- specifically. This is a coupled-cluster (CC) method utilising the equation-of-motion (EOM) formalism (EOMCC) in its double-ionisation-potential (DIP) version, [26-31] which involves removing two electrons from a reference wavefunction in order to create the electronic states of interest. The DIP-EOMCC approach provides an accurate description of open-shell character, assuming that the reference wavefunction is predominantly closed-shell in nature. We find it to be more suitable than traditional ways of treating open-shell systems such as complete-active-space self-consistent field (CASSCF) [32-34] and its extension, multi-reference configuration interaction (MRCI) [35], for it is more conducive to expansion towards the exact answer and hence the estimation of likely error bounds. For the triplet manifold, its ground state appears mostly single-reference in nature and so we apply traditional particle conserving EOMCC singles and doubles [36] (EOMCCSD) and time-dependent density-functional theory [37] (TDDFT) approaches. Another significant aspect of the Methods, applied to model 10-ring and larger compounds, is the use of mixed quantum-mechanics/molecular-mechanics (QM/MM) approaches utilizing, in the MM part, an AMBER [38] force field fitted to reproduce DFT-calculated properties of h-BN [39].

Simulation of spectra of defects in h-BN is usually made based on the Huang-Rhys approximation [40] or its variants. The basic model involves five core approximations, any or all of which are likely to fail when applied to defect spectroscopy [11]. Notably, this approach is inapplicable at conical intersections. General simulation codes pertinent to the Jahn-Teller effect are not available. We herein apply standard methods to model systems developed to mimic the key features of the triplet and singlet manifolds revealed by the electronic structure calculations. A key quantity of interest is the emission reorganisation energy λ^E, which we determine through the measurement and interpretation of experimental photoluminescence spectra. In semiclassical models such as the Huang-Rhys model, λ^E equals the difference in energy on the final electronic state after a vertical transition (i.e., transition without change in defect geometry induced by interactions with phonons) from the adiabatic minimum of the state has taken place. Perception of the observed photoluminescence spectra as being too narrow compared to expectations have been based on this assumption. By directly simulating spectra using a Jahn-Teller model, we investigate the dramatic effects possible, including spectral narrowing.

We also calculate emission lifetimes and competitive photochemical reaction rates. These include: rates for intersystem crossing reactions between the triplet and singlet manifolds, as well as rates for internal-conversion involving both avoided crossings (forming traditional transition states) and symmetry-forbidden processes at conical intersections. Only simple model calculations are reported, accurate to about an order of magnitude, but these are sufficient to capture processes

occurring from sub-ps to ms or longer timescales that are relevant to the experimental observations and estimated photoemission lifetimes.

The results show how detailed knowledge of both the singlet and triplet manifolds, as well as the operation of the Jahn-Teller effect, is required to interpret the observed photoluminescence of V_B^-. In particular, three transitions, one in the singlet manifold and two in the triplet manifold, are pursued in detail concerning the likelihood that they could be responsible for the observed emission. We also measure improved defect spectra for comparison.

II. METHODS

A. Material fabrication

The analysed samples were hBN flakes, neutron irradiated in the Triga Mark I IPR-R1 nuclear reactor (CDTN, Brazil), with a thermal flux of 4×10^{12} n cm^{-2} s^{-1} for 16 h, with a resulting integrated dose of approximately 2.3×10^{18} n cm^{-2}. All the samples were irradiated in cadmium capsules to block thermal neutrons and let the most energetic neutrons irradiate the sample [5].

B. Spectroscopy measurements

Spectroscopy measurements were carried out on a lab-built confocal microscope. A 532-nm, continuous-wave, solid-state laser (Gem 532TM; Laser Quantum Ltd.) was used as the excitation source. Light was focused onto the sample via a high numerical aperture (NA 0.9) air objective (Plan Fluor Epi P 100 ×; Nikon). Emission from the sample was collected in reflection, filtered through a long pass filter (transmission >560 nm) to suppress the excitation laser and sent into a multimode fibre. The collected signal could then be sent either to an avalanche photodiode (SPCM-AQRH-W4-FC; Excelitas Technologies) or a spectrometer with a 300 g/mm grating (SpectraPro Monochromator Acton SP2300), mounting a thermoelectric cooled (75 ºC) CCD camera (Pixis Camera 256; Princeton Instruments). Spectra were acquired both at liquid nitrogen (77 K) and at room temperature (295 K).

C. Electronic structure computations

We utilise a wide range of computational methods, for which strengths and weaknesses are discussed in SM Section S1 and summarised in Table II [26-31, 35, 36, 41-70]. These methods include:

(1) CAM-B3LYP [57-59], as an example of an appropriate entry-level DFT methodology [24, 70], as well as the commonly used HSE06 functional [55, 56], both relying on the time-dependent formulation of DFT (TDDFT) [37] to determine excited electronic states. The D3(BJ) dispersion correction [71] is applied to all systems involving multiple h-BN layers.

(2) the standard single-reference coupled-cluster (CC) theory [61-63, 65] with singly and doubly excited clusters (CCSD) [64] combined with a quasi-perturbative non-iterative correction due to connected triply excited clusters defining the widely used CCSD(T) approximation [66], along with the equation-of-motion (EOM) extension of CCSD to excited states abbreviated as EOMCCSD [36].

(3) The double-ionisation-potential (DIP) extension of the EOMCC formalism [26-31], abbreviated as DIP-EOMCC, using both the basic 3-hole–1-particle (3*h*-1*p*) [28-31] truncation and the highest currently implemented [30, 31] 4*h*-2*p* level, which belong to a broader category of particle non-conserving EOMCC theories [30, 31, 65]. In the case of the 4*h*-2*p* truncation, we use active orbitals to select the dominant 4*h*-2*p* components to reduce computational costs [30, 31]. These approaches allow one to determine singlet and triplet manifolds of open-shell systems that can formally be obtained by removing two electrons from the parent closed-shell cores (an operation generating the appropriate multi-configurational reference space within a single-reference framework), while relaxing the remaining electrons to capture dynamic electron correlations.

(4) The CASSCF approach [32-34], which is a conventional multi-reference technique for capturing static electron correlation effects, and

(5) Two different ways of correcting CASSCF calculations for dynamic correlations missing in CASSCF, including (CASPT2) [67, 68], which uses the second-order multi-reference perturbation theory, and one of the variants of MRCI [35], which incorporates singly and doubly excited configuration state functions from a CASSCF reference, followed by the internal contraction and adding quasi-degenerate, relaxed-reference, Davidson corrections.

(6) Application of the ONIOM [72, 73] approach to QM/MM to extend model sizes. This uses an AMBER [38] force field for the MM part, parameterised to mimic CAM-B3LYP/D3 results [39]. Two rings are retained in the QM part only, leading to very computationally efficient calculations.

All DFT and EOMCCSD calculations and CCSD geometry optimizations were performed using Gaussian-16 [74]. All CASSCF, CASPT2, CCSD(T) and MRCI calculations were performed using MOLPRO [75]. All DIP-EOMCC calculations were carried out using standalone in-house codes [30, 31] interfaced with the integral and SCF routines in GAMESS [76, 77]. In the initial CC stages prior to DIP-EOMCC diagonalizations, these codes rely upon the spin-integrated CCSD routines available in GAMESS as well [78]. In all correlated calculations, the core orbitals correlating with the 1*s* shells of the B and N atoms were kept frozen and the spherical components of *d* and *f* basis functions, if present in the basis set, were employed throughout. The basis sets used were STO-3G [79], 6-31G [80], 6-31G* [80], and cc-pVTZ [81]. Self-consistent reaction field calculations, modelling a defect embedded deep within the h-BN bulk, are performed using the polarizable continuum model [82]

using Gaussian-16, with the low-frequency bulk dielectric constant of h-BN is taken to be 5.87, whilst the high-frequency value is taken as 4.32.

D. Observed spectral fitting

Observed spectra were fitted to a thermal Huang-Rhys model using the THRUP programme [83, 84]. This allows spectra to be simulated for multiple electronic states interacting through multiple vibrational modes using either diabatic or adiabatic representations. It is often used to model the complex scenarios that arise during natural [85, 86] and artificial [87] photosynthetic systems. In this application, it is used simply to model spectra within the Huang-Rhys model. Full details are given in SM Section S2.

E. Spectral simulation

Absorption and emission spectra for assumed non-degenerate states are evaluated using Huang-Rhys-type schemes, perhaps extended to include curvilinear coordinates, Herzberg-Teller effects, and/or approximate inclusion of the Duschinsky matrix relating the initial-state and final-state normal modes using the DUSHIN software [88]. For systems of 10 rings or more, only the basic Huang-Rhys model is used, driven using analytical Hessian matrices written by Gaussian-16 into its formatted checkpoint files (use instead of the associated listed normal modes as their use was found to lead to significant errors). Methods beyond the above such Huang-Rhys-type approaches that include the Jahn-Teller effect are described in detail in SM Sect S8.

F. Photophysical and photochemical rate simulations

All methods used are traditional applications of either transition-state theory or adiabatic electron-transfer theory and are described in detail in SM Section S9 [89-97].

III. RESULTS

A. Measurement and interpretation of h-BN photoluminescence

Fig. 2 shows the original [5] photoemission spectrum observed from h-BN defects that display ODMR with a zero-field splitting parameter in the ground state D_{gs} of 3.5 GHz, along with two newly recorded spectra. All new spectra are corrected for the response functions of the diffraction grating and detector, and were obtained at either 295 K or 77 K. As previously observed [5], such spectra

show weak intensity, indicating low quantum yield, subsequent to photo-absorption. Also, the spectra arise from multiple emitters, distinct from the single-photon emitters commonly studied in h-BN [1-4]. The spectra are presented as the bandshape function $E(\nu)/\nu^3 \propto \lambda^5 E(\lambda)$ that display the intrinsic properties of the defect, allowing the shapes and bandwidths of photoemitters at different wavelengths to be directly compared. Maximum emission occurs at vertical transition energies ΔE_v^E of 1.5–1.6 eV (830–770 nm). The quantitative analysis of the effect of site inhomogeneity on the observed spectral bandshapes is not currently possible.

In SM, these and more spectra are presented and crudely analysed based on the assumption that each spectrum arises only from a single emitter. This assumption is known not be applicable to the present spectra as they comprise an ensemble of emissions observed from different defects. Each defect could have slightly different character in terms of its emission energy and/or spectral distribution, and hence the observed spectra become broadened and could have their shapes changed in unpredictable ways. Hence the analyses presented depict upper bounds for the reorganisation energy λ^E associated with photoemission, and the associated estimates of the energies E_{00} of the associated zero-phonon lines (ZPL) may also be significantly in error, especially if the ZPL lies in the high-frequency tail of a spectrum rather than near its maxima. Nevertheless, a traditional approach is taken in which each spectrum is represented using a set of Huang-Rhys factors depicting transitions between non-degenerate electronic states. This results in the spectral interpretation: $E_{00} = (1.61 \pm 0.03)$ eV and $\lambda^E < 0.05$ eV. Weaker emitters are apparent in the spectra, and in principle these could range in energy from 1.3 to 2.0 eV, based on the available information. The reorganisation energy could also be significantly smaller than the upper bound of 0.05 eV; indeed, the new spectra reported herein are significantly narrower than that originally reported (Fig. 2), reflecting more the intrinsic properties of single defects. For comparison, traditional bright h-BN single-photon emitters have been categorised into "Group-1" emitters with reorganisation energies of 0.06–0.16 eV and "Group-2" emitters with 0.015–0.030 eV [11].

Two features of this analysis are important. First, the determined reorganisation energies do not include contributions from the acoustic phonons that determine the width of the ZPL, whereas the calculations presented later include all contributions. Second, the V_B^- defect has inherent 3-fold symmetry and hence many of its electronic states will be doubly degenerate and therefore subject to the Jahn-Teller effect. In SM Section S2, we show that this effect can considerably reduce calculated spectral bandwidths, masking the effect of the reorganisation energy. Indeed, both effects can place the ZPL in the far blue-region of the observed spectral tail, as illustrated in Fig. 2. As a result of both effects, the above traditional analysis could significantly underestimate the actual reorganisation energy.

B. Overview of key orbital energy levels, electronic states, and the Jahn-Teller effect

If a boron atom is removed from a pristine h-BN layer to make V_B^-, "dangling bonds" appear at each neighbouring nitrogen atom in both the σ and π electronic systems, making for six intrinsic orbital levels associated with the defect. We employ many different computational methods, all of which indicate that these six levels sit in the band gap of the h-BN, as sketched in Fig. 3, that are occupied by 10 electrons, consistent with other calculations [12, 17, 18]. Varying occupancy, as depicted in Fig. 4, results in many low-energy singlet and triplet defect states, most of which are open-shell in nature. States always arise as mixtures of such configurations, but nevertheless we name them based on the configuration that is the most dominant; this labelling is therefore *diabatic* in nature and hence not subject to the discontinuities that occur at Jahn-Teller and other conical intersections, or the anharmonic effects that give rise to transition states.

We optimize the geometries of identified excited states, seeking potential-energy minima. Mostly, these optimizations are constrained to depict C_{2v} symmetry; sometimes optimized geometries with D_{3h} symmetry result, and sometimes vibrational analyses (or other means) indicate that the C_{2v} structures are transition states rather than minima on the complete potential-energy surface. At D_{3h} geometries, states are usually labelled using labels appropriate to D_{3h}, with structures at C_{2v} geometries similarly named. State names based on these two labelling schemes are defined in Fig. 4 for the configurations of greatest interest.

Four relevant, doubly degenerate states at D_{3h} geometries are: $(1)^1E'$, $(1)^1E''$, $(1)^3E'$, and $(1)^3E''$. These must undergo Jahn-Teller distortions that reduce their symmetry to C_{2v}. Each component of a doubly degenerate state has the same label in D_{3h} symmetry, but individual labels in C_{2v}, e.g., $(1)^3E''$ splits into $(1)^3A_2$ and $(1)^3B_1$, whilst $(1)^3E'$ splits into $(1)^3A_1$ and $(1)^3B_2$. Note that we use C_{2v} standard axis conventions for planar molecules throughout [98, 99] (otherwise "B_1" and "B_2" would be interchanged). Physically, this effect produces "tricorn Mexican hat" shaped potential-energy surfaces as a function of some e' doubly degenerate vibrational coordinate, as sketched in Fig. 5. A conical intersection appears at the central undistorted D_{3h} geometry, with three equivalent local minima, defining symmetrically equivalent isomers of the defect, separated by three symmetrically equivalent transition states, all of C_{2v} symmetry, appearing on axes separated from each other by 120°. Away from these axes, the symmetry is reduced to C_s. The example shown in Fig. 5 pertains to $(1)^1E'$; its components in C_{2v} symmetry are $(1)^1A_1$ and $(1)^1B_2$, with calculations predicting that $(1)^1B_2$ forms the local minima (in this case, defining the singlet ground state), whilst $(1)^1A_1$ provides transition states that are unstable to distortion in a b_2 vibrational mode. As the figure shows, the three isomers support short N–N interaction distances within the defect, located along each

of the three crystallographic axes, whilst the analogous distances are lengthened in their interconnecting transition states. Note that the derivative discontinuity manifested at the conical intersection causes the symmetry to change abruptly as it is crossed along one of the three C_{2v} orientations.

The basic tricorn Mexican hat depicted in Fig. 5 may be distorted symmetrically, through avoided crossings or other interactions with nearby states, as well as distorted asymmetrically through strain effects. Although only briefly discussed herein, out-of-plane distortions may be introduced as well as the in-plane distortions manifested in the figure. The shortening of neighbouring N–N distances apparent in the figure highlights that defects rearrange their structure to maximise strong chemical bonding effects, and that this is state-dependent, for it relies on the electron occupancy and overall spin. Model compounds containing only a single ring (Fig. 1) may over-accentuate this [24].

If the transition-state barrier displayed in Fig. 5 is large compared to the associated vibrational energy spacings—or if distortions induced by interactions with other states or external forces are large—then just one single well (isomer) of the tricorn structure needs to be considered in calculating spectroscopic and other properties, known as the *static* Jahn-Teller effect. Huang-Rhys-type models may provide realistic predictions of spectral bandshapes in this scenario. Alternatively, if the transition-state is of low energy, then quantum interference occurs between the vibronic energy levels in each of the three wells, possibly controlling spectral lineshapes. This is known as the *dynamic* Jahn-Teller effect and has the consequence that the properties of the defect cannot be described purely in terms of those of just one of its isomeric forms. Note that all spectroscopic simulations reported herein pertaining to the Jahn-Teller effect are performed using a diabatic basis. They include both lower and upper adiabatic surfaces, never introducing Born-Oppenheimer approximation shown in Fig. 5 and the isomeric forms that it reveals.

C. Electronic-structure calculations for the triplet manifold

Key calculated properties of the triplet-state manifold for the V_B^- defect of h-BN are presented in Table III, evaluated for the model systems shown in Fig. 1. Extended results, including more excited states up to 5.5 eV at vertical excitation, all ring sizes, various basis sets, and additional computational methods, are provided in SM TABLE S1–TABLE S4. Predictions made by the CAM-B3LYP, HSE06, MRCI, CCSD, CCSD(T), and EOMCCSD methods are mostly in good agreement, suggesting that the evaluated properties are reliable. Results from CASSCF are qualitatively similar but not of quantitative accuracy owing to its neglect of dynamics electron correlation, with CASPT2 results being unreliable owing to low-energy-denominator effects. The results presented for the 5-ring model obtained using both full CAM-B3LYP and that incorporated into a QM/MM scheme are

very similar, with only the QM/MM scheme applied to 10- to 30-ring models. The presented results are: the vertical absorption energies ΔE_v^A at the ground-state optimised geometries, the adiabatic transition energies ΔE_0 evaluated at individually optimised geometries, and the reorganisation energies associated with absorption (λ^A) and emission (λ^E). The adiabatic transition energies ΔE_0 may be directly compared to observed ZPL energies ΔE_{00} by neglecting the (usually small, but at most 0.25 eV) [24] changes in zero-point energy ΔE_{zpt} that can occur. Also, the emission reorganisation energies λ^E can be directly compared to the observed data in Fig. 2 if non-degenerate states are assumed and allowed Franck-Condon intensity [100] rather than vibronically-borrowed Herzberg-Teller intensity [101] dominates.

That so many different methods predict similar results for the triplet manifold is unusual for defect spectroscopy [24]. The reason for this is that the ground state is predicted to be $(1)^3A_2'$, a state that contains seemingly full shells of both spin-up and spin-down electrons (Fig. 4) and hence can be treated using conventional DFT and CC techniques; the important $(1)^3E''$ excited state has similar properties. As the ground state $(1)^3A_2'$ is well represented, TDDFT and EOMCCSD approaches are expected to provide good descriptions of all states that can be produced from it by single excitation. Prediction of this $(1)^3A_2'$ ground state agrees with previous calculations that are in accord with observed ODMR magnetic properties [17, 18].

Convergence of the CAM-B3LYP calculations with respect to expansion of the model compound from 1-ring to 30-ring compounds, extension to a 3-layer model, and further extension to include implicit treatment of the surrounding h-BN crystal, as well as basis-set expansion, is described in SM Section S3. In summary, the 1-ring model is only qualitatively indicative, the 2-ring model is adequate for most purposes, and the 3-ring model is quantitatively reliable. The correction needed to apply to 2-ring 6-31G* calculations to mimic 6-ring cc-pVTZ calculations in solid h-BN is (–0.01 ± 0.07) eV, and at most 0.15 eV in magnitude. Hence 2-ring 6-31G* calculations are identified as a computationally efficient approach of sufficient accuracy to support the comparison of calculated and observed data; later, mostly only calculations at this level are applied to the singlet manifold. In general, convergence of basic energetics calculations on model-compounds pertaining to localized-defect transitions have been found to converge rapidly to the same results as obtained from (much larger) converged periodic-defect calculations [102].

In D_{3h} symmetry, the low-lying triplet excited states are predicted to be $(1)^3E''$ (forbidden Franck-Condon emission), $(1)^3A_1''$ (allowed Franck-Condon emission, lone lifetime, out-of-plane polarised), and $(1)^3E'$ (allowed Franck-Condon emission, short lifetime, in-plane polarised). Also, whilst $(1)^3E'$ is predicted to dominate absorption at the excitation wavelength used in the experiments (532 nm, 2.33 eV, see SM TABLE S16 and FIG. S12), it appears to be too high in energy

and its spectrum too broad to account for the emission process, so attention is focused onto the $(1)^3E''$ and $(1)^3A_1''$ states.

The $(1)^3E''$ first excited triplet state must undergo Jahn-Teller distortion, hence manifesting a tricorn Mexican hat potential-energy surface (see, e.g., Fig. 5), leading to state components with C_{2v} symmetry that are labelled $(1)^3A_2$ and $(1)^3B_1$. The relative ordering of these components is critical to understanding spectroscopic properties. CAM-B3LYP calculations on the 2-ring model compound predict that $(1)^3A_2$ is lower in energy by 0.18 eV, defining the available stable isomers, with correction to embed the defect in a 3D h-BN crystal changing this to 0.19 eV (Table III). Similarly, EOMCCSD calculations predict an isomerization barrier of 0.15 eV. Also, CCSD/6-31G predicts a barrier of 0.43 eV, but this result is unreliable as this method incorrectly splits the energy of these state components by 0.23 eV at the D_{3h} ground-state geometry. In contrast, MRCI predicts no barrier and CASSCF predicts that $(1)^3B_1$ is lower in energy by 0.49 eV. Other reported calculations for this splitting based on DFT and CASSCF approaches have also reported $(1)^3B_1$ as being of lower energy [17], but as these methods sometimes predict results similar to higher-level approaches and sometimes results that are very different, we are unable to estimate their reliability. The proper treatment of dynamical electron correlation is critical. We find that the MRCI Davidson correction is also significant. Hence the CAM-B3LYP and EOMCCSD results that embody more of the basic physics without inherent unreliability issues are taken as to be the most indicative. Note that the CAM-B3LYP and EOMCCSD calculations indicate that an avoided crossing between $(1)^3E''$ and $(1)A_1''$ upon C_{2v} distortion is more significant than the Jahn-Teller effect and generates an extremely complex low-energy excited-state manifold, see e.g. SM Section S8, especially FIG. S10 and TABLE S14.

Table III shows that most calculation methods predict that the adiabatic transition energy for $(1)^3A_2 \rightarrow (1)^3A_2'$ photoluminescence is in the range ΔE_0 = 1.6–1.8 eV. This is in good agreement with the emission origin energies of $\Delta E_{00} \sim 1.6$ eV (SM FIG. S1) obtained using Huang-Rhys models to interpret the spectra as if they arise from single emission sources. Alternatively, the calculated emission reorganisation energies (Table III) are λ^E = 0.33 eV (CAM-B3LYP) and 0.27 eV (EOMCCSD) for the 2-ring model. The calculated correction to obtain CAM-B3LYP results for large rings with the cc-pVTZ basis embedded in 3D h-BN is –0.08 eV, reducing this to 0.25 eV. If the same correction is applied to the EOMCCSD results (Table III), the value becomes 0.19 eV. As shown in Fig. 2, the associated CAM-B3LYP spectrum is broader than that originally reported [5] and much broader than those reported herein. In SM Section S8, a Jahn-Teller spectral model is developed that simultaneously includes both the $(1)^3A_2$ and $(1)^3B_1$ components of the $(1)^3E''$ state. The best-estimate spectrum obtained from the CAM-B3LYP 2-ring model is shown in Fig. 2. It

displays apparent spectral narrowing and is much more reminiscent of the observed spectra. A crudely estimated EOMCCSD spectrum is also mooted in the figure, obtained by scaling the CAM-B3LYP spectrum by the estimated λ^E difference, that is similar to our newly observed spectra. Note that, within the Jahn-Teller model, interchange of the ordering of $(1)^3A_2$ and $(1)^3B_1$ does not greatly perturb the spectral width as the critical lower-energy component always has the larger reorganisation energy (see SM Section S8).

It is possible that the CAM-B3LYP, EOMCCSD, and MRCI calculations misrepresents state ordering and that in fact $(1)^3A_1''$ lies lower than $(1)^3E'$. The calculations indicate that $(1)^3A_1''$ has a minimum of D_{3h} symmetry plus also an associated set of C_{2v} symmetry that we label $(2)^3A_2$ resulting from avoided crossings with higher-energy states, but the later appears to become unviable as ring-size increases. Considering the high-symmetry geometry, the calculated emission reorganisation energies (Table III) for $(1)^3A_1'' \rightarrow (1)^3A_2'$ vary over the range 0.03–0.09 eV and are consistent with our new observed spectra, as demonstrated by the simulated spectrum shown in Fig. 2.

D. Electronic-structure calculations for the singlet manifold

Based on the highly open-shell nature of the low-energy singlet states of V_B^- as depicted in Fig. 4, the methods properties listed in Table II indicate that standard particle-conserving single-reference methods, such as DFT, CCSD, or CCSD(T), should not provide qualitatively useful spectroscopic descriptions. The results presented in SM Section S6 indeed do indicate that this is the case. Alternatively, the particle-non-conserving DIP-EOMCC methodology is ideally-suited to this application, and mostly we focus on these results, seeking reliable error estimates for the calculated quantities. We also provide MRCI results, which, like those presented for the triplet manifold, are expected to be realistic, but nevertheless difficult to estimate error bounds for. All geometry optimisations are performed using CASSCF, as DFT methods are extremely unreliable for the singlet manifold. As for the triplet manifold, CASSCF typically predicts that the singlet states of interest are unstable to out of plane distortions, but likewise we also find that MRCI prefers high-symmetry structures instead. Even though there is no formal proof that MRCI (and more importantly DIP-EOMCC) predicts high symmetry structures, mostly, we confine discussion to their consideration only.

Details of the DIP-EOMCC calculations, emphasising convergence with respect to higher-order electron correlation effects and basis set size, are presented in SM Section S7. A full set of DIP-EOMCC results obtained using the 3-hole–1-particle 3*h*-1*p* approximation and a 6-31G basis set, abbreviated as DIP-EOMCC(3*h*-1*p*)/6-31G or DIP(3*h*-1*p*)/6-31G for short, is reported. Corrections to the raw DIP(3*h*-1*p*)/6-31G data to include the leading high-order 4*h*-2*p* correlations

outside the CCSD core, as well as the replacement of the 6-31G basis set by its larger 6-31G* counterpart, lead to extrapolated DIP(4*h*-2*p*)/6-31G* values seen in Tables 4, S9, and S11. These corrections are mostly less than 0.1 eV in magnitude (see SM Section S7 for further details).

Calculated adiabatic transition energies and emission reorganisation energies within the singlet manifold are listed in Table IV, with vertical and adiabatic energy differences to $(1)^3A_2'$ listed in SM TABLE S11 and the vertical and adiabatic transition energies and reorganisation energies between all states considered listed in TABLE S10. The lowest-energy singlet state is predicted to be $(1)^1E'$, which undergoes a large Jahn-Teller distortion to form $(1)^1B_2$ minima and $(1)^1A_1$ transition states, as indicated in Fig. 5. The next singlet state is predicted to be $(1)^1A_1''$, which distorts to $(1)^1A_2$. This is very close in energy to $(1)^1E''$, a state that undergoes a Jahn-Teller distortion to $(2)^1A_2$ (minima) and $(1)^1B_1$ (transition states), but the distortion is weak and the avoided crossing between $(1)^1A_2$ and $(2)^1A_2$ is important and taken to dominate the excited-state properties. A variety of states are apparent at energies ca. 0.5 eV higher, but we briefly consider only one of these, $(2)^1A_1$ owing to its close relationship to $(1)^1E'$ that is apparent from considering the diabatic state descriptions given in Fig. 4. The properties of the singlet-state manifold are complex and best understood globally through the state-energy-minimum depiction provided in SM FIG. S2.

Quantitatively, the lowest-energy singlet component $(1)^1B_2$ for the 2-ring model is predicted to lie adiabatically 0.56 eV above the triplet ground state $(1)^3A_2'$ (SM TABLE S11); applying the QM/MM procedure to expand the ring size to a 5-ring model (see SM Section S7) increases this to 0.84 eV. The lowest energy photoemission within the singlet manifold is similarly predicted to be $(1)^1A_2 \rightarrow (1)^1B_2$ at ΔE_0 = 1.25 eV (Table IV). Next follows $(2)^1A_2 \rightarrow (1)^1B_2$ at ΔE_0 = 1.44 eV, close to the observed emission energy. Of greatest note, the emission reorganisation energy for this is calculated to be λ^E = 0.10 eV, something possibly consistent with the very narrow observed photoluminescence spectra. That this transition could account for the observed photoluminescence peaks at 1.5–1.6 eV (Fig. 2) therefore requires further consideration.

E. State dipole moments: possible Stark shifts and long-range dielectric spectral shifts

The calculated dipole moment changes for the excited states of the V_B^- of h-BN are described in SM Section S5. Even though these changes can be quite large and indicate substantial charge transfer within the inner ring of the defect, associated Stark effects are predicted to be small, with spectral shifts as large as 0.1 eV requiring nearby charges or ion pairs.

F. Photoluminescence assignment possibilities.

The most likely origins of the observed photoluminescence analysed within the Huang-Rhys model to have ΔE_{00} ~ 1.6 eV and λ^E < 0.05 eV is either the triplet transition $(1)^3E'' \rightarrow (1)^3A_2'$, with dominant $(1)^3A_2 \rightarrow (1)^3A_2'$ component for which the best calculations predict ΔE_0 = 1.78–1.83 eV and λ^E = 0.19–0.25 eV, and/or the singlet transition $(1)^1E'' \rightarrow (1)^1E'$, with dominant $(2)^1A_2 \rightarrow (1)^1B_2$ component for which calculations predict ΔE_0 = 1.44 eV and λ^E = 0.10 eV. Another possibility is also $(1)^3A_1'' \rightarrow (1)^3A_2'$ emission as this is predicted at ΔE_0 = 2.00–2.13 eV and to be very narrow with λ^E = 0.03–0.07 eV.

If $(1)^3E'' \rightarrow (1)^3A_2'$ is responsible, then either the calculation methods all significantly misrepresent the reorganisation energy, or else the apparent spectral width must be narrower than what is trivially expected owing to the Jahn-Teller effect. If either $(1)^1E'' \rightarrow (1)^1E'$ or $(1)^3A_1'' \rightarrow (1)^3A_2'$ are involved, then the operative photochemical processes need to be of a type that would facilitate population buildup on the initial states for a sufficiently long period. This is in-principle possible as the observed quantum yield is very low.

In the following two subsections, to examine these possibilities, we consider sophisticated spectral simulation approaches followed by photochemical reaction-rate estimations.

G. Spectral simulations

A variety of Huang-Rhys and Jahn-Teller spectral simulations are performed, as described in SM Section S8, with the principle results shown in Fig. 2. Details including the form and displacement of the critical normal modes, their ring-size dependence, symmetry, contributions from Franck-Condon (allowed) and Herzberg-Teller (forbidden) intensity, and model dependences, are discussed therein. Full details including excited-state frequencies and the associated Duschinsky rotation matrices are also provided in SM data files. The absorption spectra predicted using individually determined vibrational modes for each excited state are also presented in SM FIG. S12.

For the $(1)^3E'' \rightarrow (1)^3A_2'$ emission, a major result is that the Jahn-Teller effect is capable of narrowing apparent spectral widths, as shown in Fig. 2, whilst maintaining the adiabatic transition energy ΔE_0 and reorganisation energy λ^E. The Jahn-Teller effect withdraws intensity from the spectral wings to concentrate it around the vertical emission energy $\Delta E_v^E = \Delta E_0 - \lambda^E$. Note that, within the Jahn-Teller analysis, the ZPL is forbidden; all intensity is therefore associated with vibronic origins. As the Jahn-Teller distortion intrinsically permits allowed out-of-plane polarised emission, a vibronic origin results from the e' distortion. In addition, the $(1)^3E''$ state may couple vibronically with the nearby $(1)^3E'$ state, facilitating additional vibronic origins with e'' symmetry.

The intensity of such transitions has been calculated using Herzberg-Teller theory (see SM TABLE S15). These results indicate that the borrowed in-plane polarised intensity should be 7 times stronger than the intrinsic out-of-plane polarised contribution.

Concerning the possibility of $(1)^3A_1'' \rightarrow (1)^3A_2'$ emission, the predicted spectrum (Fig. 2) is indeed very narrow and fully consistent with the observed narrow bandshape. Minimal Herzberg-Teller intensity is predicted for this transition, making it purely out-of-plane polarized. The spectral bandshape calculated for the $(2)^1A_2 \rightarrow (1)^1B_2$ (dominant) component of the $(1)^1E'' \rightarrow (1)^1E'$ emission is also in good agreement with experiments (Fig. 2).

H. Rates for photochemical reactions and photoemission

The low quantum yield of photoemission requires explanation. The rates of many photophysical and photochemical processes are determined from the calculated triplet and singlet potential energy surfaces in SM Section S9. Basically, this involves the use of traditional adiabatic electron-transfer theory [89-97] to estimate the activation energies for the reactions involved, based on calculated adiabatic transition energies and the associated reorganization energies, as well as the associated calculated electronic couplings needed to drive intersystem crossing reactions. Key results summarised in Fig. 6 (77 K) and SM FIG. S14 (295 K). Overviewing Fig. 6, vertical absorption is predicted to be 2000 times stronger to $(1)^3E'$ than to $(1)^3A_1''$, with absorption to $(1)^3E'$ being Franck-Condon forbidden. After allowing for geometry relaxation, Jahn-Teller and avoided crossing interactions, and vibronic (Herzberg-Teller) borrowing, these ratios become 2000:1:8. Fast relaxation from $(1)^3E'$ quickly transfers the absorbed energy to either $(1)^3A_2$ or $(2)^3A_2$.

The $(1)^3E'' \rightarrow (1)^3A_2'$ photoemission is predicted to have a lifetime of 11 μs, much slower than the intersystem crossing to $(1)^1B_2$ which has a predicted lifetime of 3.8 ns at 77 K and 1.7 ns at 295 K. Calculated rates for this process are insensitive to details of the calculations such as the use of EOM-CCSD, or MRCI as the $(1)^1B_2$ surface crosses $(1)^3E''$ close to its $(1)^3A_2$ minimum. It is therefore a robust prediction of the calculations that intersystem crossing to the singlet manifold consumes most of the quantum yield, with the quantum yield for photoluminescence from within the triplet manifold being very low, ~0.03 %, and temperature insensitive, in qualitative agreement with the experimental data. The quantum yield is small but needs to be large enough to produce the observed ODMR contrast, which is suggestive of values of this order. Of the other possible scenarios considered for the photoemission, for the $(1)^3A_1'' \rightarrow (1)^3A_2'$ transition, the predicted emission lifetime, quantum yield, and temperature dependence are inconsistent with the experimental observations. For $(2)^1A_2 \rightarrow (1)^1B_2$, most predicted photochemical properties are highly inconsistent

with those required. A feature of interest, however, is the long ground-rate recovery times of 10^{23} s at 77 K and 1.8 s at 295 K. These rates are sensitive to calculation details, with a 0.3 eV reduction in the calculated energy differences leading to times of 3 s and 2 μs, respectively. Hence the calculations cannot rule out the possibility that initial excitation converts most of the defects in the h-BN to their singlet state, with subsequent absorption and emission happening within the singlet manifold. Nevertheless, the photochemical data strongly suggests that the photoemission is $(1)^3E'' \rightarrow (1)^3A_2'$.

IV. CONCLUSIONS

The reliable prediction of defect spectroscopic properties remains a severe challenge for both electronic-structure computation and spectral/photochemical simulation. Our conclusion for V_B^- is that, to within likely errors in the calculations, only the $(1)^3E'' \rightarrow (1)^3A_2'$ emission is capable of explaining the observed emission associated with ODMR. This is despite all high-level computational methods used predicting the spectrum to be broader than those observed. Indeed, our new experimental measurements, presenting bands much narrower than previously observed, accentuate this effect. Issues such as the critical role of the Jahn-Teller effect in driving apparent spectral narrowing, and the role of acoustic phonons, demand further attention. Central to this is the loss of the generally accepted qualitative scenario that the ZPL is apparent in spectra, whereas our calculations perceive it as forbidden, but otherwise located in the far high-energy tail of the spectrum. One alternate assignment possibility cannot be eliminated, however, and that is that initial irradiation converts the defects into a long-lived singlet state, with subsequent absorption end emission pertaining to this manifold.

Concerning electronic-structure calculations, we see the need for reliable high-level methods with useful worst-case scenario error expectations. One of the key findings of this work is the demonstration of the ability of the DIP-EOMCC methodology to provide a reliable description of the complex singlet manifold of the V_B^- defect in h-BN. Even basic DIP-EOMCC($3h$-$1p$)-level truncation opens up new possibilities for reliable modelling defects in h-BN and similar 2D materials. It could also be applied to less-difficult scenarios such as the triplet manifold of V_B^-. Associated with this is the coupling of such high-level methods with QM/MM schemes, allowing the QM part of this to accurately describe electronic effects and the MM part to simultaneously describe long-range nuclear structural effects. Such approaches should become the norm for defect spectroscopic modelling.

ACKNOWLEDGEMENTS

We thank the Australian Research Council (DP 160101301, DP190101058 and DE180100810), National Natural Science Foundation of China (NSFC; Grant 11674212), and the Chemical Sciences, Geosciences and Biosciences Division, Office of Basic Energy Sciences, Office of Science, U.S. Department of Energy (Grant No. DE-FG02-01ER15228) for funding this work and National Computational Infrastructure (grant no2) and Intersect (Grants d63, r88, sb4) as well as computer facilities at Shanghai and Michigan State Universities for computer time.

References

1. T. T. Tran, K. Bray, M. J. Ford, M. Toth, and I. Aharonovich, Nat. Nanotechnol., **11**, 37, (2016).
2. T. T. Tran, C. Elbadawi, D. Totonjian, C. J. Lobo, G. Grosso, H. Moon, D. R. Englund, M. J. Ford, I. Aharonovich, and M. Toth, ACS Nano, **10**, 7331, (2016).
3. T. T. Tran, C. Zachreson, A. M. Berhane, K. Bray, R. G. Sandstrom, L. H. Li, T. Taniguchi, K. Watanabe, I. Aharonovich, and M. Toth, Phys. Rev. Appl., **5**, 034005 (2016).
4. S. A. Tawfik, A. Sajid, M. Fronzi, M. Kianinia, T. T. Tran, C. Stampfl, I. Aharonovich, M. Toth, and M. J. Ford, Nanoscale, **9**, 13575, (2017).
5. A. Gottscholl, M. Kianinia, V. Soltamov, C. Bradac, C. Kasper, K. Krambrock, A. Sperlich, M. Toth, I. Aharonovich, and V. Dyakonov, Nat. Mater., **19**, 540, (2020).
6. N. Chejanovsky, A. Mukherjee, Y. Kim, A. Denisenko, A. Finkler, T. Taniguchi, K. Watanabe, D. B. R. Dasari, J. H. Smet, and J. Wrachtrup, arXiv:1906.05903, (2019).
7. D. D. Awschalom, L. C. Bassett, A. S. Dzurak, E. L. Hu, and J. R. Petta, Science, **339**, 1174, (2013).
8. F. Xia, H. Wang, D. Xiao, M. Dubey, and A. Ramasubramaniam, Nat. Photonics, **8**, 899, (2014).
9. I. Aharonovich, D. Englund, and M. Toth, Nat. Photonics, **10**, 631, (2016).
10. A. Lohrmann, B. Johnson, J. McCallum, and S. Castelletto, Rep. Prog. Phys., **80**, 034502, (2017).
11. A. Sajid, M. J. Ford, and J. R. Reimers, Rep. Prog. Phys., **83**, 044501, (2020).
12. M. Abdi, J.-P. Chou, A. Gali, and M. Plenio, ACS Photonics, **5**, 1967, (2018).
13. M. E. Turiansky, A. Alkauskas, L. C. Bassett, and C. G. Van de Walle, Phys. Rev. Lett., **123**, 127401, (2019).
14. L. Weston, D. Wickramaratne, M. Mackoit, A. Alkauskas, and C. G. Van de Walle, Phys. Rev. B, **97**, 214104, (2018).
15. J.-W. Feng, and J.-X. Zhao, J. Mol. Model., **20**, 2197, (2014).
16. A. Sajid, J. R. Reimers, and M. J. Ford, Phys. Rev. B, **97**, 064101, (2018).
17. V. Ivády, G. Barcza, G. Thiering, S. Li, H. Hamdi, J.-P. Chou, Ö. Legeza, and A. Gali, NPJ Comput. Mater., **6**, 41, (2020).
18. A. Sajid, K. S. Thygesen, J. R. Reimers, and M. J. Ford, Commun. Phys., **3**, 153, (2020).
19. B. Huang, and H. Lee, Phys. Rev. B, **86**, 245406, (2012).
20. B. Huang, H. Xiang, J. Yu, and S.-H. Wei, Phys. Rev. Lett., **108**, 206802, (2012).
21. C. Attaccalite, M. Bockstedte, A. Marini, A. Rubio, and L. Wirtz, Phys. Rev. B, **83**, 144115, (2011).
22. S. Choi, T. T. Tran, C. Elbadawi, C. Lobo, X. W. Wang, S. Juodkazis, G. Seniutinas, M. Toth, and I. Aharonovich, ACS Appl. Mater. Interfaces, **8**, 29642, (2016).
23. Y. Xue, H. Wang, Q. Tan, J. Zhang, T. Yu, K. Ding, D. Jiang, X. Dou, J.-j. Shi, and B.-q. Sun, ACS Nano, **12**, 7127, (2018).
24. J. R. Reimers, A. Sajid, R. Kobayashi, and M. J. Ford, J. Chem. Theory Comput., **14**, 1602, (2018).

25. See Supplemental Material at http://link.aps.org/supplemental/10.1103/PhysRevB.?????? for 9 additional subsections of text concerning methods and results, 21 additional tables, 14 additional figures, and key optimized geometries and vibrational data needed to simuilate spectra.
26. M. Wladyslawski, and M. Nooijen, in *Low-Lying Potential Energy Surfaces*, edited by M. R. H. a. K. G. Dyall (American Chemical Society, Washington, 2002), ACS Symposium Series Vol. 828, pp. 65.
27. M. Nooijen, Int. J. Mol. Sci., **3**, 656, (2002).
28. K. W. Sattelmeyer, H. F. Schaefer III, and J. F. Stanton, Chem. Phys. Lett., **378**, 42, (2003).
29. T. Kuś, and A. I. Krylov, J. Chem. Phys., **135**, 084109 (2011).
30. J. Shen, and P. Piecuch, J. Chem. Phys., **138**, 194102, (2013).
31. J. Shen, and P. Piecuch, Mol. Phys., **112**, 868, (2014).
32. H. J. Werner, and P. J. Knowles, J. Chem. Phys., **82**, 5053, (1985).
33. B. O. Roos, P. R. Taylor, and P. E. M. Sigbahn, Chem. Phys., **48**, 157, (1980).
34. K. Ruedenberg, M. W. Schmidt, M. M. Gilbert, and S. T. Elbert, Chem. Phys., **71**, 41, (1982).
35. K. R. Shamasundar, G. Knizia, and H.-J. Werner, J. Chem. Phys., **135**, 054101, (2011).
36. J. F. Stanton, and R. J. Bartlett, J. Chem. Phys., **98**, 7029, (1993).
37. M. E. Casida, in *Recent Advances in Density Functional Methods, Part 1*, edited by D. P. Chong (World Scientific, Singapore, 1995), pp. 155.
38. W. D. Cornell, P. Cieplak, C. I. Bayly, I. R. Gould, K. M. Merz Jr, D. M. Ferguson, D. C. Spellmeyer, T. Fox, J. W. Caldwell, and P. A. Kollman, J. Am. Chem. Soc., **117**, 5179, (1995).
39. N. Mendelson, D. Chugh, J. R. Reimers, T. S. Cheng, A. Gottscholl, H. Long, C. J. Mellor, A. Zettl, V. Dyakonov, P. H. Beton, S. V. Novikov, C. Jagadish, H. H. Tan, M. J. Ford, M. Toth, C. Bradac, and I. Aharonovich, arXiv, **2003.00949v3**, (2020).
40. K. Huang, A. Rhys, and N. F. Mott, Proc. R. Soc. London, A, **204**, 406, (1950).
41. P. Hohenberg, and W. Kohn, Phys. Rev., **136**, B864, (1964).
42. W. Kohn, and L. J. Sham, Phys. Rev., **140**, A1133, (1965).
43. O. Gunnarsson, and B. I. Lundqvist, Phys. Rev. B, **13**, 4274, (1976).
44. Z.-L. Cai, and J. R. Reimers, J. Chem. Phys., **112**, 527, (2000).
45. F. Wang, and T. Ziegler, J. Chem. Phys., **121**, 12191, (2004).
46. P. H. Dederichs, S. BÏgel, R. Zeller, and H. Akai, Phys. Rev. Lett., **53**, 2512, (1984).
47. C. P. Plaisance, R. A. Van Santen, and K. Reuter, J. Chem. Theory Comput., **13**, 3561, (2017).
48. B. Kaduk, T. Kowalczyk, and T. Van Voorhis, Chem. Rev., **112**, 321, (2012).
49. Q. Wu, and T. Van Voorhis, J. Chem. Theory Comput., **2**, 765, (2006).
50. G. L. Manni, R. K. Carlson, S. Luo, D. Ma, J. Olsen, D. G. Truhlar, and L. Gagliardi, J. Chem. Theory Comput., **10**, 3669, (2014).
51. J. Gao, A. Grofe, H. Ren, and P. Bao, J. Phys. Chem. Lett., **7**, 5143, (2016).
52. L. Yang, A. Grofe, J. R. Reimers, and J. Gao, Chem. Phys. Letts., **736**, 136803, (2019).
53. A. B. J. Parusel, and S. Grimme, J. Phys. Chem. B, **104**, 5395, (2000).
54. J. P. Perdew, K. Burke, and M. Ernzerhof, Phys. Rev. Lett., **77**, 3865, (1996).
55. A. V. Krukau, O. A. Vydrov, A. F. Izmaylov, and G. E. Scuseria, J. Chem. Phys., **125**, 224106, (2006).
56. J. Heyd, G. E. Scuseria, and M. Ernzerhof, J. Chem. Phys., **118**, 8207, (2003).
57. T. Yanai, D. P. Tew, and N. C. Handy, Chem. Phys. Lett., **393**, 51, (2004).
58. R. Kobayashi, and R. D. Amos, Chem. Phys. Lett., **420**, 106, (2006).
59. Z.-L. Cai, M. J. Crossley, J. R. Reimers, R. Kobayashi, and R. D. Amos, J. Phys. Chem. B, **110**, 15624, (2006).
60. Z.-L. Cai, K. Sendt, and J. R. Reimers, J. Chem. Phys., **117**, 5543, (2002).
61. J. Čížek, J. Chem. Phys., **45**, 4256, (1966).
62. J. Čížek, Adv. Chem. Phys., **14**, 35, (1969).
63. J. Paldus, J. Íek, and I. Shavitt, Phys. Rev. A, **5**, 50, (1972).

64. G. P. Purvis, III, and R. J. Bartlett, J. Chem. Phys., **76**, 1910, (1982).
65. R. J. Bartlett, and M. Musiał, Reviews of Modern Physics, **79**, 291, (2007).
66. K. Raghavachari, G. W. Trucks, J. A. Pople, and M. Head-Gordon, Chem. Phys. Lett., **157**, 479, (1989).
67. K. Andersson, P. Å. Malmqvist, B. O. Roos, A. J. Sadlej, and K. Wolinski, J. Phys. Chem., **94**, 5483, (1990).
68. K. Andersson, P.-Å. Malmqvist, and B. O. Roos, J. Chem. Phys., **96**, 1218, (1992).
69. M. Bockstedte, F. Schütz, T. Garratt, V. Ivády, and A. Gali, NPJ Quant. Mater., **3**, 31, (2018).
70. J. R. Reimers, R. Kobayashi, and M. J. Ford, arXiv, **2006.16463**, (2020).
71. L. Goerigk, and S. Grimme, Phys. Chem. Chem. Phys., **13**, 6670, (2011).
72. M. Svensson, S. Humbel, R. D. J. Froese, T. Matsubara, S. Sieber, and K. Morokuma, J. Phys. Chem., **100**, 19357, (1996).
73. S. Dapprich, I. Komaromi, B. K. S., K. Morokuma, and M. J. Frisch, J. Mol. Struct. (THEOCHEM), **461-462**, 1, (1999).
74. M. J. Frisch, G. W. Trucks, H. B. Schlegel, G. E. Scuseria, M. A. Robb, J. R. Cheeseman, G. Scalmani, V. Barone, G. A. Petersson, H. Nakatsuji, X. Li, M. Caricato, A. V. Marenich, J. Bloino, B. G. Janesko, R. Gomperts, B. Mennucci, H. P. Hratchian, J. V. Ortiz, A. F. Izmaylov, J. L. Sonnenberg, D. Williams, F. Ding, F. Lipparini, F. Egidi, J. Goings, B. Peng, A. Petrone, T. Henderson, D. Ranasinghe, V. G. Zakrzewski, J. Gao, N. Rega, G. Zheng, W. Liang, M. Hada, M. Ehara, K. Toyota, R. Fukuda, J. Hasegawa, M. Ishida, T. Nakajima, Y. Honda, O. Kitao, H. Nakai, T. Vreven, K. Throssell, J. A. Montgomery Jr., J. E. Peralta, F. Ogliaro, M. J. Bearpark, J. J. Heyd, E. N. Brothers, K. N. Kudin, V. N. Staroverov, T. A. Keith, R. Kobayashi, J. Normand, K. Raghavachari, A. P. Rendell, J. C. Burant, S. S. Iyengar, J. Tomasi, M. Cossi, J. M. Millam, M. Klene, C. Adamo, R. Cammi, J. W. Ochterski, R. L. Martin, K. Morokuma, O. Farkas, J. B. Foresman, and D. J. Fox, *Gaussian 16 Revision C.01*. (Gaussian Inc., Wallingford, CT, 2016).
75. H.-J. Werner, P. J. Knowles, G. Knizia, F. R. Manby, M. Schütz, P. Celani, W. Györffy, D. Kats, T. Korona, R. Lindh, A. Mitrushenkov, G. Rauhut, K. R. Shamasundar, T. B. Adler, R. D. Amos, A. Bernhardsson, A. Berning, D. L. Cooper, M. J. O. Deegan, A. J. Dobbyn, F. Eckert, E. Goll, C. Hampel, A. Hesselmann, G. Hetzer, T. Hrenar, G. Jansen, C. Köppl, Y. Liu, A. W. Lloyd, R. A. Mata, A. J. May, S. J. McNicholas, W. Meyer, M. E. Mura, A. Nicklaß, D. P. O'Neill, P. Palmieri, D. Peng, K. Pflüger, R. Pitzer, M. Reiher, T. Shiozaki, H. Stoll, A. J. Stone, R. Tarroni, T. Thorsteinsson, and M. Wang, *MOLPRO, version 2015.1, a package of ab initio programs*. (University of Birmingham, Birmingham, 2015).
76. M.W.Schmidt, K.K.Baldridge, J.A.Boatz, S.T.Elbert, M.S.Gordon, J.H.Jensen, S.Koseki, N.Matsunaga, K.A.Nguyen, S.Su, T.L.Windus, M.Dupuis, and J.A.Montgomery, J. Comput. Chem, **14**, 1347, (1993).
77. G. M. J. Barca, C. Bertoni, L. Carrington, D. Datta, N. D. Silva, J. E. Deustua, D. G. Fedorov, J. R. Gour, A. O. Gunina, E. Guidez, T. Harville, S. Irle, J. Ivanic, K. Kowalski, S. S. Leang, H. Li, W. Li, J. J. Lutz, I. Magoulas, J. Mato, V. Mironov, H. Nakata, B. Q. Pham, P. Piecuch, D. Poole, S. R. Pruitt, A. P. Rendell, L. B. Roskop, K. Ruedenberg, T. Sattasathuchana, M. W. Schmidt, J. Shen, L. Slipchenko, M. Sosonkina, V. Sundriyal, A. Tiwari, J. L. G. Vallejo, B. Westheimer, M. Włoch, P. Xu, F. Zahariev, and M. S. Gordon, J. Chem. Phys., **152**, 154102, (2020).
78. M. Włoch, J. R. Gour, and P. Piecuch, J. Phys. Chem. A, **111**, 11359, (2007).
79. W. J. Hehre, R. F. Stewart, and J. A. Pople, J. Chem. Phys., **51**, 2657, (1969).
80. W. J. Hehre, R. Ditchfield, and J. A. Pople, J. Chem. Phys., **56**, 2257, (1972).
81. T. H. Dunning, Jr., J. Chem. Phys., **90**, 1007, (1989).
82. J. Tomasi, B. Mennucci, and R. Cammi, Chem. Rev., **105**, 2999, (2005).
83. P. J. Chappell, G. Fischer, J. R. Reimers, and I. G. Ross, J. Molec. Spectrosc., **87**, 316, (1981).
84. G. Fischer, J. R. Reimers, and I. G. Ross, Chem. Phys., **62**, 187, (1981).
85. J. R. Reimers, and N. S. Hush, J. Chem. Phys., **119**, 3262, (2003).

86. J. R. Reimers, and N. S. Hush, J. Am. Chem. Soc., **126**, 4132, (2004).
87. P. C. Dastoor, C. R. McNeill, H. Frohne, C. J. Foster, B. Dean, C. J. Fell, W. J. Belcher, W. M. Campbell, D. L. Officer, I. M. Blake, P. Thordarson, M. J. Crossley, N. S. Hush, and J. R. Reimers, J. Phys. Chem. C, **111**, 15415, (2007).
88. J. R. Reimers, J. Chem. Phys., **115**, 9103, (2001).
89. V. G. Levich, and R. R. Dogonadze, Proc. Akad. Nauk. SSSR, **133**, 591, (1960).
90. R. Kubo, and Y. Toyozawa, Prog. Theor. Phys., **13**, 160, (1955).
91. N. S. Hush, J. Chem. Phys., **28**, 962, (1958).
92. R. P. Van Duyne, and S. F. Fischer, Chem. Phys., **5**, 183, (1974).
93. S. Efrima, and M. Bixon, Chem. Phys., **13**, 447, (1976).
94. J. Jortner, J. Chem. Phys., **64**, 4860, (1976).
95. N. R. Kestner, J. Logan, and J. Jortner, J. Phys. Chem., **78**, 2148, (1974).
96. A. Warshel, J. Phys. Chem., **86**, 2218, (1982).
97. S. Yin, L. Li, Y. Yang, and J. R. Reimers, J. Phys. Chem. C, **116**, 14826, (2012).
98. E. B. Wilson, J. C. Decius, and P. C. Cross, *Molecular Vibrations: The Theory of Infrared and Raman Vibrational Spectra*. (McGraw-Hill Book Company, New York, 1955).
99. P. W. Atkins, M. S. Child, and C. S. G. Phillips, *Tables for Group Theory*. (Oxford University Press, Oxford, 2006).
100. E. U. Condon, Phys. Rev., **32**, 858, (1928).
101. G. Herzberg, and E. Teller, Z. Phys. Chem., **21**, 410, (1933).
102. J. R. Reimers, A. Sajid, R. Kobayashi, and M. J. Ford, J. Phys. Chem. C, **in press DOI: 10.1021/acs.jpcc.0c06445**, (2020).
103. P. Cudazzo, I. V. Tokatly, and A. Rubio, Phys. Rev. B, **84**, 085406, (2011).

TABLE I. Key aspects of h-BN defects and their consequences for high-level spectroscopic modelling [24].

Aspects of h-BN defects	Consequences
Mostly open-shell in character	Static electron correlation often critical, posing problems for DFT and CC calculations that focus on single-reference configurations, demanding MRCI or, when appropriate, TDDFT, EOMCCSD, EOM-CC etc. methods.
Dynamically correlated	Methods such as Hartree-Fock theory, CASSCF (and DMRG) give poor results, establishing approaches such as DFT, CC, QMC, and MRCI as entry-level methods.
Strong electron-hole interactions	The ordering of electronic states can be very different to that suggested by considering only one-particle orbital energy levels, demanding extensive state searching.
Electronic arrangements modulate chemical bonding	Very large structural rearrangements can accompany electronic transitions, often leading to very large reorganisation energies, e.g., 2.5 eV, so that state energy ordering at adiabatically relaxed geometries can be very different to that perceived vertically at the ground-state geometry.
Charge transfer can occur	DFT methods such as PBE and HSE06 can, without warning, deliver very poor results, identifying range-corrected functionals such as CAM-B3LYP [60] as the entry level for DFT calculations.
Are embedded in 3D materials	Dielectric effects can be critical, but as h-BN is essentially a 2D material, such effects are minimised [103].

TABLE II. The electronic-structure computational methods used, their key properties and applicability.[a]

Method	Properties	Applicability
DFT	includes dynamic electron correlation but fails for open-shell systems	the critical triplet ground state $(1)^3A_2'$
TDDFT	excited-state open-shell systems are well described if the ground-state is closed shell	triplet excited states e.g., $(1)^3E''$, $(1)^3A_1''$, $(1)^3E'$, including depiction of the normal vibrational modes of phonons
CCSD	very good for closed-shell systems, treats static electron correlation asymmetrically	the critical triplet ground state $(1)^3A_2'$, perhaps other triplet states
CCSD(T)	typically improves on CCSD using perturbative corrections for triple excitations, but often degrades performance for open-shell systems	the critical triplet ground state $(1)^3A_2'$
DIP-EOMCC	works well for open-shell systems for which a suitable closed-shell reference is available containing two additional electrons	all states of interest, but no analytical gradients for geometry optimisation
CASSCF[b]	good description of static electron correlation, poor description of dynamic electron correlation[c]	all states qualitatively described correctly, poor quantitative accuracy and therefore below entry level
CASPT2	CASSCF plus perturbative treatment of dynamic electron correlation[c]	all states, may give poor results if low-energy coupled states are nearby
MRCI	CASSCF plus treatment of dynamic electron correlation up to double excitations, but size inconsistent[c]	all lowest-energy states of each spin and spatial symmetry, no analytical gradients for geometry optimisation

a: see SM Section S1 for discussion and explanations.
b: Enhanced treatment of static electron correlation using large active spaces is warranted and can be achieved using density-matrix renormalisation group (DMRG) approaches, and can also be empirically parameterised using DFT orbitals; these features have been applied [17] to V_B^- but are not incorporated herein.
c: All approaches based on CASSCF suffer from the limitations of the need to choose an active space and the possible use of state averaging. The active space used herein is shown in Fig. 2; with state averaging used where possible to establish overall symmetry and energy relativity. Even though calculation errors may be relatively low, these issues make error bounds difficult to estimate as it is impractical to demonstrate convergence.

TABLE III. Calculated spectroscopic properties for absorption and emission transitions within the triplet manifold of the V_B^- defect in h-BN, in eV, involving the $(1)^3A_2'$ triplet ground state.

METHOD	CAM-B3LYP	QM/MM	CAM-B3LYP	CASSCF[f]	CASPT2[b]	MRCI[b]	CCSD	CCSD(T)[d]	EOM-CCSD[c]	EOM-CCSD	Other[k]
BASIS	cc-pVTZ[a]	6-31G*	6-31G*	6-31G*	6-31G*	6-31G*	6-31G	6-31G	6-31G*	cc-pVTZ[a]	
RINGS	6[a]	30	2	2	2	2	2	2	2	6[a]	2D
LAYERS	crystal[a]	1	1	1	1	1	1	1	1	crystal[a]	1
Vertical absorption energies ΔE_v^A											
$(1)^3E''$ - $(1)^3A_2$	2.04		1.99	1.45[ehi]	1.84[o]	1.98[eh]	2.18[m]	2.12	2.16	2.21	1.92
$(1)^3E''$ - $(1)^3B_1$	2.04		1.99	1.37[ehi]		1.93[ehi]	2.41	2.25	2.16	2.21	1.92
$(1)^3A_1''$	2.03		2.08	2.25[io]	2.17[io]	2.13[o]			2.27	2.22	
$(1)^3E'$ - $(1)^3A_1$	2.65		2.76	3.01[h]	2.94[h]	2.98[h]	2.82	2.70	2.76	2.66	2.29
$(1)^3E'$ - $(1)^3B_2$	2.65		2.76						2.76	2.66	2.29
$(1)^3A_2''$			3.70						3.93		1.8
Adiabatic transition energies ΔE_0											
$(1)^3A_2$	1.78[g]	1.74	1.67	1.34[h]	1.83[h]	1.51[h]	1.60[c]		1.72	1.83	> 1.72
$(1)^3B_1$[j]	1.97		1.85	0.85[hi]		1.51[h]	2.03[c]		1.87	1.99	1.72
$(1)^3A_1''$	2.00		2.04	2.18[n]	1.54[n]	2.12[n]			2.17	2.13	
$(2)^3A_2$	1.99		1.92	2.02[io]	2.08[io]	2.18[o]			1.94	2.01	
$(1)^3A_1$[l]	2.22		2.21	2.32	2.33	2.37	2.06[c]		2.19	2.20	
$(2)^3B_2$[l]	2.25		2.21						2.22	2.26	
Absorption reorganisation energies λ^A											
$(1)^3A_2$	0.26		0.32	0.11		0.47			0.44	0.37	
$(1)^3B_1$	0.08		0.14	0.52		0.42			0.29	0.22	0.20
$(1)^3A_1''$	0.03		0.04						0.09	0.07	
$(2)^3A_2$	0.04		0.16	0.24	0.09				0.33	0.20	
$(1)^3A_1$	0.43		0.55	0.69	0.61	0.61			0.57	0.45	
$(2)^3B_2$	0.40		0.55						0.54	0.39	
Emission reorganisation energies λ^E											
$(1)^3A_2$	0.25	0.26	0.33	0.20[h]	0.49[h]	0.31[h]			0.27	0.19	
$(1)^3B_1$	0.12		0.13	-0.42[h]		0.20[h]			0.11	0.10	
$(1)^3A_1''$	0.06		0.05						0.02	0.03	
$(2)^3A_2$	0.15		0.12						0.09	0.12	
$(1)^3A_1$	0.48		0.42	0.41[h]	0.52[h]	0.51[h]			0.44	0.50	
$(2)^3B_2$	0.46		0.41						0.47	0.52	

a: After addition of CAM-B3LYP corrections to mimic calculations on the h-BN crystal for the cc-pVTZ basis set, see SM TABLE S3.
b: At CASSCF optimised geometries.
c: CCSD/6-31G at CAM-B3LYP/6-31G* optimised geometries.
d: At CCSD optimised geometries.
e: CASSCF calculations can break the degeneracy of degeneracy of E' and E'' states owing to asymmetric representation of the active space and orbital optimisation. This effect can be minimised using state-averaged approaches, and is usually reduced by MRCI.
f: CASSCF predicts symmetry lowering of $(1)^3A_2'$ to (at least) C_{2v}, influencing λ^E, but this symmetry lowering is not supported by single-point energy MRCI calculations; CCSD can also predict (much smaller) distortions not supported at the CCSD(T) level.
g: Leads to a ZPL energy of ΔE_0 = 1.76 eV after addition of the calculated zero-point energy correction of ΔE_{zpl}= -0.02 eV obtained for the 2-ring compound using CAM-B3LYP/6-31G*.
h: single-state calculation.
i: two-state calculation using 50:50 weighting; both *h* and *i* flags indicate that each approach gives this result.
j: transition state on the tricorn Mexican hat, see e.g. Fig. 5.
k: By Ivády et al. [17].
l: CAM-B3LYP 2-ring calculations indicate $(1)^3E'$ undergoes barrierless out-of-plane relaxation from $(1)^3A_1$ to $(1)^3A_2$ and from $(2)^3B_2$ to $(2)^3A_2$.
m: 2.02 eV by CCSD/6-31G*.
n: at CAM-B3LYP/6-31G* geometry.

o: three-state calculations weighted 40:30:30 predict (CASSCF, CASPT2, MRCI) energies ΔE_v^A= (2.17, 1.63, 2.13) eV and ΔE_0 = (2.22, 1.67, 2.18) eV; the CASPT2 results, which predict that $(1)^3A_1''$ is the lowest-energy triplet excited state, are believed unreliable.

TABLE IV. Calculated spectroscopic properties for emission transitions within the singlet manifold of the V_B^- defect in h-BN, in eV, involving the $(1)^1E'$ lowest-energy singlet state[a] of the 2-ring model compound and that as embedded in a 5-ring model.

initial state	to $(1)^1B_2$					to $(1)^1A_1$			
	MRCI	DIP(3*h*-1*p*)[b]	DIP(4*h*-2*p*)[b]	QM/MM[c] DIP(4*h*-2*p*)[b]	Other[d]	MRCI	DIP(3*h*-1*p*)[b]	DIP(4*h*-2*p*)[b]	QM/MM[c] DIP(4*h*-2*p*)[b]
Adiabatic transition energies ΔE_0									
$(1)^1A_2$	1.15	1.01	0.98	1.25		0.98	0.94	0.86	1.09
$(2)^1A_2$	1.18	1.31	1.35	1.44	1.33	1.01	1.24	1.23	1.28
$(1)^1B_1$	1.23	1.35	1.41	1.50		1.06	1.28	1.29	1.34
Emission reorganisation energies λ^E									
$(1)^1A_2$	0.29	0.24					0.19[e]		
$(2)^1A_2$	0.26	0.10[e]				0.15	0.03		
$(1)^1B_1$	0.26	0.10[e]				0.15	0.03		

a: the minimum of the lowest-energy singlet state $(1)^1E'$ is predicted to be its $(1)^1B_2$ component, 0.4 - 0.7 eV higher in energy than the triplet ground state $(1)^3A_2'$ (see SM TABLE S9).
b: ΔE_0 values calculated using the raw DIP(3*h*-1*p*)/6-31G and extrapolated DIP(4*h*-2*p*)/6-31G* data (see SM Table S9).
c: 5-ring total, 2-ring in QM part, frozen 2-ring structure with the outer 3 rings optimised.
d: by Ivády et al. [17].
e: to lower Born-Oppenheimer surface, as is relevant to high-energy emission; for data pertinent to the native upper Born-Oppenheimer surface, see SM TABLE S11 and FIG. S2 as they provide broader perspectives.

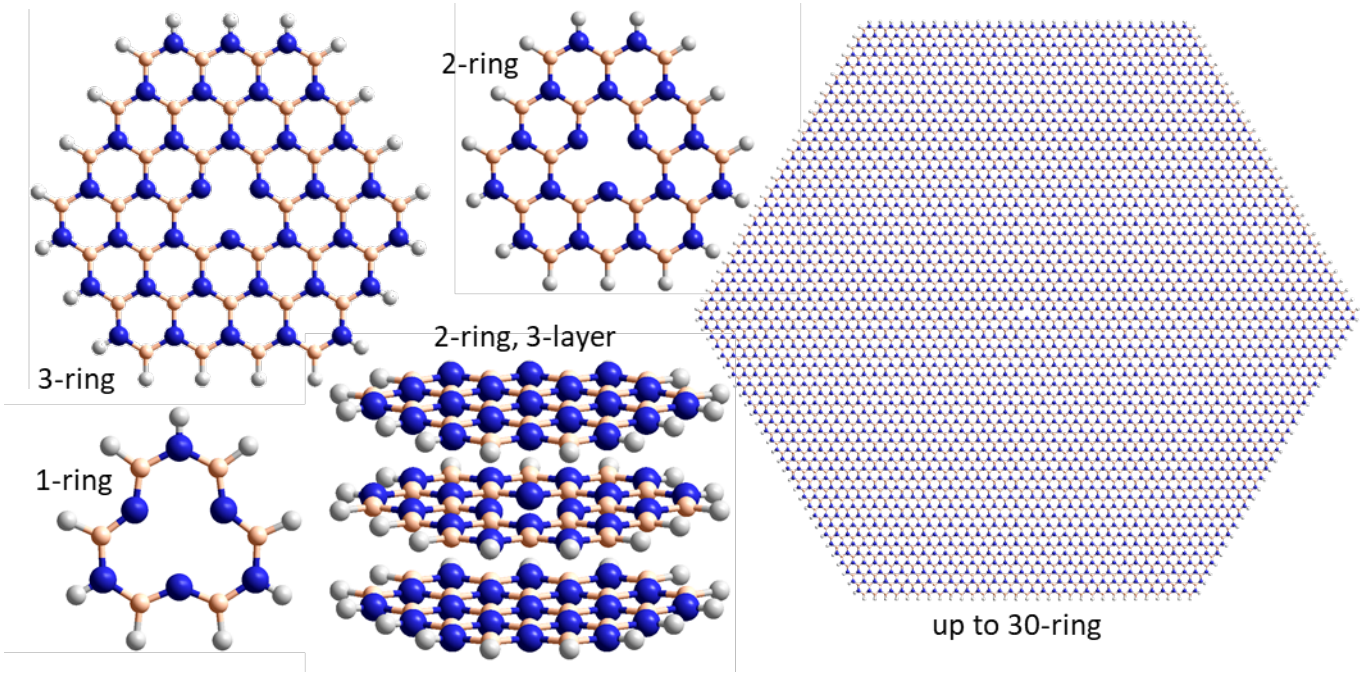

FIG. 1. Model compounds used to study the electronic states of the V_B^- defect: one layer- 1-, 2-, 3- and 30-ring shown (also 4-, 5-, 6-, 10-, 15-, 20- and 25-ring models not shown), as well as a 2-ring 3-layer model and that plus a dielectric continuum to model bulk h-BN. Blue, peach, and grey spheres represent nitrogen, boron, and hydrogen atoms, respectively.

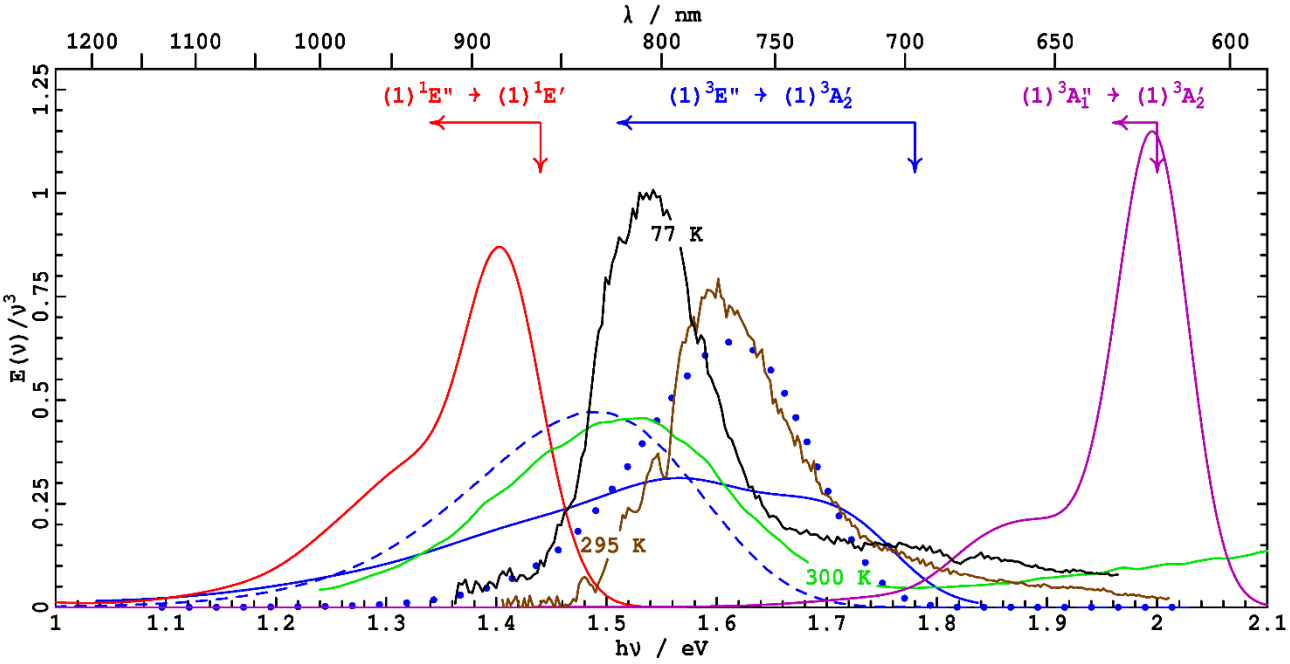

FIG. 2. Observed ensemble photoemission bandshapes of h-BN defects reported [5] as displaying ODMR with ground state zero field splitting D_{gs} = 3.5 GHz are compared to calculated bandshapes for three possible emissions. Observed spectra: at 295 K (brown) and 77 K (black) from current measurements, and at 300 K from previous ones [5] (green). Calculated spectra are for the transitions $(1)^1E'' \rightarrow (1)^1E'$ (red), $(1)^3E'' \rightarrow (1)^3A_2'$ (blue), and $(1)^3A_1'' \rightarrow (1)^3A_2'$ (purple), obtained using DIP-EOMCC Huang-Rhys (red), CAM-B3LYP Huang-Rhys (purple and blue solid), CAM-B3LYP Jahn-Teller (blue dashed), and CAM-B3LYP Jahn-Teller crudely adjusted to match the EOMCCSD ΔE_0 and λ^E (blue dots). Arrows indicate CAM-B3LYP or DIP-EOMCC ZPE locations ΔE_0 and spectral widths λ^E.

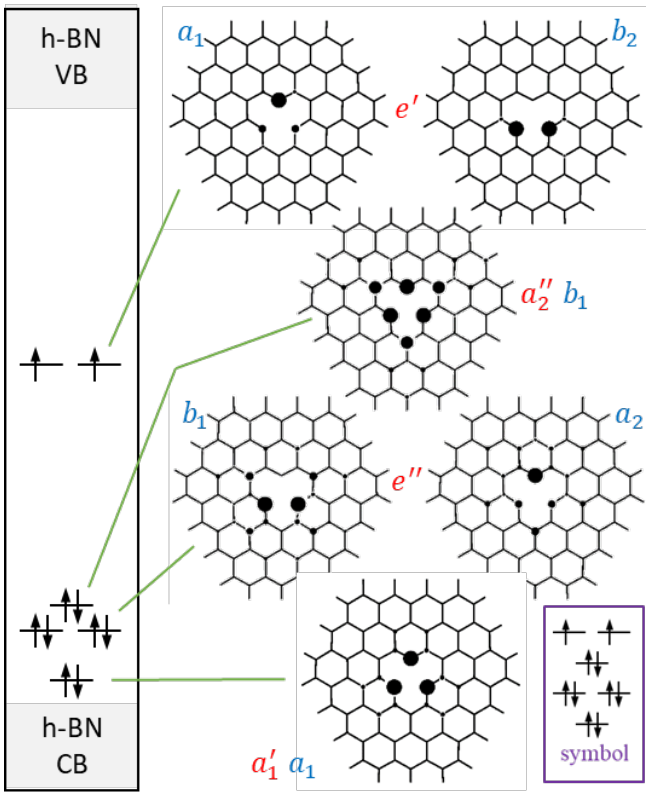

FIG. 3. The six 3-ring CAM-B3LYP/6-31G* mid-gap defect orbital energy levels (spin restricted) lying between the h-BN valence band (VB) and conduction band (CB), represented as circles depicting the atomic electron density, for the V_B^- defect in h-BN. Symmetries are indicated for both the D_{3h} (red) and C_{2v} (blue) point groups. The electronic configuration of the $(1)^3A_2'$ ground state is shown, with excited states depicted in Fig. 4 using variants of the inserted symbol.

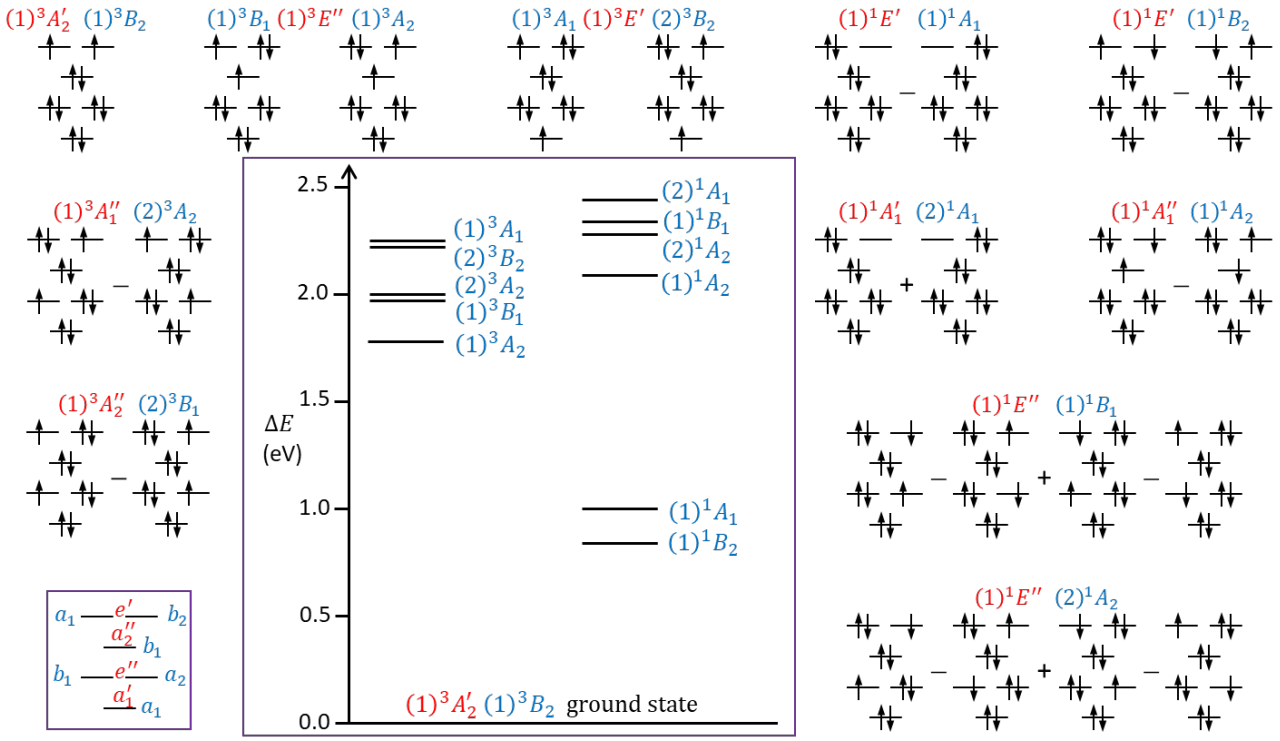

FIG. 4. Key diabatic configurations of orbital energy levels contributing to the low-energy states of the V_B^- defect in h-BN, showing symmetry labels depicting both D_{3h} (red) and C_{2v} (blue) local point-group symmetry. Adiabatic wavefunctions obtained from the electronic structure calculations are depicted throughout the text in terms of their dominant diabatic configurations, with often considerable mixing apparent that is method dependent. The inset shows the best-estimate adiabatic energy minima: triplets EOMCCSD, see Table III, singlets: DIP-EOMCC except $(2)^1A_1$ from MRCI, see Table S11; (*nb.*, singlet-triplet splittings appear to be overestimated).

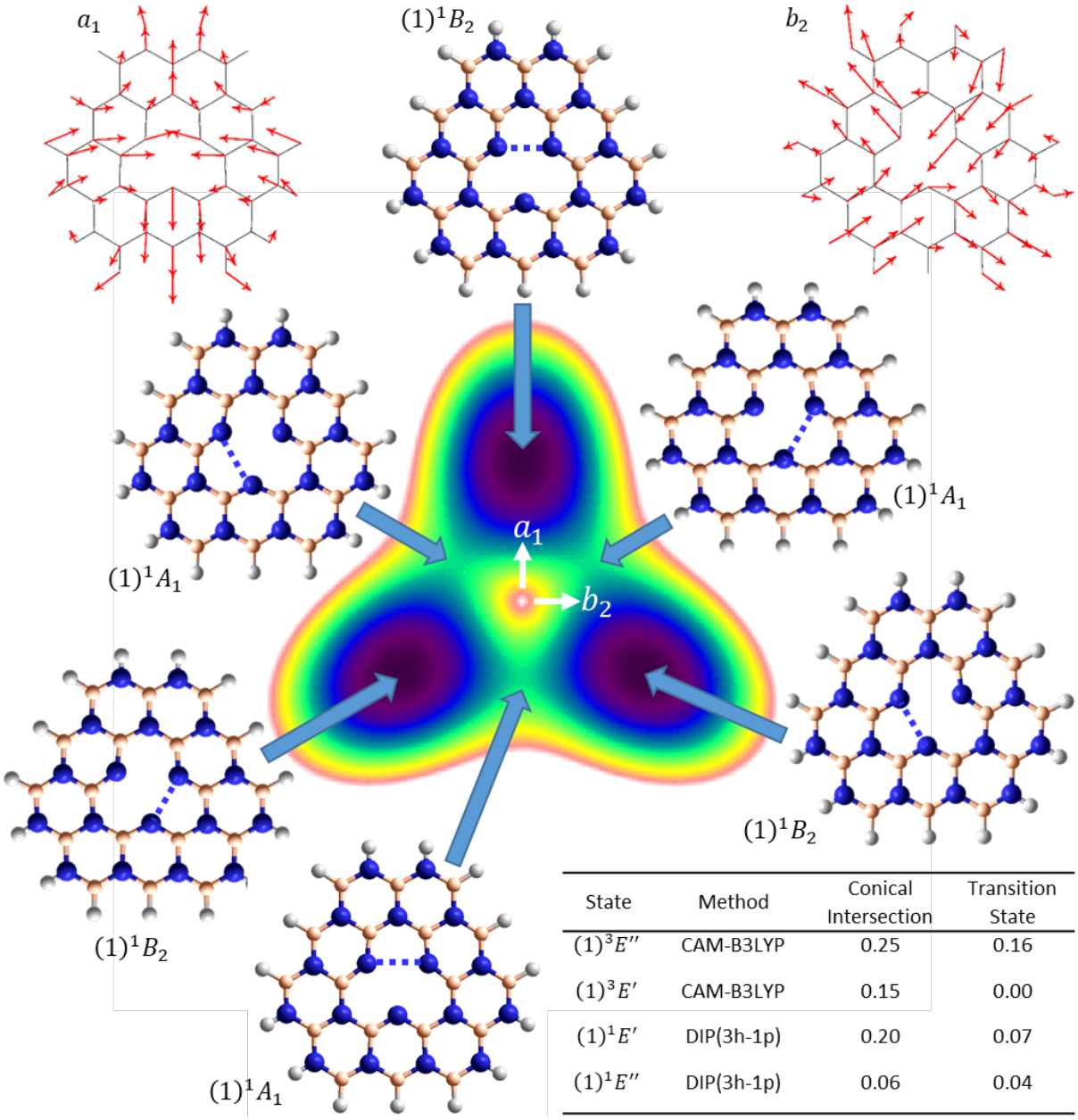

State	Method	Conical Intersection	Transition State
$(1)^3E''$	CAM-B3LYP	0.25	0.16
$(1)^3E'$	CAM-B3LYP	0.15	0.00
$(1)^1E'$	DIP(3h-1p)	0.20	0.07
$(1)^1E''$	DIP(3h-1p)	0.06	0.04

FIG. 5. Contour plot (black- low energy minima, white- energy of the conical intersection and above) depicting generic tricorn Mexican-hat Born-Oppenheimer potential-energy surface associated with Jahn-Teller conical intersections. The energy is shown as a function of displacements in the a_1 and b_2 components of some generalised e' vibrational mode, with indicated the ground-state normal-mode displacement vectors for the dominant mode involved in most transitions, $34e'$ at 183 cm^{-1} (0.023 eV) varying to 163–192 cm^{-1} in the triplet excited states. The conical intersection in the centre has D_{3h} local-point group symmetry, whereas the three lines passing through the stationary points have C_{2v} symmetry and all other points have C_s symmetry. The six indicated chemical structures were optimised using CASSCF(10,6)/6-31G* for the $(1)^1E'$ surface and depict three $(1)^1B_2$ isomers (black) and their interconnecting $(1)^1A_1$ transition-state (cyan) structures for the $(1)^1E'$ surface. The dashed lines indicate B-B separations that differ from those involving the analogous inner-ring B atom. The key shows the calculated energies of the conical intersections and transition states with respect to the minima for different V_B^- states, in eV. For $(1)^3E'$ and $(1)^1E'$, avoided crossings at C_{2v} geometries with $(1)^3A_1''$ and $(1)^1A_1''$, respectively, significantly distort the Jahn-Teller surfaces. For

more details, see SM FIG. S3 - FIG. S7 and FIG. S11, as well as TABLE S12 - TABLE S14, and TABLE S17.

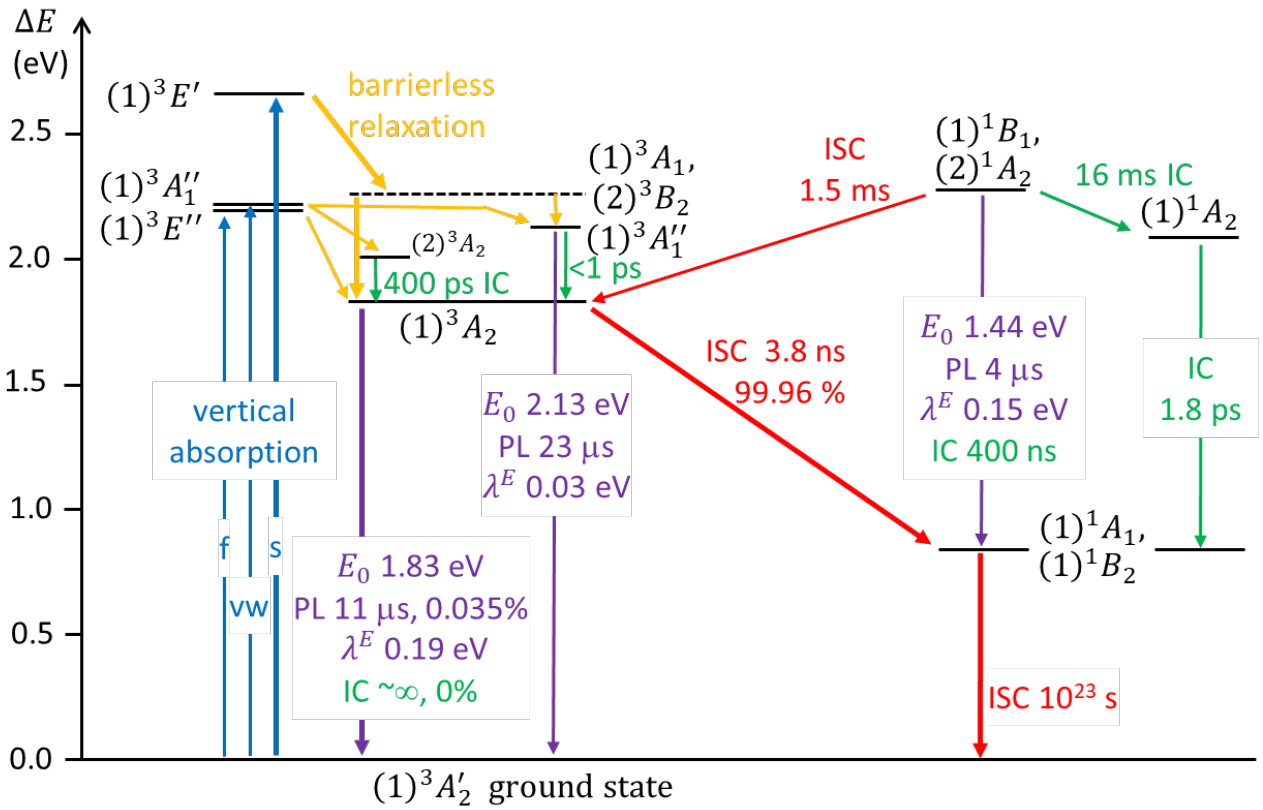

FIG. 6. Calculated photochemical and photoemission processes for the V_B^- defect of h-BN at 77 K, obtained using EOMCCSD calculations on the triplet manifold, DIP-EOMCC calculations on the singlet manifold, and MRCI-calculated transition dipole moments and spin-orbit couplings. Thicker arrows indicate the critically perceived processes during the photocycle. The indicated processes are: blue- vertical absorption (related absorption at lower energies down to the shown ZPLs and also at higher energies will also occur, see SM Fig. S12), with Franck-Condon (Herzberg-Teller) allowed oscillator strengths in the ratio f:vw:s of 0(8):1:2000; orange- barrierless ultrafast relaxation to ZPLs; green- internal conversion (IC); red- intersystem crossing (ISC), purple- photoluminescence (PL). Marked percentages indicate quantum yields. The energy levels and internal rate processes the doubly degenerate states that form transition states in C_{2v} symmetry are not shown, for clarity (see instead Fig. 4). States denoted with a solid line indicate that a local minima is established (triplet manifold) or believed (singlet manifold) to be involved, dashed lines indicate saddle structures that are unstable to out-of-plane distortion leading directly to $(1)^3A_2$. The use of different computational methods for the singlet and triplet manifolds results in overestimation of the singlet-triplet splittings. Some rates like the primary 3.8 ns ISC are insensitive to calculation details and temperature, whereas others re extremely sensitive to both, *e.g.,* the shown 10^{23} s singlet recovery time can be reduced to the seconds timescale within possible computational uncertainties. Analogous results for 295 K are shown in SM FIG. S14.

Photoluminescence, photophysics and photochemistry of the V_B^- defect in hexagonal boron nitride

Jeffrey R. Reimers[1,2], Jun Shen,[3] Mehran Kianinia,[2] Carlo Bradac,[2] Igor Aharonovich,[2] Michael J. Ford,[2] and Piotr Piecuch[3,4]

[1] *International Centre for Quantum and Molecular Structures and Department of Physics, Shanghai University, Shanghai 200444, China.*
[2] *University of Technology Sydney, School of Mathematical and Physical Sciences, Ultimo, New South Wales 2007, Australia.*
[3] *Department of Chemistry, Michigan State University, East Lansing, Michigan 48824, United States of America.*
[4] *Department of Physics and Astronomy, Michigan State University, East Lansing, Michigan 48824, United States of America.*

SUPPLEMENTAL MATERIAL

Contents

S1. PROPERTIES OF THE COMPUTATIONAL METHODS USED.

A. DFT methods

Choice of computational methods to employ in calculations of defect spectroscopy is rarely straightforward. As dynamic electron correlations originating from short-range electron-electron repulsion are identified as a key element in defect properties, the use of methods based on DFT [41-43], especially those employing its popular Kohn-Sham formulation [42], is favoured, since it allows one to treat such effects at a generally useful level for minimal computational cost. Unfortunately, basic DFT approaches in wide use today continue facing enormous challenges and, in fact, usually fail when static electron correlation effects characterizing quasi-degenerate low-spin states that involve entanglement of many electrons at larger electron-electron separations, which formally requires a multi-configurational description, become prominent. Long-range dispersion interactions, which contribute to various properties of materials, remain a challenge too. Even if we put aside empiricism characterizing the majority of the existing DFT functionals, fundamental problems facing conventional DFT methods in calculations for low-spin electronic states, including the singlet states of the V_B^- defect considered in this work, result in spin contamination and other types of symmetry breaking, leading to uncontrollable accuracy loss that make results difficult to interpret.

Time-dependent DFT (TDDFT) [37] provides the most transparent and practical way to extend the ground-state DFT calculations to excited electronic states, assuming that the reference states employed are themselves not of multi-configurational open-shell character [24]. Otherwise TDDFT can lead to catastrophic failures too [44], especially when two- and other many-electron excitations and charge transfer are involved, and so great care is needed in any application of TDDFT. This includes defects in materials, such as h-BN, that are open-shell in nature, involving perhaps a mix of high-spin and low-spin states with varying degrees of dynamic and static correlations.

Modern extensions to Kohn-Sham DFT that treat multiple electronic configurations involved in low-spin open-shell states on equal footing provide a useful alternative [45-53, 69], but the issues of unphysical spin- and spatial-symmetry breaking and empiricism often remain. A recent calculation [17] for V_B^- provides an example of this type of approach, but the way in which DFT is mixed with CASSCF therein is empirical rather than derived from first-principles DFT. Its predictions are sometimes within 0.02 eV of those presented herein, and sometimes different by over 2 eV (see Tables 3 and 4).

Also, as defect states can involve charge transfer, DFT functionals popular in materials science, such as PBE [54] and HSE06 [55, 56], which do not embody asymptotic correction of the potential, can show dramatic failures for systems closely related to h-BN defects [60], although the appropriately corrected DFT approaches that display an improved long-range behaviour, including the CAM-B3LYP method [57-59] used in this study, exist. Nevertheless, they do not address the aforementioned issues facing DFT in cases involving strong static electron correlation effects, or problems with the use of TDDFT in describing many-electron excitations. In general, we have to keep in mind that in the case of DFT and TDDFT calculations, which are undoubtedly very appealing due to low computational costs and capable of delivering useful results for some defects, it is usually very difficult to estimate their reliability, with, *e.g,* HSE06 shown to undergo catastrophic failure for the V_N^- defect in h-BN, predicting low-energy charge-transfer bands with excitation energies that scale with sample size [70].

The current state of play for defects embedded in extended systems, whether in 2 or 3 dimensions, is particularly problematic: implementations of advanced wavefunction based *ab initio* methods in periodic boundary conditions are very rare, but by contrast there are a number of implementations of DFT/TDDFT with various functionals including HSE06. Hence wavefunction-based approaches are usually applied to model compounds and mostly ignore long-range effects such as dielectric screening, something that is more problematic for defects embedded in 3D crystals compared with 2D ones for which dielectric-screening effects saturate at relatively short distance.

The recent report on multi-reference DFT applied to the NV defect in diamond represent promising paths forward [69].

B. Coupled-cluster methods

For defect spectroscopy, there is also no universally reliable, computationally feasible, method that is *ab initio* in nature, *i.e.*, forms part of a hierarchy of methods that converges, in well-identified limits, to the exact answer. Coupled-cluster singles and doubles (CCSD) [61-65] theory, with perhaps perturbative correction for triples (CCSD(T)) [66], is very reliable for closed-shell systems, a situation which may or may not apply to defect states of interest, and these approaches therefore suffer from the same problems as do DFT approaches. Inclusion of triples excitations often appears necessary for accuracy beyond *ca.* 0.3 eV, but if this is performed perturbatively, as in CCSD(T), then possible low-energy denominators, as often arise in open-shell systems, can lead to catastrophic failure of the method. Methods analogous to TDDFT that expand excited states in terms of some reference can adequately deal with open-shell states, provided that the reference state is properly represented. The most commonly available approach of this type is equation-of-motion CCSD (EOMCCSD) [36].

In this work, the name "EOMCCSD" is reserved for approaches that preserve the number of electrons associated with excitation, but other types of EOMCC approaches that add electrons to or subtract electrons from the underlying closed-shell core are available as well. These particle-non-conserving EOMCC models are especially useful in calculations of ionisation potentials, electron affinities, and electronic spectra of radicals, biradicals, and other open-shell systems having one or two electrons or holes outside the closed-shell core. In particular, one can design the double-ionisation-potential EOMCC methods [26-31], including those used in the present work, abbreviated as DIP-EOMCC or DIP, for short, which allow one to remove two electrons from the closed-shell core, described in our calculations by the single-reference CCSD theory, while relaxing the remaining electrons through suitably defined operators acting on the CCSD reference state. The basic approximation in this category, abbreviated as DIP-EOMCC(3*h*-1*p*) or DIP(3*h*-1*p*), which is also a workhorse method for this study, is obtained by diagonalizing the effective Hamiltonian of CCSD in the space spanned by 2-hole and 3-hole–1-particle configurations relative to the reference determinant defining the closed-shell core [28-31]. In the case of the V_B^- defect in h-BN, the closed-shell core is defined by the V_B^{3-} system; see Section S7. The next level, abbreviated as DIP-EOMCC(4*h*-2*p*) or DIP(4*h*-2*p*) is the highest level implemented so far and used in this work. In it, one diagonalizes the effective Hamiltonian of CCSD in the space spanned by 2-hole, 3-hole–1-particle, and 4-hole–2-particle configurations [30, 31]. The DIP-EOMCC methods, which are directly applicable to the singlet and triplet manifolds of V_B^-, are particularly useful in this study, since an appropriate single-determinant closed-shell reference for the singlet manifold of the V_B^- defect in h-BN does not exist, rendering the conventional particle-conserving EOMCCSD approach inapplicable. Herein we focus on applying the DIP-EOMCC methods to the singlet manifold as other reliable methods are available for the triplet states. Unfortunately, no gradient code for geometry optimisation is currently available.

C. CASSCF-based methods

Other types of calculations that are applicable to both the triplet and singlet manifolds of V_B^- defect in h-BN are multi-reference technologies bases on CASSCF [32-34] approaches, including CASPT2 [67, 68] and MRCI [35] calculations. Unfortunately, various technical difficulties hamper these approaches, with the result that useful, indicative, results can typically be readily obtained, whereas accurate results with boundable error limits are troublesome.

First, an active space must be defined that is continuous over all scenarios of interest and includes all orbitals involved in static electron correlation. In our calculations, calculations using 10 electrons placed in 6 orbitals, as described in Fig. 3 and known as "CAS(10,6)", encompass the most critical

effects in a way that is insensitive to both basis set and sample size, achieving this goal. Nevertheless, strongly coupled orbitals in both the occupied and unoccupied spaces also contribute, with CAS(10,28) being needed at the next level. Approaches to CASSCF such as density matrix renormalisation group (DMRG) theory can make such approaches feasible and have been applied [17] to V_B^-, but nevertheless misrepresent the dynamic electron correlation that, in general, is believed to be important in defects.

Another technical issue is the need to perform state-averaged calculations, optimised to provide the best simultaneous description of multiple states rather than just the best description of the state of present interest. We perform geometry optimisations for single states, but use state averaging whenever possible to provide a more equal description of degenerate state pairs. Unfortunately, CASSCF-based approaches are not guaranteed to predict equal energies for degenerate-state components at D_{3h} symmetry, as are properly conceived TDDFT and EOMCC/EOMCCSD approaches.

In boundable CASSCF-based approaches, convergence of results with respect to active-space choice and weightings choice needs to be demonstrated, something that often proves difficult. CASSCF usually does not adequately include dynamic electron correlation. The simplest improved method is CASPT2 [68] include it perturbatively, a potentially hazardous procedure for defects as low-energy states are often strongly coupled. Beyond this, MRCI approaches [35] properly include low-energy states but do so in a manner that is not size consistent, meaning that results can degrade as the sample size increases. We use the Davidson correction throughout to correct for this. Mostly, MRCI results are less sensitive to variations in active space and state weightings than are the original CASSCF calculations, but determination of meaningful likely error bounds is still problematic.

S2. OBSERVED PHOTOLUMINESCENCE SPECTRA AND THEIR INTERPRETATION USING A HUANG-RHYS-MODEL

Spectra observed from three h-BN samples are shown in FIG. S1 where they are analysed for their spectral properties. Clearly, emission occurs from a large ensemble of defects and is dissimilar to the single-photon emission often seen from h-BN samples. The emission is also unusual in that it is very weak in intensity. A critical question of interest concerns the intrinsic bandshape of each individual emitter, specified here by the emission reorganisation energy λ^E defined as the energy of the zero-phonon line (or vibronic origin) E_{00}, less the average energy of emission [11].

Upper bounds for λ^E can be obtained by fitting the observed spectra to a thermal Huang-Rhys model specified by various vibration frequencies and their degree of excitation (see TABLE S1 for details). This approach assumes that all observed emission can be attributed to a single pair of non-degenerate electronic states on a single emitter, ignoring the inhomogeneous broadening that would arise from the known ensemble of emitters, as well as possible multiple emission processes within the one defect. Further, as detailed elsewhere [11], this approach embodies five key approximations: the Born-Oppenheimer approximation, the harmonic-oscillator approximation, the assumption that the vibration frequencies are the same on the initial and final electronic states, the neglect of Duschinsky rotation, and the Condon approximation. All of these approximations are likely to fail for defects in general and for V_B^- in particular owing to the possible operation of the Jahn-Teller effect.

The observed emission spectra shown in FIG. S1 present primary emission maxima near 1.6 eV, with small tails to low energy and significant and variable tails to high energy. The high-energy emission could not arise from the same spectral system on the same defect as does the other emission and is not included in this analysis. The spectrum analysed in FIG. S1(c) was taken at 77 K and its central and low-energy components can readily be interpreted as emission from a single state of a single defect with λ^E up to 0.046 eV. The 295 K spectrum in FIG. S1(b) can also be fitted in this manner by values of λ^E up to 0.058 eV, although emission details do suggest emission from defects with varying environments. FIG. S1(a) shows features of its low-energy tail that are strongly suggestive of multiple emission sites, with fitting of the band to a 1-site model yielding λ^E up to 0.093 eV.

Combining all data, the largest conceivable reorganisation energy at 0 K consistent with a Huang-Rhys model is 0.05 eV, with interpretations for which λ^E is an order of magnitude smaller also being possible. Such values within the range of traditional "Group-1" (0.06 – 0.16 eV) and "Group-2" (0.015 – 0.030 eV) h-BN single-photon emitters [11]. The significance of these results comes from computational modelling studies of proposed defects, for which calculated values range from 0.2 to 2.5 eV; [11, 24] envisaging defects with reorganisation energies consistent with experiment is a difficult task, making this properties very important when it comes to defect identification.

Considering the observed data for what range of origin energies E_{00} it depicts, values from 1.3 to 2.0 eV appear feasible. This range could depict local site variations inducted by strain or Stark fields, and/or emission from multiple states within the same defect. Alternative explanations of the emission are also possible.

A major limitation of the presented analysis is that it follows the basic predictions of the Huang-Rhys model that the ZPL is intense and located within the main observed band. Later, we show that this expectation does not follow if a Jahn-Teller model is used to interpret the spectra. The Jahn-Teller model instead sees the ZPL as a forbidden transition located in the high-energy tail of the emission. Another limitation of this analysis is that the contributions from acoustic phonons are implicitly treated within the inhomogeneous broadening. If the inherent Lorentzian lineshape was apparent, then the extracted reorganisation energy corresponds only to the contribution from the optical phonons, with analysis of the lineshape needed to determine the contribution of acoustic phonons to the reorganisation energy.

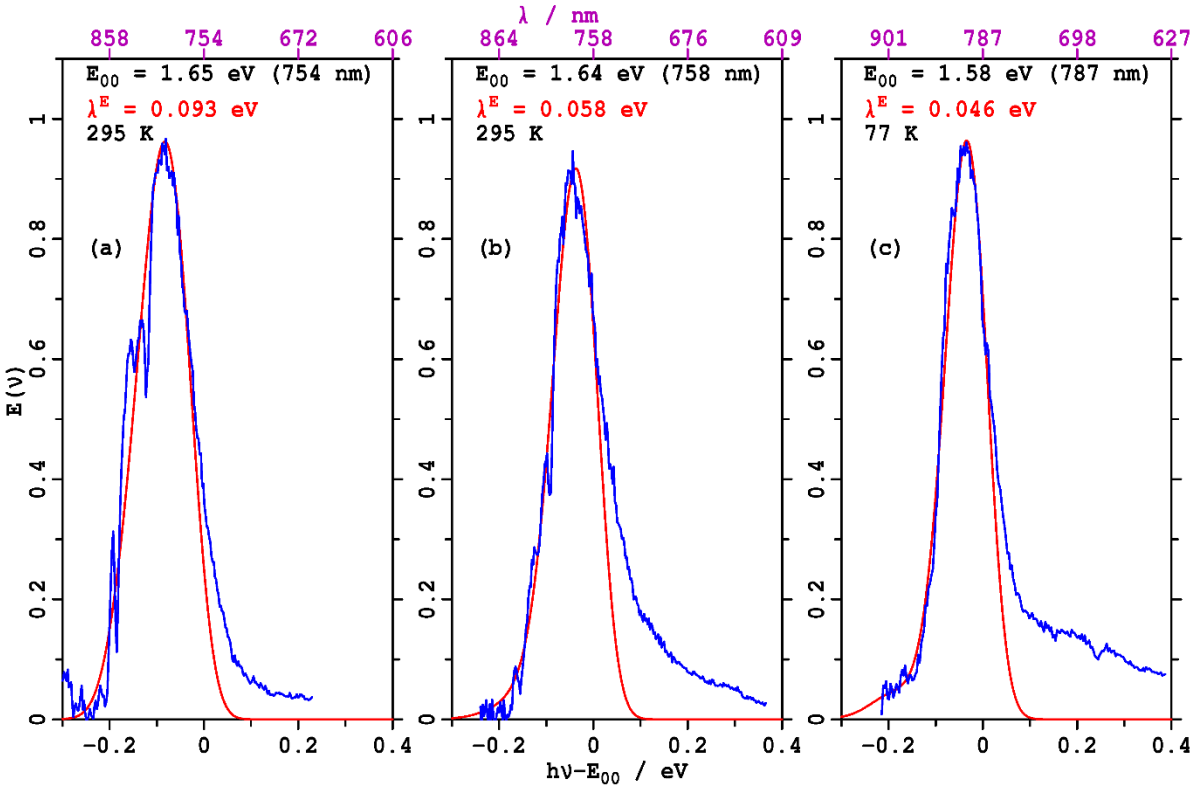

FIG. S1. Three sets of observed photoluminescence band contours $E(\nu)/\nu^3 \propto \lambda^5 E(\lambda)$ (blue) of the V_B^- defect of h-BN, interpreted in terms of Huang-Rhys models (red) that manifest the largest possible values of the emission reorganisation energies λ^E.

TABLE S1. Parameters in the Huang-Rhys models used to fit the observed photoluminescence spectra shown in FIG. S1: σ- Gaussian inhomogeneous broadening, δ- dimensionless displacement, S- Huang Rhys factor, λ^E- contribution to the emission reorganisation energy, DW- Debye-Waller factor.

(a) T = 295 K, σ = 250 cm^{-1}				(b) T = 295 K, σ = 250 cm^{-1}				(c) T = 77 K, σ = 275 cm^{-1}			
ν / cm^{-1}	δ	λ^E / eV	S	ν / cm^{-1}	δ	λ^E / eV	S	ν / cm^{-1}	δ	λ^E / eV	S
400	0.3	0.002	0.05	1200	0.2	0.003	0.02	1300	0.28	0.006	0.04
200	2.7	0.090	3.65	200	2.1	0.055	2.21	200	1.8	0.040	1.62
total		0.093	3.69	total		0.058	2.23	total		0.046	1.66
DW			2 %				11 %				19 %

S3. CONVERGENCE OF DFT CALCULATIONS

The relative energies of 10 triplet states and 3 singlet states of the V_B^- defect in h-BN, at both the optimised geometry of $(1)^3A_2'$ and their individual optimised geometries, are compared subject to changes in computational procedure, with results summarised in TABLE S2 and listed in detail in TABLE S3 and TABLE S4. First, calculations are performed using the CAM-B3LYP density functional [57-59] and the 6-31G* basis set [80] on the 1 - 6 ring model systems shown in Fig. 1. Also, in a variant of the 3D structure, long range dielectric effects are included using a self-consistent reaction field model. The conclusion reached is that the 2-ring 1-layer model compound is useful for the consideration of relative state energies. For the triplet states, on average, the correction needed to be applied to correct state energies for expansion to 6 rings and the inclusion of nearby bulk h-BN is -0.01±0.07 eV. Henceforth calculations on the 2-ring model compound are taken to provide an adequate description of electronic energies, with corrections (TABLE S2) applied to mimic the crystalline material. The convergence of the reorganisation energy, and with it vibrational properties, with sample size is much slower and is discussed in detail later.

The smaller 1-ring model compound is found to predict energies to within 0.1 eV in many instances, but in others changes of several eV are found. This occurs as the 1-ring compound is able to undergo large-scale structural rearrangements to facilitate bond making and hence defect healing. If the geometry used is indicative of structures feasible in h-BN flakes, then the energetics of the key transitions are predicted to usable accuracy, however. In this work, QM/MM approaches using 1-ring only in the QM part are not used, but such an approach may indeed provide a computationally efficient and widely applicable approach for considering defect spectroscopy.

TABLE S2. Average and standard-deviation corrections for the energy difference to the $(1)^3A_2'$ minimum to add to lower-level approaches to simulate higher-level ones, in eV, averaged over the $(1)^3E''$ $i.e.$ $(1)^3A_2$ and $(1)^3B_1$, $(1)^3A_1''$ $i.e.$ $(2)^3A_2$, $(1)^3E'$ $i.e.$ $(1)^3A_1$ and $(2)^3B_2$, $(1)^1E'$ $i.e.$ $(1)^1A_1$ and $(1)^1B_2$, and $(1)^1A_1'$ $i.e.$ $(2)^1A_1$ states.[a]

from	to	vertical, all data		adiabatic, all data		adiabatic, no $(1)^1A_1$	
		ave	stdev	ave	stdev	ave	stdev
1 ring	2 ring	0.17	0.40	0.14	1.02	-0.89	
2 ring	6 ring (triplets), 3 ring (singlets)	0.02	0.04	0.06	0.05	0.06	0.05
1 layer	3 layers	-0.02	0.03	0.00	0.04	-0.03	0.01
3 layers	crystal	-0.03	0.03	-0.04	0.14	0.03	0.01
6-31G*	cc-pVTZ	0.00	0.04	-0.03	0.13	-0.03	0.06
6-31G	cc-pVTZ	-0.08	0.06	-0.11	0.06	-0.13	0.04
STO-3G	cc-pVTZ	-0.24	0.19	0.04	0.22	-0.12	0.03
HSE06	CAM-B3LYP	0.13	0.10	0.08	0.11	-0.08	0.01
CAM-B3LYP/6-31G*/1-ring	CAM-B3LYP/cc-pVTZ/crystal	0.15	0.39	0.61	0.69	0.92	0.02
CAM-B3LYP/6-31G*/2-ring	CAM-B3LYP/cc-pVTZ/crystal	-0.02	0.07	0.03	0.17	0.04	0.03
CAM-B3LYP/6-31G/2-ring	CAM-B3LYP/cc-pVTZ/crystal	-0.10	0.10	-0.05	0.14	-0.06	0.07
HSE06/6-31G*/2-ring	CAM-B3LYP/cc-pVTZ/crystal	0.10	0.14	0.10	0.20	-0.05	0.03

a: In these DFT calculations, the $(1)^1A_1$ state is taken to have a doubly occupied a_1 orbital, the $(2)^1A_1$ state is taken to have a doubly occupied b_2 orbital, and the energy of the $(1)^1B_2$ state is taken to be twice the energy of the determinant with singly occupied a_1 and b_2 orbitals less that of the corresponding triplet state.

TABLE S3. Triplet excited state energies relative to $(1)^3A_2'$ for the V_B^- defect of h-BN, and corrections intended to correct CAM-B3LYP (CAM) 6-31G* calculations on the 2-ring model compound to cc-pVTZ calculations on a 4 or 6 ring defect imbedded in h-BN crystal, in eV.

METHOD	CAM QM/MM	CAM QM/MM	CAM QM/MM	CAM QM/MM	CAM	CAM	CAM	CAM	CAM	CAM	CAM	CAM	CAM	CAM	CAM	HSE06	CAM
BASIS	6-31G*	6-31G*	6-31G*	6-31G*	6-31G*	6-31G*	6-31G*	6-31G*	6-31G*	cc-pVTZ	6-31G*	6-31G*	6-31G	STO-3G	6-31G*	6-31G*	corr.
RINGS	30	20	10	5	6	5	4	3	2	2	2	2	2	2	1	2	
LAYERS	1	1	1	1	1	1	1	1	1	1	3	3 SCRF	1	1	1	1	
Vertical absorption energies ΔE_v^A at D_{3h}-symmetric geometry of the to $(1)^3A_2'$ state																	
$(1)^3E''$					2.00	1.99	1.99	2.00	1.99	2.04	2.01	1.98	2.14	2.05	1.92	1.90	0.05
$(1)^3A_1''$					2.04	2.03	2.03	2.05	2.08	2.10	2.05	2.05	2.28	2.43	2.52	2.02	-0.05
$(1)^3E'$					2.83	2.83	2.83	2.82	2.76	2.69	2.75	2.66	2.78	3.14	1.94	2.74	-0.10
Adiabatic transition energies ΔE_0																	
$(1)^3A_2$	1.743	1.743	1.743	1.740	1.73	1.73	1.72	1.71	1.67	1.72	1.67	1.67	1.84	1.63	1.55	1.64	0.11
$(1)^3B_1$					1.89	1.89	1.88	1.87	1.85	1.90	1.87	1.88	2.01	1.84	1.63	1.75	0.12
$(1)^3A_1''$					2.02	2.00	2.00	2.01	2.04	2.06	2.00	2.00	2.24	2.37	2.42	1.97	-0.04
$(2)^3A_2$					1.93	1.93	1.92	1.92	1.92	1.96	1.91	1.94	2.13	-[b]	-[b]		0.07
$(1)^3A_1$							2.31	2.29	2.21	2.14	2.17	2.21	2.25	2.28	1.32	2.29	0.01
$(2)^3B_2$							2.33	2.31	2.21	2.15	2.18	2.21	2.25	2.25	1.32	2.28	0.04
Absorption reorganisation energies λ^A																	
$(1)^3A_2$					0.27	0.26	0.27	0.29	0.32	0.32	0.34	0.31	0.30	0.42	0.37	0.26	-0.07
$(1)^3B_1$					0.11	0.10	0.11	0.13	0.14	0.14	0.14	0.11	0.13	0.21	0.29	0.15	-0.07
$(1)^3A_1''$					0.01	0.03	0.03	0.04	0.04	0.04	0.05	0.05	0.04	0.06	0.10	0.05	-0.02
$(2)^3A_2$					0.10	0.10	0.11	0.13	0.16	0.14	0.14	0.11	0.15		-		-0.13
$(1)^3A_1$							0.52	0.53	0.55	0.55	0.58	0.45	0.53	0.86	0.62	0.45	-0.12
$(2)^3B_2$							0.14	0.51	0.55	0.54	0.57	0.45	0.53	0.89	0.62	0.46	-0.15
Emission reorganisation energies λ^E																	
$(1)^3A_2$	0.257	0.257	0.260	0.269	0.27	0.27	0.28	0.29	0.33	0.32	0.32	0.33	0.32	0.40	0.34	0.30	-0.08
$(1)^3B_1$					0.10	0.10	0.11	0.11	0.13	0.13	0.13	0.15	0.13	0.18	0.30	0.18	-0.01
$(1)^3A_1''$					0.04	0.04	0.04	0.04	0.05	0.07	0.05	0.05	0.04	0.06	0.10	0.05	0.01
$(2)^3A_2$					0.10	0.10	0.11	0.11	0.12	0.12	0.12	0.17	0.14		-		0.03
$(1)^3A_1$							0.40	0.40	0.42	0.41	0.44	0.51	0.40	0.58	0.39	0.33	0.06
$(2)^3B_2$							0.38	0.38	0.41	0.39	0.42	0.51	0.40	0.60	0.39	0.34	0.05

a: Two minima pertaining to $(2)^3A_2$ have been found, differing by mixing with a state barely considered in this work, $(3)^3A_2$. This table shows results for the higher-energy one whereas Table III shows the lower energy one, for which the absorption-emission symmetry is enhanced.
b: collapses to $(1)^3A_2$.

TABLE S4. Extended CAM-B3LYP/6-31G* vertical excitation energies ΔE_v^A from the $(1)^3A_2'$ ground state for 1-6 ring compounds.[a]

state	1	2	3	4	5	6
$(1)^3E''$	1.92	1.99	2.00	1.99	1.99	2.00
$(1)^3A_1''$	2.52	2.08	2.05	2.03	2.03	2.04
$(1)^3E'$	1.94	2.76	2.81	2.83	2.83	2.83
$(1)^3A_2''$	3.98	3.70	3.67	3.65	3.65	3.67
$(2)^3E''$	3.84	3.67	3.67	3.66	3.66	3.68
$(2)^3A_2''$	4.17	5.08	4.95	4.91	4.91	4.94
$(3)^3E''$	5.17	4.94	4.97	4.94	4.94	4.97
$(4)^3E''$	5.60	5.74	5.46	5.43	5.43	5.47
$(1)^3A_1'$	5.38	5.56	5.57	5.55		
$(2)^3A_1''$	5.60	5.49	5.63	5.57		

a: For 1 – 4 ring compounds, 25 roots were obtained and the lowest 13 listed in this table; only 13 roots were obtained for the 5 and 6 ring compounds.

TABLE S5. Singlet excited state energies relative to $(1)^3A_2'$ for the V_B^- defect of h-BN, and corrections intended to adjust CAM-B3LYP (CAM) 6-31G* calculations on the 2-ring model compound to mimic cc-pVTZ calculations on the defect imbedded in h-BN crystal, in eV.

METHOD		CAM	CAM	CAM	CAM	CAM	CAM	CAM	CAM	HSE06
BASIS		6-31G*	6-31G*	cc-pVTZ	6-31G*	6-31G*	6-31G	STO-3G	6-31G*	6-31g*
RINGS		3	2	2	2	2	2	2	1	2
LAYERS		1	1	1	3	3 SCRF	1	1	1	1
Vertical absorption energies ΔE_v^A										
$(1)^1E$	$(1)^1A_1$	2.75	2.74	2.72	2.67	2.64	2.79	3.17	2.57	2.53
	$(1)^1B_2$	1.07	1.06	1.05	1.05	1.05	1.07	1.15	0.85	0.97
$(1)^1A_1'$	$(2)^1A_1$	2.24	2.21	2.23	2.20	2.19	2.23	2.34	2.02	1.93
Adiabatic transition energies ΔE_0										
	$(1)^1A_1$	1.21	1.05	0.70	1.10	0.71	0.84	0.30	-1.27	0.85
	$(1)^1B_2$	0.67	0.63	0.63	0.67	0.61	0.68	0.51	0.18	0.47
	$(2)^1A_1$	1.64	1.54	1.57	1.56	1.58	1.56	1.36	1.40	1.34
Absorption reorganisation energies λ^A										
	$(1)^1A_1$	1.54	1.69	2.03	1.56	1.94	1.95	2.87	3.84	1.68
	$(1)^1B_2$	0.40	0.42	0.42	0.38	0.44	0.38	0.63	0.66	0.50
	$(2)^1A_1$	0.60	0.67	0.66	0.65	0.61	0.67	0.99	0.62	0.59

S4. DETAILED CALCULATED PROPERTIES OF THE TRIPLET MANIFOLD

More computed energetics of the triplet manifold are listed in Table S6. Calculated zero-point energy corrections are less than 0.03 eV; these are not significant in the present context and so not discussed for brevity. Hence observed values for ΔE_{00} are compared to computed values for ΔE_0.

A noteworthy difference between the CAM-B3LYP results and those from CASSCF and CCSD as these methods predict that the ground state $(1)^3A_2'$ distorts to $(1)^3B_2$ in C_{2v} symmetry, with the effect decreasing in expanding from the 1-ring compound to the 2-ring one. Single-point energy calculations performed using MRCI and CCSD(T) at the related low-symmetry geometries indicate increases in energy compared to $(1)^3A_2'$, however, suggesting that these more advanced methods prefer high-symmetry instead. Regardless, it is clear that the defect can undergo certain large-scale changes in geometry at little energy cost, an important qualitative feature.

TABLE S6. Additional energy differences of the triplet states with respect to the $(1)^3A_2'$ D_{3h}-symmetric minimum, in eV.[a]

METHOD		CCSD	CCSD	CCSD(T)	CASSCF (10,6)	MRCI (10,6)	CCSD	CCSD(T)	EOMCCSD	EOM-CCSD	EOM-CCSD	CASSCF (10,6)	MRCI (10,12)	MRCI (10,6)
BASIS		6-31G*	STO-3G	STO-3G	6-31G*	6-31G*	6-31G*	6-31G*	6-31G*	6-31G*	6-31G	STO-3G	STO-3G	STO-3G
RINGS		2	2	2	1	1	1	1	1	1	1	1	1	1
LAYERS		1	1	1	1	1	1	1	1	1	1	1	1	1
GEOMETRY		CASSCF	CASSCF	CASSCF	CASSCF	CASSCF	CASSCF	CASSCF	CAM-B3LYP	CCSD	CCSD	CASSCF	CASSCF	CASSCF
Vertical absorption energies ΔE_v^A														
$(1)^3E''(D_{3h})$	$(1)^3A_2(C_{2v})$	2.02	2.11	2.09	1.86	2.03	2.06	2.05	2.06	1.94	2.11	2.32	2.20	2.45
	$(1)^3B_1(C_{2v})$		2.19	2.16	1.35	2.19	2.12	2.08	2.06	1.94	2.11	2.39	2.18	2.29
$(1)^3A_1''(D_{3h})$	$(2)^3A_2(C_{2v})$				2.49				2.71	2.55	2.88			
$(1)^3E'(D_{3h})$	$(1)^3A_1(C_{2v})$		2.44	2.38	2.20	2.17	2.22	2.19	1.93	1.91	2.01			
	$(2)^3B_2(C_{2v})$								1.93	1.91	2.01			
Adiabatic transition energies ΔE_0														
$(1)^3A_2$					1.16	1.38	1.43	1.48			1.74	0.95	1.31	1.12
$(1)^3B_1$					0.67	1.63	1.50	1.47			1.80	1.45	1.49	1.42
$(2)^3A_2$					2.10						2.78			
$(1)^3A_1$					1.34	1.42	1.41	1.38			1.40			
$(2)^3B_2$											1.42			
Absorption reorganisation energies λ^A														
$(1)^3A_2$					0.70	0.65	0.63	0.57			0.37	1.37	0.88	1.32
$(1)^3B_1$					0.69	0.56	0.62	0.61			0.31	0.95	0.69	0.87
$(2)^3A_2$					0.39						0.10			
$(1)^3A_1$					0.86	0.75	0.80	0.81			0.61			
$(2)^3B_2$											0.59			
Emission reorganisation energies λ^E														
$(1)^3A_2$											0.36	0.27		
$(1)^3B_1$											0.32			
$(2)^3A_2$											0.10			
$(1)^3A_1$														
$(2)^3B_2$											0.36			

a: All CASSCF and MRCI results are for individually weighted states, except for $(2)^3A_2$ and $(2)^3B_2$ for which 50:50 weighting is used with the lower-energy state of that symmetry.

S5. DIPOLE MOMENT CHANGES ON EXCITATION AND THE STARK EFFECT

TABLE S7 lists the dipole moments of the primary electronic states considered, calculated using CASSCF(10,6)/6-31G*, relative to that for $(1)^3A_2'$ which is taken to be zero (the dipole-moment is origin dependent as the defect is charged). Dipole moment changes of up to 7 D are predicted, indicating that spectral energies will be influenced by Stark shifts and by long-range dielectric interactions. For a Stark shift of 0.1 eV and a dipole change of 5 D, the required electric field strength would be 0.002 au = 0.09 VÅ^{-1}, a very substantial value. Field strengths of this order would require either ordered arrays of charges, which would seem to be unlikely, or else to have the V_B^- defect ion-paired with an adjacent counterion.

Also, the change in dipole moment that occurs during a transition can interact with the long-range dielectric material in the h-BN to shift transition energies. The self-consistent reaction-field calculations reported in TABLE S3 directly model this effect, yet yield no noticeable influence. Those calculations pertain to emission to the symmetric $(1)^3A_2'$ state, and hence may underestimate the effect. Calculation performed at other geometries that do involve large initial-state and final-state dipoles also show little effect. If the defect was neutral, then such dipole changes would result in large solvent shifts induced by the environment, but for V_B^- the dielectric response is always dominated by the net charge, nullifying the effect of the charge redistribution.

TABLE S7. State dipole moment changes from $(1)^3A_2'$ at individually optimised geometries calculated using CASSCF(10,6/6-31G*) on the 2-ring model compound of the V_B^- defect in h-BN.

State	Dipole moment / D
$(1)^3A_2'$	[0]
$(1)^3A_2$	-3.7
$(1)^3B_1$	5.9
$(1)^3A_1''$	0
$(2)^3A_2$	-1.6
$(1)^3A_1$	-2.7
$(2)^3B_2$	6.5
$(1)^1B_2$	-2.5
$(1)^1A_1$	5.1
$(1)^1A_2$	-3.7
$(1)^1B_1$	5.8
$(2)^1A_2$	5.8
$(2)^1A_1$	6.7

S6. FAILURE OF SINGLE-REFERENCE METHODS FOR TREATING SINGLET STATES

Calculated energies for the singlet states obtained using DFT are listed in TABLE S5, whilst those obtained using *ab initio* approaches are listed in TABLE S8. These results indicate errors of up to 2 eV in establishing the degeneracy of the two components ($(1)^1A_1$ and $(1)^1B_2$) of the $(1)^1E'$ state at the D_{3h} ground-state geometry, as well as failure to establish the large energy splitting between the $(1)^1A_1$ and $(2)^1A_1$ states. DFT geometry optimisations on $(1)^1A_1$ lead to B-B bond formation within the defect, whereas CASSCF calculations lead to increased B-B separations, an effect confirmed by MRCI and EOMCC calculations. Indeed, the ability to reform bonds often leads to substantial differences between results for the 1-ring and 2-ring model compounds, but 2-ring results are found to be in good agreement with 3-ring ones. Methods based on TDDFT or EOMCCSD descriptions of states in terms of excitations from a closed-shell reference are also expected to perform poorly as no suitable reference determinant is obvious, although the DFT results for $(1)^1B_2$ singlet-biradical state are qualitatively indicative and empirical schemes based on this feature could be envisaged.

TABLE S8. Failure of single-reference *ab initio* methods to depict key qualitative properties of the low-energy singlet manifold of V_B^-, as evidenced from calculated energy differences with respect to the $(1)^3A_2'$ D_{3h}-symmetric minimum, in eV.

state	ΔE_v^A			ΔE_0			λ^A		
	CCSD 6-31G* 2 rings	CCSD 6-31G* 1 ring	CCSD(T) 6-31G* 1 ring	CCSD 6-31G* 2 rings	CCSD 6-31G* 1 ring	CCSD(T) 6-31G* 1 ring	CCSD 6-31G* 2 rings	CCSD 6-31G* 1 ring	CCSD(T) 6-31G* 1 ring
$(1)^1A_1$	2.03	1.80	0.96	1.59	1.41	0.23	0.44	0.39	0.73
$(2)^1A_1$	2.12	1.91	1.00	2.17	1.77	0.35	-0.05	0.14	0.64

S7. DIP-EOMCC calculations for the singlet manifold

In this section, we provide details pertinent to the calculations of singlet states evaluated using the particle-non-conserving DIP-EOMCC methodology. This approach is specifically designed to handle multiconfigurational states that can formally be obtained by removing two electrons from a parent closed-shell core. This expands on the information provided in Table IV and also encompasses many more singlet states.

To model states of V_B^- using DIP-EOMCC, a reference wavefunction pertaining to V_B^{3-} must be generated. From Fig. 3, this reference wavefunction is seen to occupy *all* defect orbital levels within the h-BN band gap. It is therefore expected to be mostly closed-shell in character and hence provide a good starting point for the description of the states of V_B^-. High-level dynamical correlations are modelled in an accurate manner through the CC and EOMCC ansätze. This provides a size extensive description of the CC reference state (we use CCSD to describe it), as well as a size intensive description of the EOMCC double ionisation and excitation energies. The extent of correlation captured by the DIP-EOMCC calculations is indicated through the *nh*-*mp* notation that indicates that all possible states with up to *n* holes (electrons removed from the V_B^{3-} reference) and $m = n–2$ particles (electrons added to orbitals not occupied in the V_B^{3-} reference) are included on top of the CCSD description of the closed-shell core. The simplest level of approximation, 2*h*-0*p*, provides information about the leading electron configurations responsible for the relevant non-dynamical correlations, such as those seen in Fig. 4, and some core correlation effects. The information about dynamical correlation effects, especially those dominated by one-electron excitations from a multi-configurational reference space and those outside the CCSD core correlations, is captured by the next, more quantitative, 3*h*-1*p* level, which is the main workhorse of this study. In order to confirm the reliability of the corresponding DIP-EOMCC(3*h*-1*p*) calculations, we also examined the highest currently implemented [30, 31] 4*h*-2*p* theory level, with 4*h*-2*p* correlations outside the CCSD core treated using active orbitals to reduce computational costs, which captures the single as well as double excitations from a multi-configurational reference space and various higher-order terms resulting from the use of the CC exponential ansatz. The active space used in the DIP-EOMCC(4*h*-2*p*) calculations to identify the leading 4*h*-2*p* terms consisted of the 6 highest orbitals occupied in the V_B^{3-} reference configuration.

Whereas it is difficult to estimate intrinsic errors characterizing the otherwise high-level MRCI calculations owing to their sensitivity to state averaging, active space selection, and size-inextensivity effects, the state-of-the-art DIP-EOMCC calculations reported in Table IV and TABLE S9 - TABLE S11 (*cf.*, also, FIG. S2) seem to be offering a smooth and systematic convergence path towards the exact answers, with error bounds, as further elaborated on below, under reasonable control, allowing us to draw important conclusions regarding the role of singlet-singlet transitions in the observed photoemission spectra displaying ODMR. We should, of course, keep in mind that all calculations were performed at CASSCF-optimised geometries. DFT geometries were found to be unreliable, and MRCI or DIP-EOMCC approaches for geometry optimisations involving the 21-atom 1-ring and the 51-atom 2-ring model systems to which DIP-EOMCC is applied are prohibitively expensive. We believe that the geometries resulting from our CASSCF optimisations correctly capture the key structural features of the various electronic states of the V_B^- defect, which means that it is reasonable to adopt them in single-point calculations using higher MRCI and DIP-EOMCC levels (a common practice in quantum chemistry). With all of this mind, in the discussion below we

TABLE S9. Convergence of DIP-EOMCC calculations for singlet states of V_B^-, showing energies relative to $(1)^3A_2'$ D_{3h}-symmetric minimum, in eV.[a]

EOMCC method	Basis	Rings	Vertical (D_{3h})				Adiabatic (C_{2v})				
			$(1)^1E'$	$(1)^1A_1''$	$(1)^1E''$	$(1)^1A_1'$	$(1)^1B_2$	$(1)^1A_1$	$(1)^1A_2$	$(2)^1A_2$	$(1)^1B_1$
DIP(3*h*-1*p*)[b]	6-31G	1	0.60	2.75	1.96	2.23	0.18	0.20	1.60	1.81	1.87
DIP(4*h*-2*p*)[c]	6-31G	1	0.58	2.87	2.13	2.17	0.27	0.32	1.73	1.98	2.06
DIP(3*h*-1*p*)[b]	6-31G*	1	0.57	2.47	1.79	2.15	0.12	0.16	1.45	1.71	1.78
DIP(4*h*-2*p*)[c]	6-31G*	1	0.56	2.58	1.95	2.10	0.20	0.27	1.58	1.87	1.95
DIP(3*h*-1*p*)[b]	6-31G	2	0.79	2.08	1.92	2.81	0.54	0.61	1.56	1.85	1.89
DIP(4*h*-2*p*)[d]	6-31G*	2	0.75	1.91	1.91	2.68	0.56	0.68	1.54	1.91	1.97

a: All calculations are performed at CASSCF/6-31G* optimised geometries for unweighted single states in either D_{3h} or C_{2v} symmetry.
b: Raw DIP-EOMCC(3*h*-1*p*) data.
c: Raw DIP-EOMCC(4*h*-2*p*) data.
d: Extrapolated DIP-EOMCC results to account for 4*h*-2*p* correlations and the effect of replacing the 6-31G basis set by 6-31G*, see text.

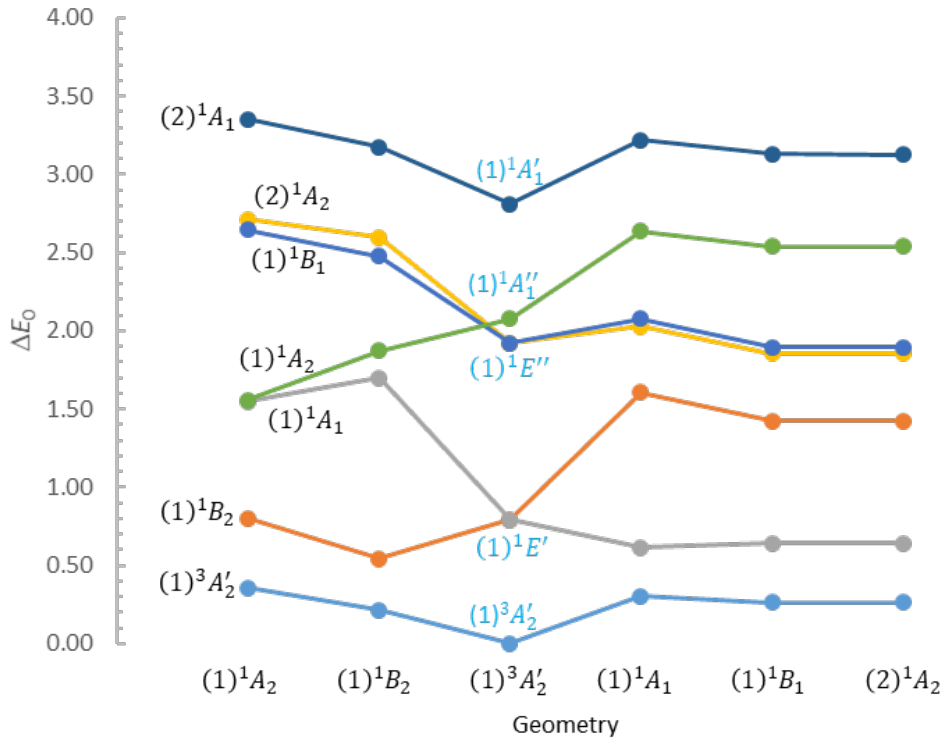

FIG. S2. Ordering of the diabatic states, in eV, relative to the $(1)^3A_2'$ minimum, resulting from the DIP-EOMCC(3*h*-1*p*)/6-31G calculations for the 2-ring system along a fictitious nuclear coordinate that connects the geometries of the triplet ground state and the low-lying singlet excited states optimised with the CASSCF/6-31G* approach. Whereas a rigorous description of the Jahn-Teller distortions characterizing the $(1)^1E'$ and $(1)^1E''$ states would require a minimum of four nuclear coordinates, by projecting all state energies onto the fictitious one-dimensional nuclear coordinate we can highlight both the Jahn-Teller conical intersections and the $(1)^1A_2 - (2)^1A_2$ diabatic crossing. Of note is the small Jahn-Teller distortion characterizing the $(1)^1E''$ state, especially when compared to its $(1)^1E'$ counterpart. The numerical data used to construct the Fig. are based on TABLE S10. State labels in D_{3h} symmetry are presented in blue, those at C_{2v} geometries in black.

TABLE S10. DIP-EOMCC(3*h*-1*p*)/6-31G energy differences for the 2-ring model compound determined at CASSCF/6-31G* optimised geometries, for various states of V_B^-, in eV.[a]

Geometry	Vertical excitation energies from this geometry						
	$(1)^3B_2$	$(1)^1B_2$	$(1)^1A_1$	$(1)^1A_2$	$(2)^1A_2$	$(1)^1B_1$	$(2)^1A_1$
Vertical excitation energies							
$(1)^3A_2'$	[0]	0.79	0.79	2.08	1.92	1.92	2.81
$(1)^1B_2$	-0.33	[0]	1.16	1.33	2.05	1.93	2.63
$(1)^1A_1$	-0.31	0.99	[0]	2.03	1.41	1.46	2.60
$(1)^1A_2$	-1.20	-0.76	-0.01	[0]	1.15	1.09	1.79
$(2)^1A_2$	-1.59	-0.43	-1.22	0.68	[0]	0.04	1.27
$(1)^1B_1$	-1.63	-0.47	-1.26	0.64	-0.04	[0]	1.23
Adiabatic transition energies ΔE_0							
$(1)^3A_2'$	[0]	0.54	0.61	1.56	1.85	1.89	
$(1)^1B_2$	-0.54	[0]	0.07	1.01	1.31	1.35	
$(1)^1A_1$	-0.61	-0.07	[0]	0.94	1.24	1.28	
$(1)^1A_2$	-1.56	-1.01	-0.94	[0]	0.30	0.34	
$(2)^1A_2$	-1.85	-1.31	-1.24	-0.30	[0]	0.04	
$(1)^1B_1$	-1.89	-1.35	-1.28	-0.34	-0.04	[0]	
Reorganisation energies λ							
$(1)^3A_2'$	[0]	0.25	0.18	0.52	0.06	0.02	
$(1)^1B_2$	0.21	[0]	1.09	0.31	0.74	0.58	
$(1)^1A_1$	0.30	1.06	[0]	1.08	0.17	0.18	
$(1)^1A_2$	0.36	0.26	0.93	[0]	0.86	0.75	
$(2)^1A_2$	0.26	0.88	0.03	0.98	[0]	0.00	
$(1)^1B_1$	0.26	0.88	0.03	0.98	0.00	[0]	

a: The matrix depicting the adiabatic transition energies is antisymmetric, with negative energies representing emission and positive energies representing absorption; as a result, the corresponding elements of the reorganisation energy matrix are emission reorganisation energies, λ^E, and absorption reorganisation energies, λ^A, respectively. Based on the reflection approximation, the reorganisation energy matrix is expected to be symmetric, with deviations from symmetry most likely indicative of the effects of Duschinsky rotation of the form of the normal coordinates of vibration between the two states [11]. The closeness of the reorganisation matrix to symmetric form is indicative of the accuracy in the use of diabatic labels to describe the adiabatic states produced by the electronic-structure calculations. The adiabatic transition energies, expressed relative to the $(1)^3A_2'$ D_{3h} minimum, are depicted in FIG. S2.

TABLE S11. Energy differences characterising singlet states of the V_B^- defect in h-BN with respect to the $(1)^3A_2'$ D_{3h}-symmetric minimum, in eV,[a] for the 2-ring model compound, with also a crude estimate at the correction energy appropriate for a 5-ring compound using QM/MM.

State		CASSCF	MRCI	DIP($3h$-$1p$)[b]	DIP($4h$-$2p$)[c]	QM/MM corr.	DIP($4h$-$2p$)[c] after QM/MM corr.
		6-31G*	6-31G*	6-31G	6-31G*	6-31G*	6-31G*
Vertical absorption energies ΔE_v^A							
$(1)^1E'(D_{3h})$	$(1)^1A_1(C_{2v})$	1.14[de]		0.79	0.75		
	$(1)^1B_2(C_{2v})$	1.14[de]	0.95[e]	0.79	0.75		
$(1)^1A_1''(D_{3h})$	$(1)^1A_2(C_{2v})$			2.08	1.91		
$(1)^1E''(D_{3h})$	$(2)^1A_2(C_{2v})$	1.47[de]		1.92	1.91		
	$(1)^1B_1(C_{2v})$	1.41[de]		1.92	1.91		
$(1)^1A_1'(D_{3h})$	$(2)^1A_1(C_{2v})$	1.42[f]	1.95[f]	2.81	2.68		
Adiabatic transition energies ΔE_0							
$(1)^1A_1$[g]		0.46[e]	0.53[eh]	0.61	0.68	0.32	1.00
$(1)^1B_2$		0.25[e]	0.36[eh]	0.54	0.56	0.28	0.84
$(1)^1A_2$		1.35[f]	1.51[f]	1.56	1.54	0.55	2.09
$(2)^1A_2$		0.89[e]	1.54[e]	1.85	1.91	0.37	2.28
$(1)^1B_1$[g]		0.94[e]	1.59[f]	1.89	1.97	0.37	2.34
$(2)^1A_1$		0.88[f]	2.44[f]			0.63	

a: All calculations are performed at CASSCF/6-31G* optimised geometries for unweighted single states in either D_{3h} or C_{2v} symmetry. CASSCF predicts symmetry lowering to planar C_s for $(1)^1E''$, but this is not supported by MRCI or DIP-EOMCC($3h$-$1p$) calculations.
b: Raw DIP-EOMCC($3h$-$1p$)/6-31G data.
c: Extrapolated DIP-EOMCC results to account for $4h$-$2p$ correlations and the effect of replacing the 6-31G basis set by 6-31G* using Eq. (1).
d: CASSCF calculations can break the degeneracy of degeneracy of E' and E'' states owing to asymmetric representation of the active space and orbital optimisation, an effect that is reduced here using state averaging.
e: Two-state calculation using 50:50 weighting.
f: Single-state calculation.
g: transition state on the tricorn Mexican hat, see e.g. Fig. 5.
h: in this case there is a large difference to single-state MRCI calculations which predict the reverse ordering: $(1)^1A_1$ at 0.03 eV, $(1)^1B_2$ at 0.33 eV.

focus on our highest-accuracy DIP-EOMCC data, comparing them with MRCI whenever relevant and appropriate.

We begin with the TABLE S9, which examines the convergence of the DIP-EOMCC calculations as the basis set is extended from 6-31G to 6-31G*, the ring size is extended from 1 to 2, and the truncation level in the electron removing operator of the DIP-EOMCC wavefunction ansatz is extended from $3h$-$1p$ to $4h$-$2p$. Although the most desirable DIP-EOMCC/6-31G* calculations for the 51-atom 2-ring system turned out to be prohibitively expensive, it is clear from TABLE S9 that the convergence of the DIP-EOMCC vertical and adiabatic excitation energies with respect to the wavefunction truncation level and basis set is

very fast. It is, therefore, appropriate to extrapolate the desired DIP-EOMCC(4*h*-2*p*)/6-31G* information for the 2-ring system by adopting the formula:

$$E^{(2\text{-ring})}_{\text{DIP-EOMCC}(4h\text{-}2p)/6\text{-}31G^*} \approx E^{(2\text{-ring})}_{\text{DIP-EOMCC}(3h\text{-}1p)/6\text{-}31G} + [E^{(1\text{-ring})}_{\text{DIP-EOMCC}(4h\text{-}2p)/6\text{-}31G^*} - E^{(1\text{-ring})}_{\text{DIP-EOMCC}(3h\text{-}1p)/6\text{-}31G}]. \quad (1)$$

In this formula, we use the difference between the DIP-EOMCC(4*h*-2*p*)/6-31G* and DIP-EOMCC(3*h*-1*p*)/6-31G energies determined for the smaller 1-ring model to correct the DIP-EOMCC(3*h*-1*p*)/6-31G data obtained for the target 2-ring system for the effects of high-order 4*h*-2*p* correlations, as well as for replacing the 6-31G basis set by its larger 6-31G* counterpart. The resulting DIP-EOMCC-based modelling procedure, as defined by Eq. (1), along with the underlying DIP-EOMCC(3*h*-1*p*)/6-31G approach, are regarded in this study as the major working methods, especially in characterizing the highly complex manifold of singlet electronic states (see Table IV, TABLE S9 - TABLE S11, and FIG. S2). Based on the results compiled in TABLE S9, the mean and maximum unsigned errors characterizing the raw DIP-EOMCC(3*h*-1*p*)/6-31G and extrapolated DIP-EOMCC(4*h*-2*p*)/6-31G* vertical and adiabatic excitation energies, estimated by comparing the DIP-EOMCC(3*h*-1*p*)/6-31G and DIP-EOMCC(4*h*-2*p*)/6-31G* data for the 1-ring model, are 0.07 and 0.17 eV, respectively. Naturally, relative errors characterizing energy differences that correspond to different structures on the same potential energy surface (*e.g.*, barriers separating minima on the same potential) are expected to be even smaller.

Our best DIP-EOMCC-based estimates of the properties of the singlet states summarised in Table IV and TABLE S11, relying on the extrapolated DIP-EOMCC(4*h*-2*p*)/6-31G* energetics. These indicate that the lowest-energy $(1)^1E'$ singlet, which is located 0.75 eV above the triplet ground state at the $(1)^3A_2'$ minimum, undergoes a strong Jahn-Teller distortion resulting in the C_{2v}-symmetric $(1)^1B_2$ minima that lie 0.56 eV above the $(1)^3A_2'$ minimum. These $(1)^1B_2$ minima are interconnected by the C_{2v}-symmetric $(1)^1A_1$ transition states, which are located 0.68 eV above the $(1)^3A_2'$ minimum. In other words, according to the extrapolated DIP-EOMCC(4*h*-2*p*)/6-31G* data, the $(1)^1B_2$ minima resulting from the Jahn-Teller distortion of the $(1)^1E'$ state are 0.12 eV below the $(1)^1A_1$ transition states that connect them. The underlying DIP-EOMCC(3*h*-1*p*)/6-31G calculations for the 2-ring system place the same $(1)^1B_2$ minima 0.07 eV below the interconnecting $(1)^1A_1$ transition states, in good agreement with the extrapolated DIP-EOMCC(4*h*-2*p*)/6-31G* energetics, confirming our earlier remarks about the reasonably fast convergence of the DIP-EOMCC hierarchy.

In summary, the topology of the potential energy surfaces around the Jahn-Teller conical intersection corresponding to the doubly degenerate $(1)^1E'$ singlet, which distorts into the $(1)^1B_2$ minima separated by the $(1)^1A_1$ transition states about 0.1 eV above them, resulting from the DIP-EOMCC(3*h*-1*p*)/6-31G calculations, can be seen in Fig. 5 and FIG. S2. Of note, the prediction that the lowest single state component lies 0.56 eV above the $(1)^3A_2'$ triplet provides a robust prediction of a triplet ground state for V_B^-, confirming previous predictions [12, 17]. This conclusion is further supported by our MRCI/6-31G* calculations, which place the $(1)^3A_2'$ triplet ground-state at 0.36 eV below the lowest singlet, but note that single-state MRCI calculations reduce this value. Also, QM/MM corrections for larger ring sizes act only to increase the perceived instability of the singlet states (Table IV).

As shown in Table 5 and FIG. S2, the next two singlet states above $(1)^1E'$, *i.e.*, $(1)^1E''$ and $(1)^1A_1''$, are predicted to be nearly degenerate at the D_{3h} geometry of the $(1)^3A_2'$ ground state, with the latter one undergoing a large distortion to $(1)^1A_2$ upon geometrical relaxation.

A broad diabatic-based picture of all of the singlet states and how they cross each is provided in TABLE S11 and FIG. S2. In particular, TABLE S11 compiles the vertical and

adiabatic energy differences between all the singlet states, as well as the reorganisation energies associated with conceivable absorption and emission processes, obtained in the DIP-EOMCC/6-31G calculations for the 2-ring system. The extrapolated DIP-EOMCC(4*h*-2*p*)/6-31G* adiabatic transition energies using Eq. (1), which can be found in TABLE S11 and in simpler form in Table IV, indicate that emission from the $(1)^1E''$ component minimum $(2)^1A_2$ to the $(1)^1B_2$ lower well on the $(1)^1E'$ Jahn-Teller surface would be at an energy ΔE_0 = 1.35 eV, which is consistent with the value of 1.18 eV predicted by MRCI/6-31G*. These energies are increased slightly by considering the QM/MM correction for larger ring sizes, but nevertheless the DIP-EOMCC value remains 0.2 eV below the observed photoemission energy. This difference is small enough to warrant further consideration as the source of photoemission from V_B^-. Indeed, the most significant feature of the calculations is that the predicted reorganisation energy for $(2)^1A_2 \rightarrow (1)^1B_2$ is 0.10 eV, an extremely low value that approaches the observed value of < 0.05 eV based on Huang-Rhys spectral fitting.

Methods such as DIP-EOMCC may be included in the QM part of QM/MM calculations, allowing the MM aspect to treat the effect of nuclear distortion whilst 2-ring, or even 1-ring, QM calculations could be performed to understand the key electronic properties. Complete calculations of this type are not performed herein, but instead an indication of likely effects is obtained by the calculation of one of its energy components, the h-BN external strain energy needed to make the optimised 2-ring structures used in the DIP-EOMCC calculations. This is done using a 5-ring MM model, with the outer 3 rings relaxed about frozen inner-ring structures using Gaussian-16. The corrections generated for the adiabatic transition energies are listed in TABLE S11, as well as those after correction. Energies are pushed up to 0.3 – 0.6 eV, a feature attributed to the larger change in the structures predicted for the singlet states than of interest compared to the triplet ground state, but still remain within range of the excitation energy used in the experiments. For example, the critical adiabatic transition energy for $(2)^1A_2 \rightarrow (1)^1B_2$ increases for 1.35 eV to 1.44 eV, much nearer the observed value of ~ 1.6 eV. Full QM/MM optimisation should reduce the magnitude of the effects reported, however.

A feature of the calculations that reduces the likelihood of the observed photoluminescence arising from $(2)^1A_2 \rightarrow (1)^1B_2$ emission is that the lowest-energy singlet excited state is predicted by DIP-EOMCC to be $(1)^1A_2$, not $(2)^1A_2$. Hence the operative photochemical processes would need to facilitate $(1)^1A_2$ being stable for long enough to generate photoemission before internal conversion occurs to the lower-energy state.

S8. HUANG-RHYS AND JAHN-TELLER SPECTRAL SIMULATIONS

A. Ring-size dependence of Huang-Rhys-type simulations of triplet emission

The Huang-Rhys model assumes that the initial and final states can be represented using harmonic Born-Oppenheimer potential-energy surfaces, with all intensity arising within the Franck-Condon approximation, ignoring vibrational frequency changes between the initial and final states and all effects of the Duschinsky rotation matrix. We simulate similar spectra, except that the average frequency change is included, a small effect. The primary quantities required in the simulation are the vibrational displacements δ_i in final-state vibrational mode i, expressed as dimensionless quantities in terms of the zero-point vibrational length. Related quantities are the Huang-Rhys factors $S_i = \delta_i^2/2$ and the mode reorganisation energy $\lambda_i = h\nu_i\delta_i^2/2$. These we determine from normal-mode analyses, using curvilinear coordinates for 1 – 5 ring models to minimise the effects of anharmonicity associated with large-amplitude bending and torsional motions of the defect centre. For this defect, such effects are small, however, and do diminish with increasing ring size, so traditional rectilinear coordinates are used with all QM/MM analyses. Also, full summations over individual lines are used for the pure QM calculations, but this is approximated by a spectral density representation for the QM/MM calculations. Full details, including the (mostly ignored) Duschinsky matrices for the QM calculations are given in Supporting Data. This includes the ground-state normal modes and vibration frequencies for the 1-ring, 2-ring, 3-ring, 4-ring, and 5-ring model compounds, all triplet excited-state normal modes and displacements for the 2-ring compound, and some excited-state data for the 3-ring compound.

TABLE S12 shows results for all a_1' and e' modes of the 2-ring compound for the two components of the $(1)^3E' \rightarrow (1)^3A_2'$ emission, labelled conventionally; there is no displacement in any mode of alternate symmetry and hence no contribution to spectral broadening within the Huang-Rhys model. The table includes results for both the Jahn-Teller minima $(1)^3A_2$ and transition state $(1)^3B_1$, even though only data for the minima are actually utilised in Huang-Rhys simulations. A wide variety of modes are predicted to be spectroscopically active.

As a function of ring size, FIG. S3 - FIG. S7 show the three most important modes (i.e., those with largest reorganization energy) for 1 - 5 ring compounds, respectively. Vibrations are not localized to the defect centre, but instead depict phonons delocalised throughout the model compounds. The most important modes of both a_1' and e' symmetry for compounds in this size range are predicted to be the ones of lowest frequency. This is traced in TABLE S13 where the frequencies of the most important modes of each ring size are listed. Note, however, that as ring-size increases so does the number of modes that are important, making this analysis less meaningful. A significant feature nevertheless is that increasing the ring size results in a significant decrease in the frequency of the lowest a_1' and e', and as these are strongly coupled, this effect will perturb calculated spectra. Nevertheless, the splitting of the dominant mode into multiple components with increasing ring size (e.g, $17a_1'$ splits into two active modes at 161 cm^{-1} and 389 cm^{-1} in the 5-ring compound) negates this effect on low-resolution spectra. Fig. S8 shows the variation in the total ground-state vibrational density of states, as well as Huang-Rhys spectral density $S(\nu)$ (with the total Huang-Rhys factor given by $S = \int_0^\infty S(\nu)d\nu$ and reorganisation energy $\lambda^E = \int_0^\infty S(\nu)\nu d\nu$, showing that this pattern continues to large ring sizes, with the properties of the low-frequency acoustic phonons converging slowly. TABLE S13 show that there is no analogous systematic splitting of the critical vibration frequencies for high-frequency modes excited by the transition.

TABLE S12. Projections of the 2-ring CAM-B3LYP/6-31G* displacements for the $(1)^3A_2$ and $(1)^3B_1$ components of the $(1)^3E''$ state onto the normal vibrational modes of the $(1)^3A_2'$ ground state.

mode	$h\nu_i$		$(1)^3A_2$			$(1)^3B_1$		
	cm^{-1}	eV	δ_i	S_i	λ_i^E	δ_i	S_i	λ_i^E
$17a_1'$	285	0.035	-0.76	0.289	0.010	-1.147	0.658	0.023
$16a_1'$	403	0.050	0.307	0.047	0.002	0.468	0.110	0.005
$15a_1'$	525	0.065	0.121	0.007	0.000	0.124	0.008	0.001
$14a_1'$	623	0.077	0.345	0.060	0.005	0.157	0.012	0.001
$13a_1'$	706	0.088	-0.432	0.093	0.008	-0.333	0.055	0.005
$12a_1'$	913	0.113	-0.013	0.000	0.000	-0.083	0.003	0.000
$11a_1'$	1064	0.132	-0.367	0.067	0.009	-0.339	0.057	0.008
$10a_1'$	1121	0.139	0.362	0.066	0.009	0.276	0.038	0.005
$9a_1'$	1191	0.148	0.067	0.002	0.000	0.066	0.002	0.000
$8a_1'$	1280	0.159	0.035	0.001	0.000	-0.032	0.001	0.000
$7a_1'$	1390	0.172	0.174	0.015	0.003	0.221	0.024	0.004
$6a_1'$	1401	0.174	-0.279	0.039	0.007	-0.283	0.040	0.007
$5a_1'$	1441	0.179	0.17	0.014	0.003	0.158	0.012	0.002
$4a_1'$	1563	0.194	-0.07	0.002	0.000	-0.087	0.004	0.001
$34e'$	183	0.023	3.435	5.900	0.134	-1.842	1.696	0.038
$33e'$	264	0.033	-0.492	0.121	0.004	0.324	0.052	0.002
$32e'$	396	0.049	-0.378	0.071	0.004	0.198	0.020	0.001
$31e'$	469	0.058	-0.272	0.037	0.002	0.255	0.033	0.002
$30e'$	479	0.059	0.407	0.083	0.005	-0.089	0.004	0.000
$29e'$	532	0.066	0.119	0.007	0.000	-0.106	0.006	0.000
$28e'$	630	0.078	0.617	0.190	0.015	-0.312	0.049	0.004
$27e'$	679	0.084	0.235	0.028	0.002	-0.142	0.010	0.001
$26e'$	731	0.091	-0.021	0.000	0.000	-0.005	0.000	0.000
$25e'$	814	0.101	0.453	0.103	0.010	-0.261	0.034	0.003
$24e'$	967	0.120	-0.356	0.063	0.008	0.12	0.007	0.001
$23e'$	1025	0.127	-0.186	0.017	0.002	0.132	0.009	0.001
$22e'$	1051	0.130	0.081	0.003	0.000	-0.039	0.001	0.000
$21e'$	1112	0.138	-0.104	0.005	0.001	0.046	0.001	0.000
$20e'$	1122	0.139	-0.412	0.085	0.012	0.182	0.017	0.002
$19e'$	1155	0.143	-0.209	0.022	0.003	0.074	0.003	0.000
$18e'$	1189	0.147	-0.155	0.012	0.002	0.071	0.003	0.000
$17e'$	1232	0.153	0.126	0.008	0.001	-0.043	0.001	0.000
$16e'$	1262	0.156	-0.128	0.008	0.001	0.014	0.000	0.000
$15e'$	1282	0.159	-0.141	0.010	0.002	0.038	0.001	0.000
$14e'$	1322	0.164	-0.631	0.199	0.033	0.2	0.020	0.003
$13e'$	1340	0.166	-0.591	0.175	0.029	0.268	0.036	0.006
$12e'$	1359	0.168	0.326	0.053	0.009	-0.163	0.013	0.002
$11e'$	1416	0.176	0.093	0.004	0.001	-0.097	0.005	0.001
$10e'$	1422	0.176	-0.19	0.018	0.003	0.12	0.007	0.001
$9e'$	1509	0.187	-0.071	0.003	0.000	0.044	0.001	0.000
$8e'$	1514	0.188	0.077	0.003	0.001	-0.056	0.002	0.000
$7e'$	1581	0.196	-0.017	0.000	0.000	-0.026	0.000	0.000
a_1' sum				0.703	0.057		1.025	0.063
e' sum				7.229	0.284		2.029	0.071
total				7.932	0.340		3.054	0.134

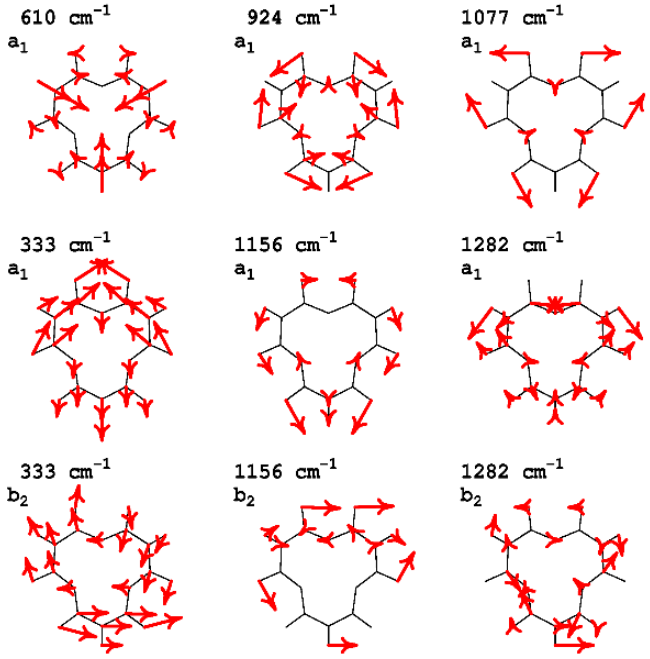

FIG. S3. Some key normal vibrational modes for $(1)^3A_2'$ state of the 1-ring model, calculated CAM-B3LYP/6-31G*, labelled in C_{2v} symmetry. The top row shows a_1' modes whilst the middle and bottom rows show the two components of some e' modes.

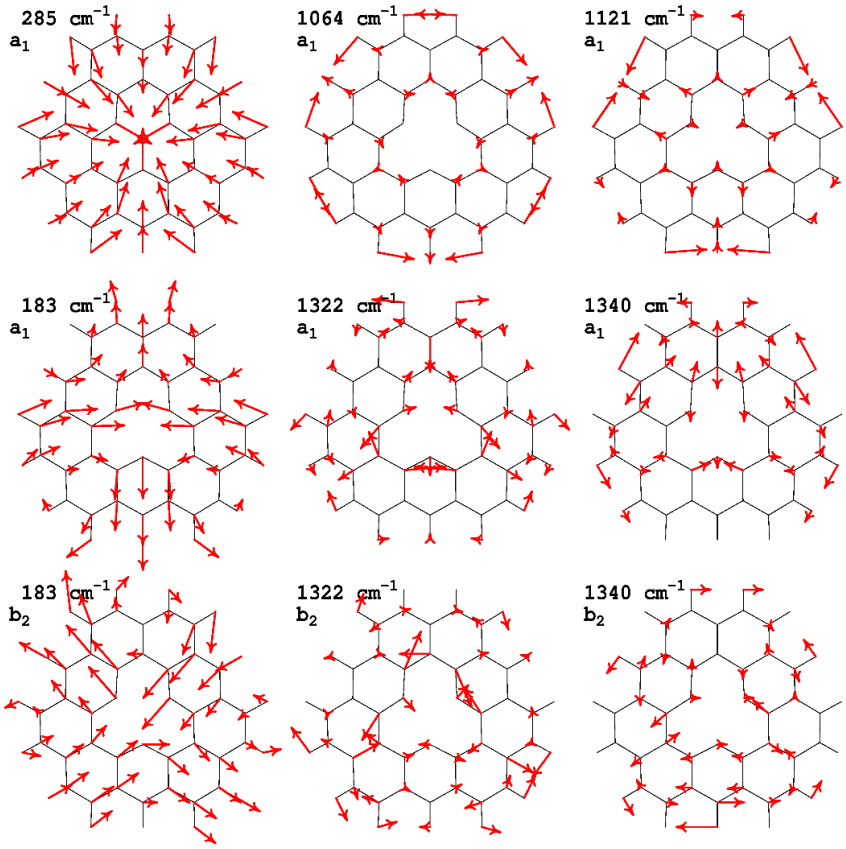

FIG. S4. Some key normal vibrational modes for $(1)^3A_2'$ state of the 2-ring model, calculated CAM-B3LYP/6-31G*, labelled in C_{2v} symmetry. The top row shows modes $17a_1'$, $11a_1'$, and $10a_1'$ whilst the middle and bottom rows show the two components of the $34e'$, $14e'$, and $13e'$ modes.

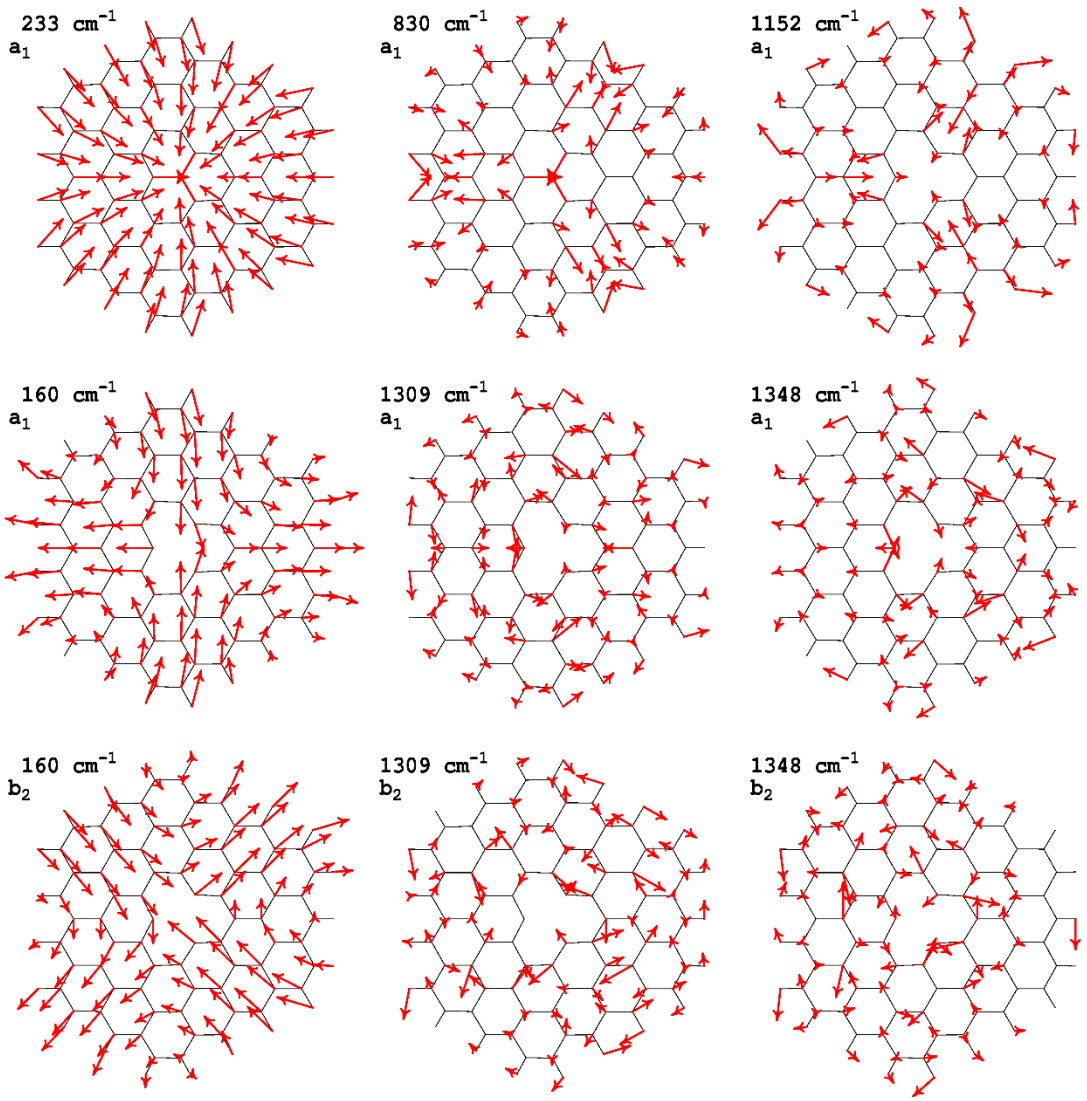

FIG. S5. Some key normal vibrational modes for $(1)^3A_2'$ state of the 3-ring model, calculated CAM-B3LYP/6-31G*, labelled in C_{2v} symmetry. The top row shows a_1' modes whilst the middle and bottom rows show the two components of some e' modes.

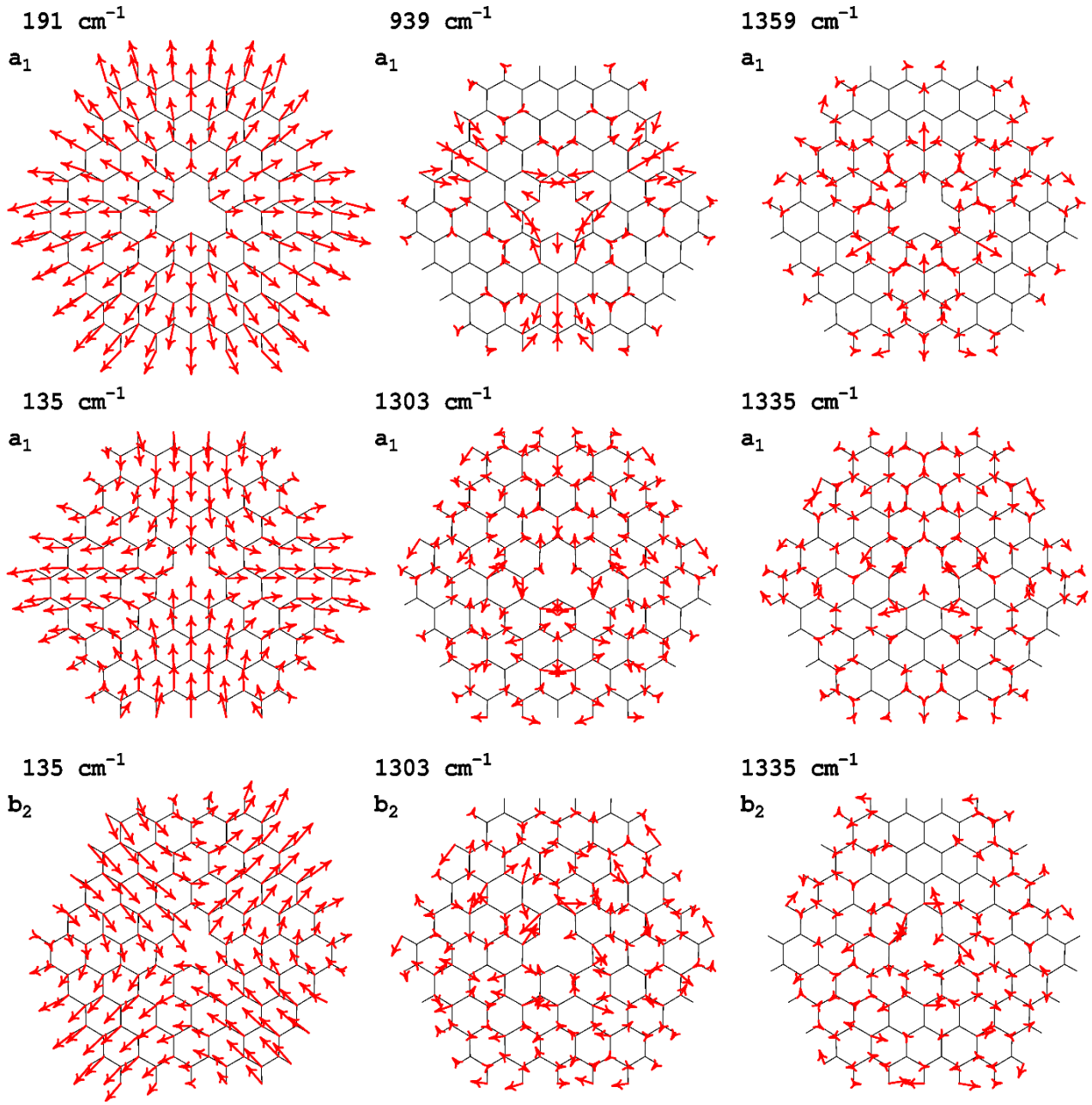

FIG. S6. Some key normal vibrational modes for $(1)^3A_2'$ state of the 4-ring model, calculated CAM-B3LYP/6-31G*, labelled in C_{2v} symmetry. The top row shows a_1' modes whilst the middle and bottom rows show the two components of some e' modes.

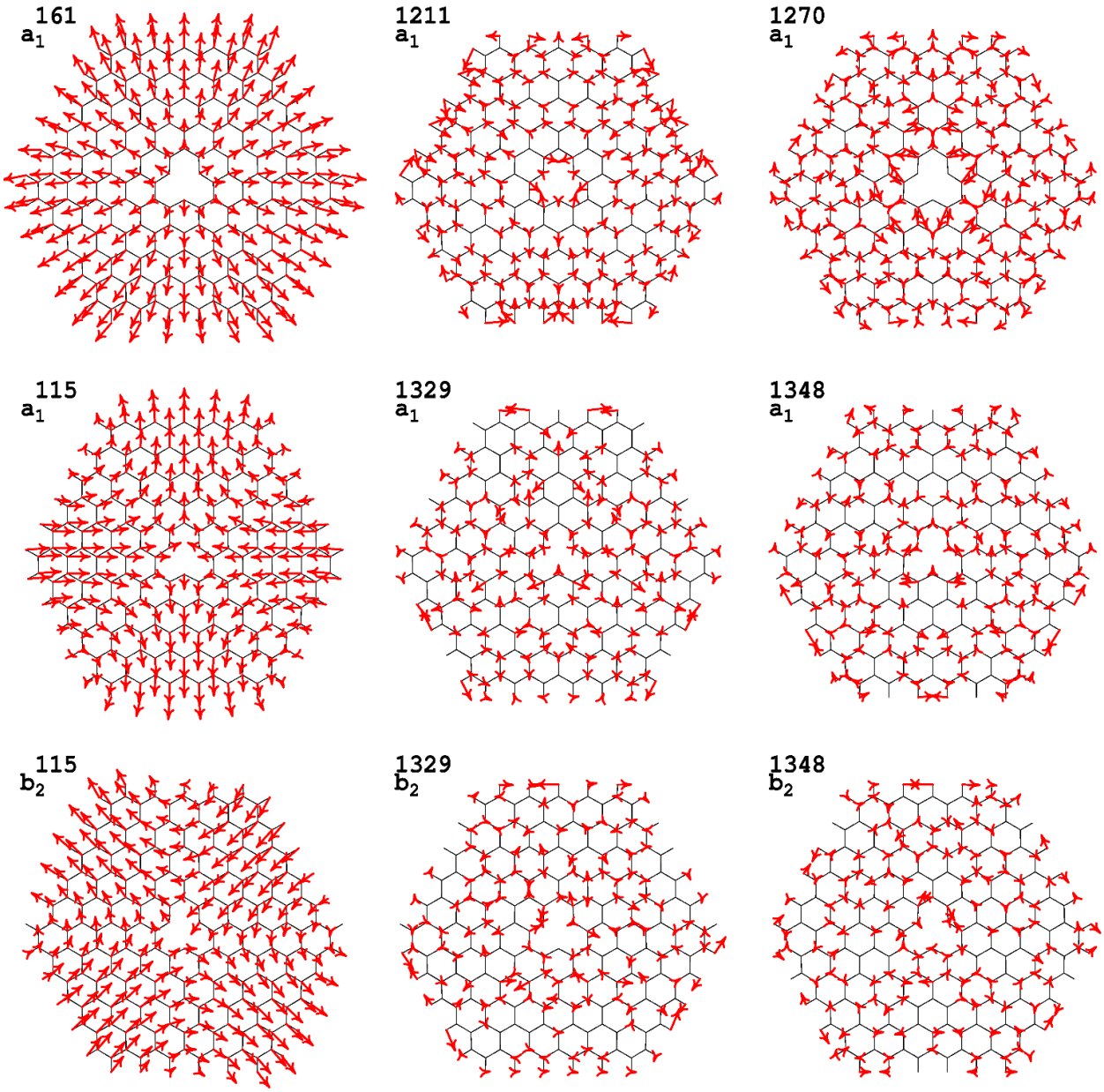

FIG. S7. Some key normal vibrational modes for $(1)^3A_2'$ state of the 5-ring model, calculated CAM-B3LYP/6-31G*, labelled in C_{2v} symmetry. The top row shows a_1' modes whilst the middle and bottom rows show the two components of some e' modes.

TABLE S13. The most important vibrational modes excited as a result of the $(1)^3A_2 \rightarrow (1)^3A_2'$ emission, in cm^{-1}, as a function of model size.

2-ring label	1 ring	2 ring	3 ring	4 ring	5 ring
$17a_1'$	610	285	233	191	161, 389
$11a_1'$	924	1064	830	939	1006
$10a_1'$	1077	1121	1152	1359	1211
$34e'$	333	183	160	135, 435	115, 310
$14e'$	1156	1322	1309	1303	1329
$13e'$	1282	1340	1348	1335	1348

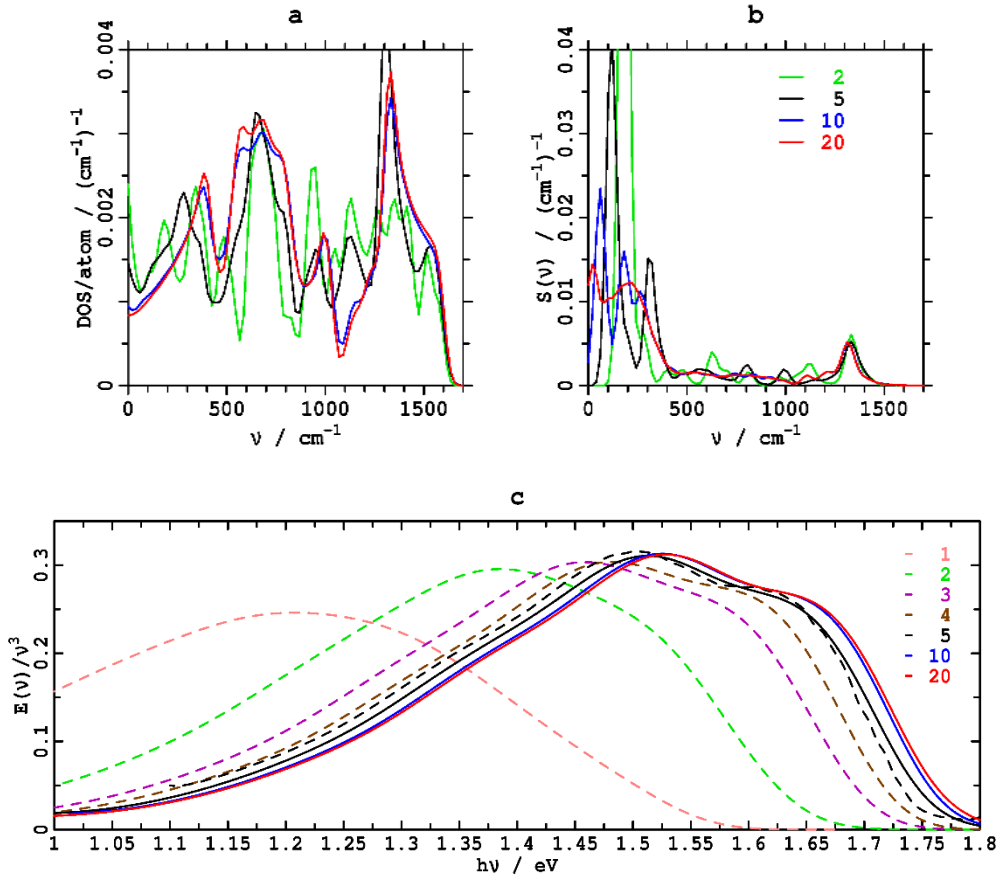

FIG. S8. Convergence of $(1)^3A_2 \rightarrow (1)^3A_2'$ photoemission spectra as a function of ring size from 1 to 20 rings, calculated using Huang-Rhys-type approximations. (a) ground-state density of vibrational states, (b) Huang-Rhys spectral density, (c) calculated emission spectra. Dashed lines: curvilinear analysis with frequency shifts from CAM-B3LYP data; Solid lines- standard rectilinear Huang-Rhys analysis from QM/MM data.

Huang-Rhys simulated $(1)^3A_2 \rightarrow (1)^3A_2'$ photoluminescence spectra at 0 K are shown in FIG. S8c as a function of ring size. The 1-ring model compound yields spectra that are usefully indicative, the 2-ring model gives a realistic bandshape, the 3-ring model is accurate except for a 0.05 eV energy shift, the differences between full QM simulation and QM/MM simulation for the 5-ring model are small, are there appears to be only little change in spectra after 10 rings. Effects on spectra of size expansion appear to be significantly less than those on the spectral density (Fig. S8b) from which they are derived.

B. Hamiltonian model for the Jahn-Teller effect

Simulation of the Jahn-Teller effect is commonly performed by assuming that one vibrational mode of e' symmetry controls all spectroscopic properties, with all other such modes remaining as bystanders. In terms of the Huang-Rhys model often used to interpret spectra involving only non-degenerate electronic states, all modes of e' symmetry do not affect the spectral bandshape. Including only a single e' mode provides an approximation depicting the overall shape of the potential-energy surface. Absorption or emission will always be accompanied by a large displacement in this mode. The major shortcoming of the use of a single-mode model is that Duschinsky rotation will almost certainly have a profound impact on the nature of this mode in the initial and final states, a feature that cannot be included in a 1-mode model. Hence results obtained using this approach are more indicative than quantitative.

The one-e'-mode model, including linear and quadratic coupling, can be expressed in terms of two diabatic electronic-state components named 1 and 2 and displacements Q_a (in symmetric modes a_1) and Q_b (in antisymmetric modes b_2) in each component of the e' mode using the Hamiltonian:

$$H = \begin{bmatrix} H_{11} & H_{12} \\ H_{21} & H_{22} \end{bmatrix}$$

$$H_{11} = h\nu \left[\frac{Q_a^2}{2}(1+\beta) + \frac{Q_b^2}{2}(1-\beta) - \alpha Q_a \right]$$

$$H_{22} = h\nu \left[\frac{Q_a^2}{2}(1-\beta) + \frac{Q_b^2}{2}(1+\beta) + \alpha Q_a \right]$$

$$H_{12} = H_{21} = h\nu[\alpha Q_b + \beta Q_a Q_b]$$

where ν is the vibration frequency of the e' mode, α is its linear vibronic coupling constant, and β the corresponding quadratic coupling. The lower eigenvalue of this matrix, depicting the lower Born-Oppenheimer adiabatic potential-energy surface, is indicated in Fig. 5 as a function of Q_b (b_2 symmetry, horizontal to page) and Q_a (a_1 symmetry, vertical to page); this is depicted quantitatively later in FIG. S11, along with the associated upper adiabatic surface. Taking $Q_a > 0$, the geometry of the stationary point on the + axis ($Q_b = 0$) of the lower surface is:

$$Q_{+a} = \frac{\alpha}{1+\beta} \text{ with energy } E_{+a} = -\frac{h\nu}{2}\frac{\alpha^2}{1+\beta}$$

relative to that of the conical intersection. The other stationary point on the $-Q_a$ axis is:

$$Q_{-a} = \frac{-\alpha}{1-\beta} \text{ with energy } E_{-a} = -\frac{h\nu}{2}\frac{\alpha^2}{1-\beta}.$$

The minimum is at Q_{+a} and the transition state is at Q_{-a} if $\beta < 0$, and vice-versa. The height of the transition state above the minimum is

$$\Delta E^{\ddagger} = \frac{-h\nu\alpha^2\beta}{1-\beta^2}.$$

Relevant quantities that are readily calculable using electronic-structure computational approaches include:

- The energies of the transition state and the conical intersection, by geometry optimisation.
- The vibration frequency ν and the coordinates Q_{+a} and Q_{-a}, by projecting (perhaps using curvilinear coordinates) of the Cartesian displacement vector between the final and initial states onto the normal modes of the final state [88].
- The energy differences between the upper and lower Born-Oppenheimer surfaces at the geometries of the local minima and the transition states.

All tasks are easy to complete for the triplet manifold as 2-ring CAM-B3LYP/6-31G* normal modes are available for the ground state and all excited states. For the singlet manifold, we project calculated displacement vectors onto the normal modes for the triplet ground state. If the vibration frequency is known, then the linear and quadratic coupling parameters can be determined using the above equations from the calculated energies of the conical intersection and transition state at geometries fully optimised in the appropriate point-group symmetry; the data needed to do this is presented in Fig. 5 for all electronic states of interest.

However, this procedure does not guarantee that the geometries are correctly perceived. This is a critical feature as the emission reorganisation energy contribution from the e' modes, ignoring Duschinsky rotation effects, is

$$\lambda^E = \frac{h\nu}{2} Q_{+a}^2$$

and is critical to the prediction of emission spectra that adequately reflect the primary electronic-structure calculations. From the displacements, the diabatic-model coupling parameters can be given by:

$$\beta = \frac{1-x}{1+x}, \qquad \alpha = \frac{2}{1+x} Q_{+a}, \qquad \text{where } x = \frac{-Q_{+a}}{Q_{-a}}$$

and inturn the displacements evaluated from the emission reorganisation energies at the minima and the transition state

$$Q_{+a} = \left(\frac{\lambda_{\text{min}}^{\text{E}}}{2h\nu}\right)^{1/2}, \quad Q_{-a} = \left(\frac{\lambda_{\text{TS}}^{\text{E}}}{2h\nu}\right)^{1/2}.$$

Specifically, for the $(1)^3E'' \rightarrow (1)^3A_2'$ emission, TABLE S12 lists the CAM-B3LYP calculated normal modes of e' and a_1' symmetry for the 2-ring model compound. The totally symmetric modes are used in a Huang-Rhys type scheme to calculate broadening for the each line calculated owing to the Jahn-Teller effect, including the effect of the Duschinsky matrix in determining the average change in vibration frequency for the initial to the final state [11, 88]. The lowest-frequency totally symmetric vibration, $17a_1'$ at 285 cm^{-1}, dominates the displacements that occur within the D_{3h} point group, aided by in-plane torsional and bending modes at 706 and 1064/1121 cm^{-1}, respectively, and then the BN stretch mode $6a_1'$ at 1401 cm^{-1}; all modes delocalise over the sample and are not just restricted to the defect atoms.

We also see that the e' modes that drive the Jahn-Teller distortion are dominated by the lowest frequency mode, $34e'$ at 183 cm^{-1}, which carries half of the reorganisation energy associated with the Jahn-Teller effect. Two other modes, $14e'$ and $13e'$ at 1322 and 1340 cm^{-1}, respectively, are also important and dominate the imaginary mode at the Jahn-Teller transition state. Mostly, the low-frequency mode is all that is required to provide a reasonable description of the displacements, conical intersection and transition-state heights, and the energy splittings between the two Born-Oppenheimer surfaces at the stationary points, etc. Calculated spectra are sensitive to the mode frequency, however, and as the Duschinsky matrix

is being ignored, the most appropriate value for the frequency is desired. Hence the average frequency is determined from the data in TABLE S12 and found to be 300.3 cm^{-1}.

In the Jahn-Teller model, the total emission reorganisation energy is partitioned into contributions from the a_1' modes, that simply generate standard Franck-Condon progressions, and the e' modes, associated with the tricorn Mexican-hat surface. For the 2-ring model, the total of 0.33 eV splits into 0.08 eV from the a_1' modes and 0.25 eV from the e' modes. For the 20-ring model, 0.26 eV becomes analogously split into 0.03 eV and 0.23 eV.

The parameters in the 1-mode Jahn-Teller model are obtained from the 2-ring model by optimizing α and β, but with with constraint that the e' contribution to the emission reorganisation energy is 0.25 eV, constraining the simulations to reproduce this is critical property determining from the emission spectrum. Hence the fit has only one free parameter. Three models are considered, as listed in TABLE S14, in each case setting the vibration frequency to 200 cm^{-1} (dominant single mode), 300 cm^{-1} (average mode) and 500 cm^{-1} (to map the parameter space). The optimisation fits the Jahn-Teller surfaces to calculated energetic properties, as listed in the table. Model #2 utilizing the average frequency fits the data best. This model is also the natural one suggested by the large-ring calculations reported in FIG. S8 as the peak in the optical-phonon band of the spectral density that pertains to the Jahn-Teller effect occurs at this frequency. However, in the Jahn-Teller model that results, the energies of the conical intersection (CI) and transition state (TS) are less than they should be. The associated minimum geometry Q_{+a} = 3.666 is correct by design, but Q_{-a} = -1.952 should be -2.64. Actually, the energy gap between the CI and TS is well reproduced, the poorly reproduced energies are all associated with the avoided crossing of the $(1)^2A_2$ and $(2)^3A_2$ surfaces. It would seem that the best way to improve the spectral simulations is to explicitly include the effect of this crossing rather than to expand the complexity of the Jahn-Teller model. The effects of model variation on calculated emission spectra are shown in FIG. S9 and are significant. As the Jahn-Teller frequency is lowered, the contraction of the emission band towards its centre is enhanced. This effect is also shown in Fig. 2 where the Model #2 Jahn-Teller spectrum is compared to its much broader Huang-Rhys counterpart.

Evaluation of the $(1)^3E'' \rightarrow (1)^3A_2'$ emission assuming just a Huang-Rhys type approximation (Fig. 2) is done using all of the a_1' and e' displacement and frequencies for $(1)^3A_2$ from TABLE S12.

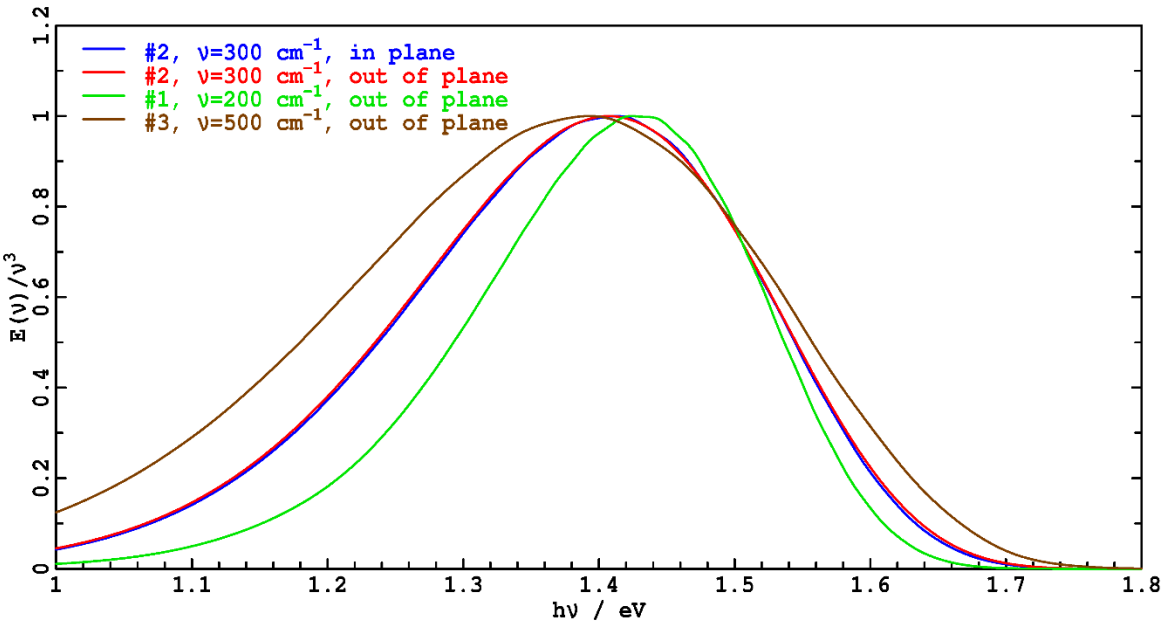

FIG. S9. Comparison of photoluminescence bandshapes for the $(1)^3E'' \rightarrow (1)^3A_2'$ transition evaluated for weak out-of-plane polarised intensity native to the Jahn-Teller distortion for Models #1, #2, and #3, and for the stronger in-plane perpendicular polarised intensity (Model #2 only) induced by b_1 modes (TABLE S15). The out-of-plane Model #2 intensity is also shown in Fig. 2. All spectra share the same adiabatic transition energy E_0 = 1.72 eV and emission reorganisation energy λ^E = 0.33 eV.

TABLE S14. Fitting of the Jahn-Teller model for the $(1)^3E''$ surface.[a]

fit	$h\nu$ / cm^{-1}	α	β	$\lambda^E((1)^3B^1)$ / eV	E_{CI} / eV	E_{TS} / eV	adiabatic energy gap at $(1)^1A_2$ geom. / eV	adiabatic energy gap at $(1)^1B_1$ geom. / eV
CAM-B3LYP				0.13	0.25	0.16	0.90	0.16
#1	200	3.413	-0.240	0.09	0.19	0.07	0.88	0.43
#2	300	2.548	-0.305	0.10	0.17	0.08	0.85	0.33
#3	500	2.102	-0.260	0.09	0.19	0.08	0.87	0.39

a: α and β are constrained to yield the CAM-B3LYP value of $\lambda^E = 0.25$ eV for emission from $(1)^3A_2$, hence there is only one free parameter fitted to five energies at each specified vibration frequency.

C. Transition-moment profile

All spectral simulations require the specification of a transition moment profile. The default one for a Jahn-Teller situation like $(1)^3E'' \rightarrow (1)^3A_2'$ involving a forbidden transition allows for intensification of the transition through the Hertzberg-Teller mechanism as a function of the e' normal mode that induces the geometrical distortion. In this case, the transition-moment operator connecting the initial diabatic state pair used to describe $(1)^3E''$ (rows) interacting with $(1)^3A_2'$ (column) is

$$\mathbf{M} = \frac{dM}{dQ}\begin{bmatrix} Q_a \\ Q_b \end{bmatrix}.$$

where $\frac{dM}{dQ}$ is the rate of change of the transition moment as a function of nuclear displacement away from the conical intersection, assumed to be a constant.

The accuracy of this approximation is considered in FIG. S10 where the transition moment is linearly interpolated along paths leading from the equilibrium structure of $(1)^3B_1$ to $(1)^3A_2'$ to $(1)^3A_2$. Also shown in the figure are the associated energy profiles. Whereas the energy profiles depicts those expected for a tricorn Mexican hat, the transition moment profile becomes non-linear and approaches constant values as the C_{2v} structures are approached, indicative that $(1)^3E''$ strongly interacts with other nearby states(s). Indeed, examination of the wavefunctions indicates in particular an avoided crossing with $(2)^3A_2$. The accuracy of the linear model depicting the transition-moment profile is therefore questionable. The value of the transition moment at the $(1)^3A_2$ geometry is 0.045 au, only one third of that expected from the value of the derivative $\frac{dM}{dQ} = 0.037$ obtained at the conical intersection. Indeed, at the $(1)^3A_2$ geometry, the intensity is nearly evenly shared between $(1)^3A_2$ and $(2)^3A_2$. Nevertheless, the simulated spectra (Fig. 2) embodying the Jahn-Teller effect use the traditional linear model. Alternatively, the spectrum in Fig. 2 calculated using the Huang-Rhys type approach, motivated by FIG. S10, assumes a constant transition moment profile. Explicitly adding the transition moment derivatives to include both Franck-Condon and Herzberg-Teller intensity indeed produces little change to the calculated spectrum, something unintuitive for a system displaying the Jahn-Teller effect.

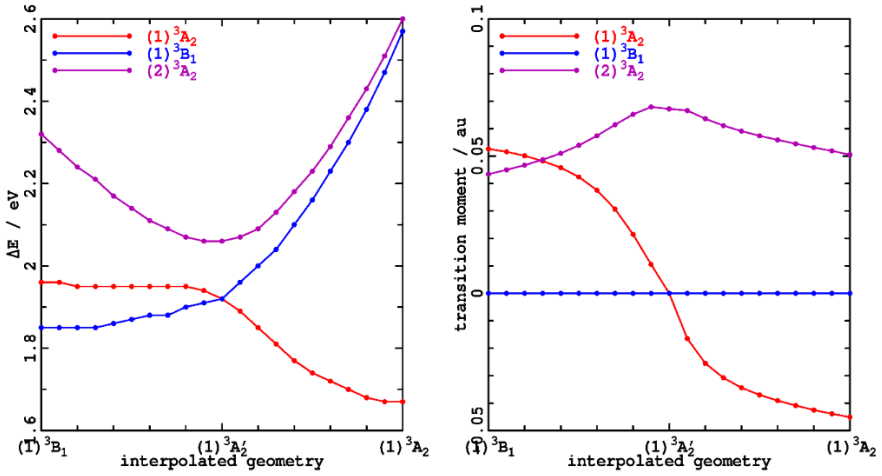

FIG. S10. Energy and transition moment profiles along lines interpolated between the 2-ring CAM-B3LYP optimised geometries of $(1)^3B_1$, $(1)^3E''$, and then $(1)^3A_2$.

D. The $(1)^3E'' \rightarrow (1)^3A_2'$ transition

We briefly consider the Jahn-Teller effect on the $(1)^3E''$ state and the $(1)^3E'' \rightarrow (1)^3A_2'$ transition in FIG. S11. This shows as a function of displacements Q_a and Q_b the utilised Born-Oppenheimer surface for $(1)^3A_2'$, the lower and upper surfaces for $(1)^3E''$, and the transition-moment profile assuming the linear model. Of note, the lower and upper components of $(1)^3E''$ manifest a derivative discontinuity at the conical intersection, whilst the transition moment displays a phase jump of π along a line (Berry phase). To avoid these problems, the Born-Oppenheimer approximation is not used in this analysis, with all spectra determined directly by solving the full electron-vibration Hamiltonian **H** in the basis of the coupled diabatic states.

E. In-plane polarised intensity through the Herzberg-Teller mechanism

For the $(1)^3E'' \rightarrow (1)^3A_2'$ transition, intensity can be borrowed from the nearby intense $(1)^3E' \rightarrow (1)^3A_2'$ transition, through vibronic coupling in out-of-plane modes of e' symmetry. This would facilitate dipole-allowed emission polarised within the plane of the h-BN, adding to the out-of-plane polarised emission intrinsically associated with the Jahn-Teller distortion. To model this, we displace the $(1)^3A_2$ state using the ground-state out-of-plane normal modes, evaluating the derivatives of the calculated in-plane intensity with respect to these displacements. The results are given in TABLE S15. Borrowed intensity polarised parallel to the C_{2v} axis of one of the $(1)^3A_2$ wells gains 0.3 times the intensity of the native out-of-plane polarisation, whilst borrowed intensity polarised perpendicular to that axis is 7.0 times stronger. Averaging over all three $(1)^3A_2$ wells will equally distribute the intensity within the h-BN plane.

The spectral bandshapes associated with native out-of-plane intensity and borrowed in-plane intensity are naively expected to be quite different as the out-of-plane intensity demands that the change in quanta in mode Q_a be odd whereas this change must be even for the in-plane polarisation. Also, each vibrational mode listed in TABLE S15 produces a false origin upon which the Huang-Rhys and other spectral progressions are based, each mimicking a ZPL in terms of its effect on spectral intensity. Net spectral broadening involves the summation of the effects in each mode, representable as an effective reorganisation energy listed in the table, which will differ from the analogous quantity demanded by odd-quanta excitation in Q_a in the Jahn-Teller case. The calculated Jahn-Teller spectral profiles for the native out-of-plane emission and the intense perpendicular-polarised emission are compared in FIG. S12. The calculated oscillator strengths for each band and polarisation are listed in TABLE S16.

The $(1)^3A_1'' \rightarrow (1)^3A_2'$ transition can be intensified by similar means. Analogous calculations, predict a negligible effect, however.

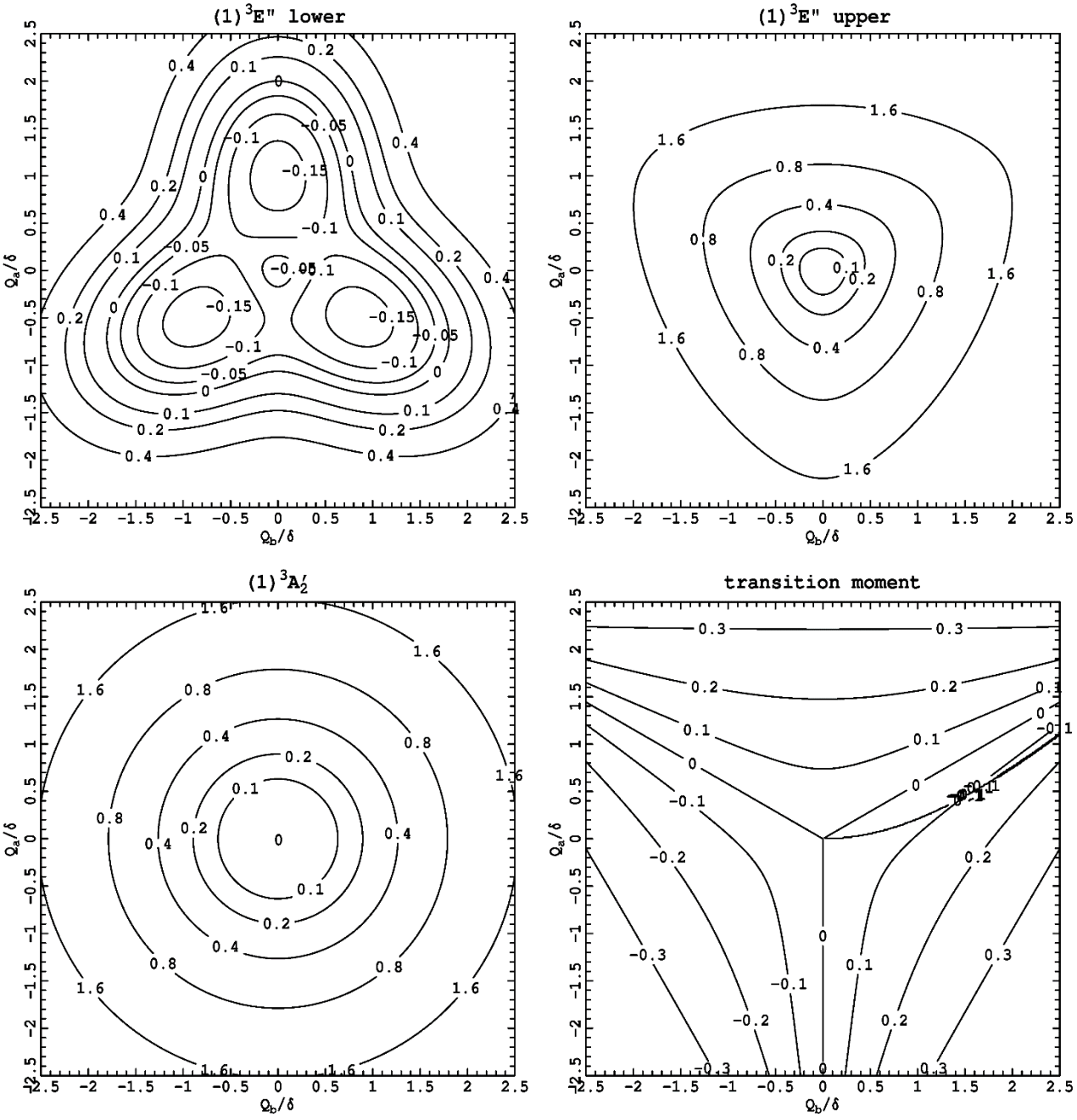

FIG. S11. Born-Oppenheimer potential energy surfaces (in eV relative to the conical intersection) and transition moment profile (in a.u.) pertaining to the $(1)^3E'' \rightarrow (1)^3A_2'$ transition, from fits to 2-ring CAM-B3LYP/6-31G* data. Nuclear displacement are shown relative to that at the $(1)^3A_2$ minima of $\delta = 3.666$. The lower and upper surfaces of $(1)^3E''$ display derivative discontinuities at the conical intersection whilst the transition moment profile manifests a line along which the phase jumps by π (Berry phase). Note that the height of the transition state in the $(1)^3E''$ from the model potential is 0.08 eV, less than the CAM-B3LYP calculated value of 0.16 eV, with key energy differences between the lower and upper surfaces also by varying by up to 0.2 eV. The lower surface for $(1)^3E''$ is also shown in Fig. 2. Born-Oppenheimer surfaces are not used in the Jahn-Teller spectral simulations.

TABLE S15. Herzberg-Teller transition-moment derivatives dM/dQ for the $(1)^3A_2$ state, in a.u., polarised in-plane and either parallel or perpendicular to the C_{2v} axis. For emission at 0 K, the total borrowed intensity is listed relative to that for the Jahn-Teller allowed out-of-plane intensity, as well as the effective reorganisation energy associated with the nuclear motion.

a_2 modes, polarised parallel			b_1 modes, polarised perpendicular		
$h\nu$ / cm^{-1}	$h\nu$ / eV	dM/dQ	$h\nu$ / cm^{-1}	$h\nu$ / eV	dM/dQ
36	0.004	-0.0024	221	0.027	0.0202
82	0.010	-0.001	682	0.085	-0.0188
108	0.013	-0.0048	173	0.021	0.0141
148	0.018	-0.0033	757	0.094	0.0129
173	0.021	-0.003	655	0.081	0.011
208	0.026	-0.0017	618	0.077	-0.0098
231	0.029	-0.0014	108	0.013	0.0088
327	0.041	0.0012	36	0.004	-0.0086
333	0.041	0.0011	748	0.093	-0.0086
337	0.042	-0.0009	52	0.006	0.0078
371	0.046	-0.0044	337	0.042	0.0062
610	0.076	0.0004	208	0.026	-0.006
618	0.077	0.0004	643	0.080	0.0055
643	0.080	-0.0011	148	0.018	-0.0045
668	0.083	0.0001	327	0.041	-0.0034
682	0.085	0.0001	909	0.113	-0.0019
699	0.087	-0.0001	306	0.038	0.0017
748	0.093	0.0019	380	0.047	-0.0015
909	0.113	-0.0001	699	0.087	-0.0014
936	0.116	-0.0001	910	0.113	-0.0012
937	0.116	0.0003	699	0.087	0.0007
955	0.118	-0.0001	371	0.046	-0.0005
			937	0.116	0.0003
			957	0.119	-0.0002
			955	0.118	0
relative intensity		0.3			7.0
effective λ^E (eV)		0.03			0.05

TABLE S16. Summary of 2-ring CAM-B3LYP/6-31G* (triplet) and EOM-CC/CASSCF(10,6)/6-31G* (singlet) calculated absorption and emission oscillator strengths and radiative lifetimes, including both Franck-Condon and Herzberg-Teller contributions, for different electric-dipole polarisation directions, for transitions of the V_B^- defect of h-BN.

transition	polarisation	mechanism	f_{osc}	Emission lifetime / μs
$(1)^3E'' \leftarrow (1)^3A_2'$	normal	Franck-Condon	0	-
	normal	Herzberg-Teller	0.00010	-
	in-plane	Herzberg-Teller	~ 0.0007[b]	-
$(1)^3A_1'' \leftarrow (1)^3A_2'$	normal[a]	Franck-Condon	0.00023	-
$(1)^3E' \leftarrow (1)^3A_2'$	in-plane	Franck-Condon	0.39	-
$(1)^3E'' \rightarrow (1)^3A_2'$	normal	Herzberg-Teller	0.00007	172
	in-plane	Herzberg-Teller	0.00049	24
$(1)^1E'' \rightarrow (1)^1E'$	normal	Herzberg-Teller	0.00059	25
	in-plane	Herzberg-Teller	~ 0.004[b]	~4[b]

a: other components not evaluated.
b: estimate using calculated factor for triplet emission for analogous states.

F. Simulated absorption spectra

The calculations also permit the evaluation of absorption spectra. To date, there is no experimental data to which this can be compared. Spectra are calculated for the $(1)^3E'' \leftarrow (1)^3A_2'$ absorption using the same Jahn-Teller surface as used in the calculations of emission. For the $(1)^3A_1'' \leftarrow (1)^3A_2'$ absorption, symmetry lowering to C_{2v} occurs, but the way in which such lowering remains compatible with the global 3-fold defect symmetry has not been investigated. Hence a Huang-Rhys type model is used. For the $(1)^3E' \leftarrow (1)^3A_2'$ absorption, a very large Jahn-Teller distortion occurs, but the transition state in the tricorn surface is very shallow (Fig. 2) and it is clear that other perturbations control details. Hence we again use a Huang-Rhys type model, simulating spectra for both $(1)^3A_1 \leftarrow (1)^3A_2'$ and $(2)^3B_2 \leftarrow (1)^3A_2'$; inclusion of the Jahn-Teller effect is predicted to slightly narrow the absorption about the band centres, akin to the effect seen in Fig. 2 for $(1)^3E' \rightarrow (1)^3A_2'$ photoemission. Calculated spectra are shown in FIG. S12. The data used in these simulations is obtained by projecting the displacement vector depicting the change in geometry upon photoabsorption onto the normal modes of the appropriate excited state. The excited-state frequencies and projections are listed in TABLE S17.

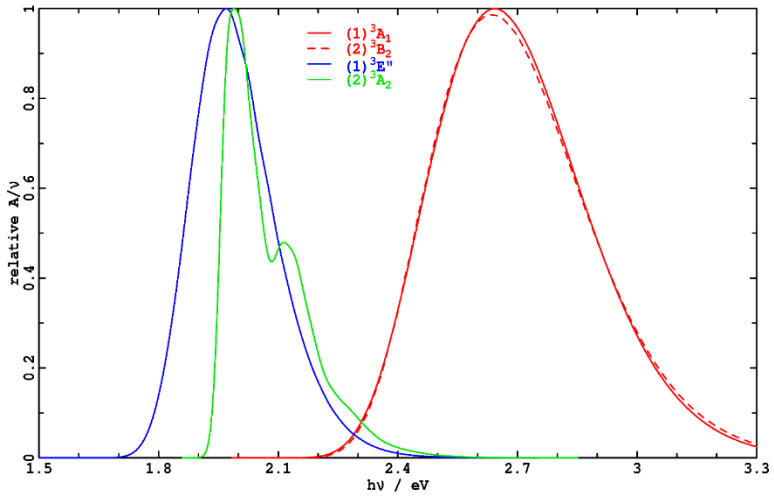

FIG. S12. Calculated absorption band shapes within the triplet manifold; only the $(1)^3E' \leftarrow (1)^3A_2'$ transitions exciting $(1)^3A_1$ and $(2)^3B_2$ is predicted to have significant intensity, see TABLE S16.

TABLE S17. Calculated excited-state vibration frequencies ν_i (in cm^{-1}) and the dimensionless displacement δ_i obtained by projecting the change in geometry upon excitation onto the normal modes of the excited state; the associated vibrational contributions to the reorganisation energy λ_i^A are also listed (in cm^{-1}).

$(1)^3A_2 \leftarrow (1)^3A_2'$			$(1)^3B_1 \leftarrow (1)^3A_2'$			$(2)^3A_2 \leftarrow (1)^3A_2'$			$(1)^3A_1 \leftarrow (1)^3A_2'$			$(2)^3B_2 \leftarrow (1)^3A_2'$		
ν_i	δ_i	λ_i^A	ν_i	δ_i	λ_i^A	ν_i	δ_i	λ_i^A	ν_i	δ_i	λ_i^A	ν_i	δ_i	λ_i^A
192	-3.469	1158	188	-1.835	317	163	0.406	14	192	-3.469	1158	187	-2.273	483
268	0.045	0	259	0.115	2	262	0.291	11	268	0.045	0	269	-0.166	4
294	-1.223	220	295	1.264	236	288	-1.262	230	294	-1.223	220	292	3.425	1713
397	-0.530	56	394	0.380	28	392	0.222	10	397	-0.530	56	392	0.759	113
399	0.328	22	399	0.278	15	399	0.311	19	399	0.328	22	394	-0.309	19
480	-0.484	56	454	-0.492	55	457	-0.146	5	480	-0.484	56	464	-0.365	31
511	-0.226	13	479	0.284	19	486	-0.430	45	511	-0.226	13	513	0.028	0
522	0.096	2	522	-0.131	5	521	0.147	6	522	0.096	2	518	0.093	2
560	-0.427	51	535	0.106	3	541	0.200	11	560	-0.427	51	591	-0.044	1
624	0.297	28	615	0.240	18	611	-0.148	7	624	0.297	28	629	-1.353	575
635	-0.318	32	628	0.035	0	628	0.052	1	635	-0.318	32	656	-0.352	41
678	0.194	13	676	-0.093	3	675	-0.035	0	678	0.194	13	677	0.233	18
710	0.390	54	712	0.299	32	710	-0.315	35	710	0.390	54	711	1.002	357
739	-0.027	0	739	-0.078	2	738	-0.089	3	739	-0.027	0	754	0.343	44
817	0.352	51	793	-0.114	5	790	0.074	2	817	0.352	51	832	0.292	36
905	-0.022	0	906	0.081	3	903	-0.004	0	905	-0.022	0	904	0.235	25
959	-0.312	47	960	0.152	11	961	0.161	13	959	-0.312	47	958	-0.140	9
1016	-0.244	30	1009	0.007	0	1017	0.144	11	1016	-0.244	30	1019	-0.031	1
1046	0.133	9	1046	-0.124	8	1046	-0.065	2	1046	0.133	9	1042	0.088	4
1056	-0.259	35	1055	0.327	56	1053	-0.385	78	1056	-0.259	35	1051	0.160	14
1092	0.448	110	1100	-0.305	51	1092	0.461	116	1092	0.448	110	1093	0.199	22
1114	0.277	43	1109	0.077	3	1107	-0.052	2	1114	0.277	43	1108	0.051	2
1116	-0.249	34	1115	0.005	0	1113	0.033	1	1116	-0.249	34	1113	0.032	1
1146	-0.011	0	1149	0.004	0	1144	-0.309	55	1146	-0.011	0	1148	0.070	3
1182	-0.143	12	1175	0.234	32	1154	0.198	23	1182	-0.143	12	1171	0.039	1
1186	0.121	9	1185	0.158	15	1181	0.161	15	1186	0.121	9	1179	-0.103	6
1218	-0.182	20	1188	-0.229	31	1184	0.088	5	1218	-0.182	20	1222	-0.045	1
1229	-0.075	3	1224	0.056	2	1225	-0.113	8	1229	-0.075	3	1227	0.051	2
1265	-0.199	25	1247	0.125	10	1251	0.057	2	1265	-0.199	25	1241	-0.081	4
1280	0.104	7	1264	0.120	9	1260	0.191	23	1280	0.104	7	1267	-0.081	4
1321	0.158	16	1270	0.051	2	1264	0.039	1	1321	0.158	16	1320	0.149	15
1345	0.308	64	1328	-0.194	25	1323	0.024	0	1345	0.308	64	1345	0.001	0
1363	0.458	143	1345	0.185	23	1345	0.045	1	1363	0.458	143	1372	-0.049	2
1375	0.557	213	1363	0.214	31	1362	0.205	29	1375	0.557	213	1386	0.062	3
1403	-0.193	26	1401	-0.268	50	1399	0.233	38	1403	-0.193	26	1399	0.251	44
1420	0.166	20	1406	-0.103	7	1412	-0.003	0	1420	0.166	20	1414	0.026	1
1438	0.253	46	1417	0.003	0	1418	-0.021	0	1438	0.253	46	1427	-0.056	2
1449	0.038	1	1438	0.142	15	1440	0.129	12	1449	0.038	1	1487	-0.079	5
1505	0.088	6	1488	0.001	0	1480	-0.077	4	1505	0.088	6	1505	-0.004	0
1526	0.166	21	1509	-0.009	0	1510	0.006	0	1526	0.166	21	1546	-0.018	0
1551	-0.111	10	1539	-0.076	4	1539	0.078	5	1551	-0.111	10	1579	-0.220	38
1583	-0.047	2	1550	-0.062	3	1549	-0.083	5	1583	-0.047	2	1688	0.826	575

G. The $(1)^1E'' \rightarrow (1)^1\mathrm{E}'$ transition

Simulation of the emission spectrum within the singlet manifold is complicated by the initial and final states both being doubly degenerate $(1)^1E'' \rightarrow (1)^1E'$, with the Jahn-Teller effect on the initial state being small but its interaction with $(1)^1A_1''$ large, as highlighted in FIG. S2. The global qualitative nature of the surfaces pertaining to the initial state are therefore difficult to reproduce using simple models. Hence the approach taken is to consider that emission only occurs from isolated $(2)^1A_2$ wells. The final state undergoes a strong Jahn-Teller distortion that is readily modelled using the single e' mode approximation. Another difficulty is that the normal modes of vibration are not available for any singlet state. As a result, we project displacement vectors pertaining to differences in 2-ring singlet-state CASSCF(10,6)/6-31G* geometries onto the normal modes of $(1)^3A_2'$. This is a crude approximation, but one that will capture the broad qualitative features of the spectra. The results are given in TABLE S18.

Table IV and TABLE S10 indicate that the geometries of $(2)^1A_2$ and $(1)^1A_1$ are very similar, leading to the very small emission reorganisation energy of 0.03 eV. Nevertheless, $(1)^1A_1$ is predicted to form the transition states on the tricorn Mexican hat surface, with the $(1)^1B_2$ minima lying 0.07 eV deeper so that the total reorganisation energy is 0.10 eV. The normal-mode projections listed in TABLE S18 depict a reorganisation energy to $(1)^1A_1$ of 0.07 eV, made up 0.03 eV from a_1' modes and 0.04 eV from e' modes, which is larger than the expected value of 0.03 eV. TABLE S10, however, indicates a that a large Duschinsky rotation effect contributes to the reorganisation energy as that for the corresponding absorption is 0.17 eV, and hence the value projected onto the $(1)^3A_2'$ modes appears reasonable. To re-establish parameters suitable for simulating the emission spectrum, we neglect altogether the displacements in the Jahn-Teller-active (e') modes and just use the totally symmetric (a_1') ones.

No means is available for determining the vibration frequency responsible for the Jahn-Teller distortion in $(1)^1E'$, but useful choices would appear to be the dominant mode revealed in TABLE S18 at 469 cm^{-1}, and the average mode frequency calculated for $(1)^3E'$, 300 cm^{-1}. The available data for fitting the Jahn-Teller parameters α and β are the heights of the conical intersection and transition state (Fig. 5) and the vertical excitation energies between components (TABLE S10). Two realistic models are presented in TABLE S19, named #1 and #2, with the resulting emission spectra shown in FIG. S13(a). The spectrum for Model #2 is also reproduced in Fig. 2. Both spectra are in accord with the basic shapes observed for V_B^- photoluminescence, predicting much narrower spectra than those simulated for emission within the triplet manifold.

In FIG. S13(b) and (c), the calculated spectrum in FIG. S13(a) for Model #2 is differently represented. First, the spectrum is continued down to zero frequency. The main part of the emission corresponds to the $(2)^1A_2 \rightarrow (1)^1B_2$ is predicted to occur at an energy of 0.43 eV or 2900 nm (TABLE S10). This is a feature well reproduced by the model that was not involved in its fitting (TABLE S19), indicating that the model does indeed provide a robust description of the potential-energy surfaces involved. Hence little emission occurs in the high-energy region associated with $(2)^1A_2 \rightarrow (1)^1A_1$ as this is vibronic intensity only. In FIG. S13(c), the emission is shown at high resolution to indicate that spectra associated with the

TABLE S18. Projections of the 2-ring CAM-B3LYP/6-31G* displacements for the $(1)^3A_2$ and $(1)^3B_1$ components of the $(1)^3E''$ state onto the normal vibrational modes of the $(1)^3A_2'$ ground state, determining the reorganisation energies in each mode.

mode	$h\nu_i$		$(1)^3A_2$		
	cm^{-1}	eV	δ_i	S_i	λ_i^E
$17a_1'$	285	0.035	-0.373	0.070	0.002
$16a_1'$	403	0.050	0.051	0.001	0.000
$15a_1'$	525	0.065	0.096	0.005	0.000
$14a_1'$	623	0.077	0.334	0.056	0.004
$13a_1'$	706	0.088	-0.388	0.075	0.007
$12a_1'$	913	0.113	0.076	0.003	0.000
$11a_1'$	1064	0.132	-0.219	0.024	0.003
$10a_1'$	1121	0.139	0.315	0.050	0.007
$9a_1'$	1191	0.148	0.070	0.002	0.000
$8a_1'$	1280	0.159	0.090	0.004	0.001
$7a_1'$	1390	0.172	0.004	0.000	0.000
$6a_1'$	1401	0.174	-0.180	0.016	0.003
$5a_1'$	1441	0.179	0.152	0.012	0.002
$4a_1'$	1563	0.194	-0.002	0.000	0.000
$34e'$	183	0.023	-0.180	0.0162	0.000
$33e'$	264	0.033	0.350	0.0613	0.002
$32e'$	396	0.049	-0.054	0.0015	0.000
$31e'$	469	0.058	0.535	0.1431	0.008
$30e'$	479	0.059	-0.085	0.0036	0.000
$29e'$	532	0.066	-0.223	0.0249	0.002
$28e'$	630	0.078	-0.281	0.0395	0.003
$27e'$	679	0.084	-0.083	0.0034	0.000
$26e'$	731	0.091	-0.154	0.0119	0.001
$25e'$	814	0.101	-0.191	0.0182	0.002
$24e'$	967	0.120	0.116	0.0067	0.001
$23e'$	1025	0.127	0.083	0.0034	0.000
$22e'$	1051	0.130	-0.032	0.0005	0.000
$21e'$	1112	0.138	0.031	0.0005	0.000
$20e'$	1122	0.139	0.231	0.0267	0.004
$19e'$	1155	0.143	0.047	0.0011	0.000
$18e'$	1189	0.147	0.076	0.0029	0.000
$17e'$	1232	0.153	-0.105	0.0055	0.001
$16e'$	1262	0.156	0.017	0.0001	0.000
$15e'$	1282	0.159	0.089	0.0040	0.001
$14e'$	1322	0.164	0.301	0.0453	0.007
$13e'$	1340	0.166	0.238	0.0283	0.005
$12e'$	1359	0.168	-0.132	0.0087	0.001
$11e'$	1416	0.176	-0.065	0.0021	0.000
$10e'$	1422	0.176	0.090	0.0041	0.001
$9e'$	1509	0.187	0.035	0.0006	0.000
$8e'$	1514	0.188	-0.051	0.0013	0.000
$7e'$	1581	0.196	-0.026	0.0003	0.000
a_1' sum				0.32	0.030
e' sum				0.47	0.041
total				0.79	0.071

TABLE S19. Fitting Jahn-Teller parameters to the DIP-EOMCC data for the $(1)^1E'$ surface.

fit	$h\nu$ / cm^{-1}	α	β	E_{CI} / eV	E_{TS} / eV	adiabatic energy gap at $(1)^1B_2$ geom. / eV	adiabatic energy gap at $(1)^1A$ geom. / eV
DIP-EOMCC				0.20	0.07	1.16	0.99
#1	469	3.163	-0.115	0.33	0.07	1.38	0.99
#2	300	3.588	-0.138	0.28	0.07	1.18	0.79

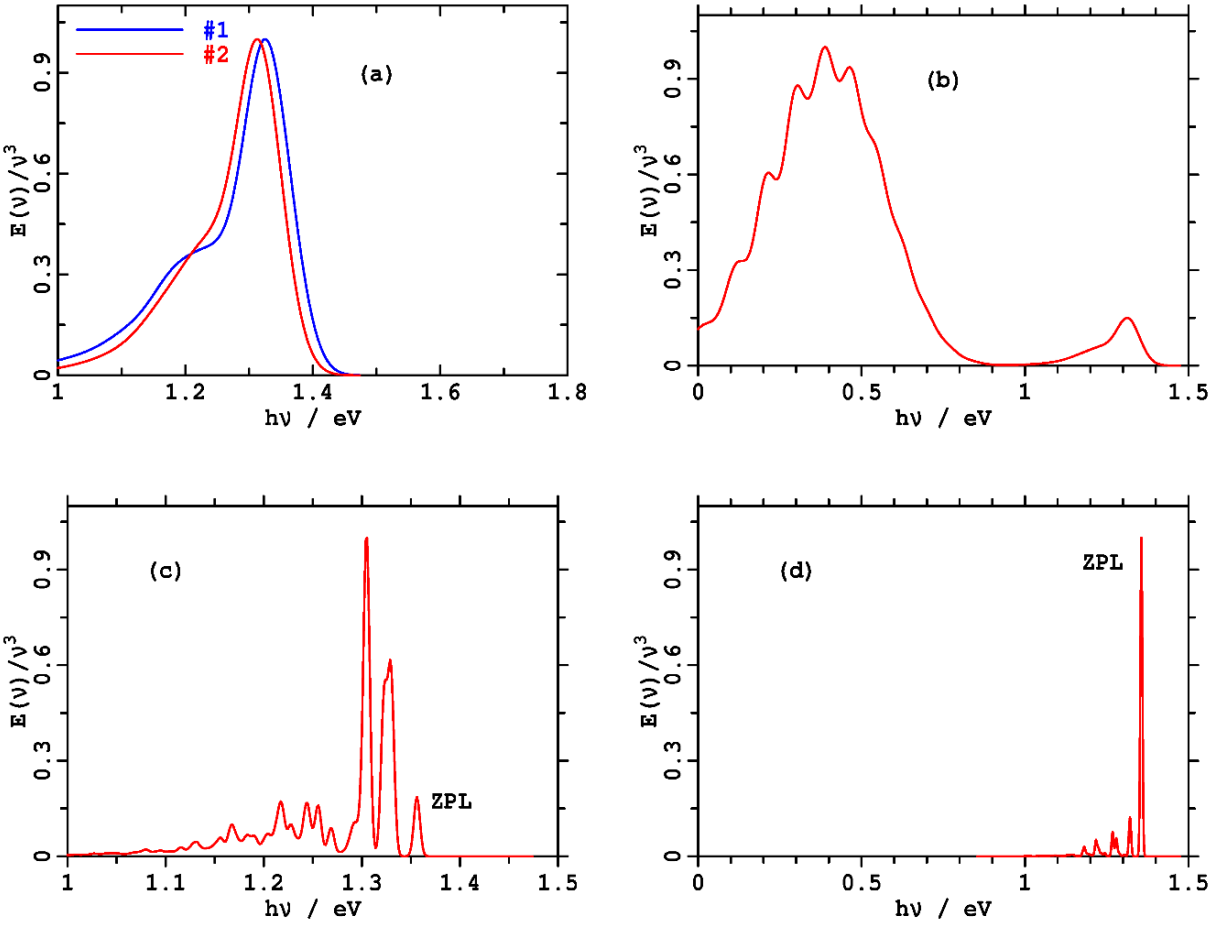

FIG. S13. Variants of calculated emission spectra in the singlet manifold at 77 K. (a) Models #1 and #2 from TABLE S19 in the spectral region observed experimentally. (b) The emission predicted by Model #2 extended down to zero energy. (c) The emission predicted by Model #2 shown in higher resolution, emphasising that Jahn-Teller spectra can appear very different from the form progression-based form anticipated by the Huang-Rhys model. (d) Model #2 varied by interchanging the ordering of the $(2)^1A_2$ and $(1)^1B_1$ components of the $(1)^1E''$ state.

Jahn-Teller effect need not show patterns at all reminiscent of the simple progressions envisaged by the Huang-Rhys model, there being no simple pattern between the energies of the ZPl and the phonon side bands. This is because the potential-energy surface is extremely anharmonic (FIG. S11) and facilitates quantum tunnelling between its three wells. Finally, FIG. S13(d) shows the emission predicted by a variation of Model #2 in which the ordering of the $(2)^1A_2$ and $(1)^1B_1$ components of the $(1)^1E''$ state is reversed. This makes the high-energy transition allowed and the low-energy one forbidden, reversing the pattern from FIG. S13(b). The emission then becomes extremely sharp. This goes to show just how sensitive spectra can be to the details of the Jahn-Teller surface. Whilst the Huang-Rhys approximation to the Jahn-Teller model for emission in the triplet manifold (Fig. 2) are somewhat similar, this is not a universally expected result.

Similarly, the simulated spectra are for the native out-of-plane intensity induced by the Jahn-Teller distortion. The selection rules change for Hertzberg-Teller transitions associated with vibronic mixing of the $(1)^1E'$ state into $(1)^1E''$, which, like that seen in the triplet manifold, is expected to be significant or even dominant. Again, whilst the change in selection rules manifested little consequence for the overall bandshape in FIG. S12 for the triplet manifold, this result would not necessarily apply to the singlet manifold.

S9. PHOTOCHEMICAL AND OPTICAL RATE PROCESSES

The accurate prediction of photoluminescence and photochemical rate processes is a challenging task, but order-of-magnitude estimates can readily be obtained using simple diabatic models for the potential-energy surfaces. Ignoring spectral bandwidth, photoemission lifetimes τ can be estimated from the associated rate constants k knowing the vertical emission frequency $\nu = E_v^E/h$ and associated oscillator strength f_{osc} using the Einstein equation

$$\frac{1}{\tau} = k = \frac{2\pi e^2}{\epsilon_0 m_e c^3}\nu^2 f_{osc} \text{ where } f_{osc} = \frac{2m_e M^2 \nu}{3\hbar^2}$$

and M is the electric transition dipole moment. The vertical emission energies are $E_v^E = \Delta E_0 - \lambda^E$ = 1.39 eV and 1.21 eV for the triplet and singlet manifolds, respectively, (Tables 3 and 4) with the calculated out-of-plane oscillator strengths being 6.9×10^{-5} and 5.8×10^{-4}, respectively (TABLE S16). This leads to triplet and singlet radiative lifetimes of 170 μs and 27 μs, respectively. However, emission can also occur through Herzberg-Teller allowed in-plane emission, including which calculations predict a revised triplet lifetime of 20 μs. Assuming the same enhancement, the singlet radiative lifetime is then estimated to be 3 μs. These values are shown on Fig. 6 and FIG. S14.

For intersystem crossing (ISC) processes involving transfer between the triplet and singlet manifolds, reaction rates at high temperature can be obtained from the Levich-Dogonadze equation [89] for non-adiabatic rate process

$$\frac{1}{\tau} = k = \frac{2\pi V_{SO}^2}{\hbar\left(4\pi\lambda k_\beta T\right)^{1/2}} \exp\frac{-\Delta E^\ddagger}{k_\beta T} \text{ where } \Delta E^\ddagger = \frac{(\Delta E_0+\lambda)}{4\lambda}$$

is the activation energy needed to reach the conical intersection, as determined by Kubo and Towozawa [90] and by Hush [91], and V_{SO} is the spin-orbit coupling, here evaluated at the available geometry closest to the conical intersection. The high-temperature limit applies when all important vibrational motions with frequencies have frequencies < 205 cm^{-1} at 295 K or < 54 cm^{-1} at 77 K. Based on the results presented in TABLE S17 and TABLE S18, such a limit clearly does not apply to the defects of concern. Whilst improved semiclassical approaches are available for which the required data is mostly already available, [92-96] cancellation of errors is known to render the more primitive approach to be widely applicable to room-temperature processes throughout chemistry, physics, and biochemistry (see e.g. [97]). Values of the parameters involved for the processes of interest herein are listed in TABLE S20, with the resulting lifetimes displayed in Fig. 6 for 77 K, whilst those calculated at 295 K are shown in FIG. S14. The spin-orbit couplings are evaluated using 1-ring MRCI(10,6)/6-31G*.

Finally, we consider internal conversion (IC) processes in which excitation is transferred between states within the same spin manifold. If there is no barrier to the reaction, then ultrafast relaxation will occur similar to energy relaxation within the one electronic state. Processes for which there is no barrier include relaxation from the optically allowed $(1)^3E'$ state excited by the incoming radiation. Excited-state vibrational analyses indicate that this state is not a local minimum but undergoes barrierless out-of-plane relaxation from $(1)^3A_1$ to $(1)^3A_2$ and from $(2)^3B_2$ to $(2)^3A_2$ (Table III, Fig. 6).

TABLE S20. Estimation of intersystem crossing lifetimes.

from	to	ΔE_0 / eV	λ / eV	V_{SO} / cm^{-1}	τ at 77 K	τ at 295 K
$(1)^1B_1$	$(1)^3A_1$	-0.14	0.20	4.1	150 ms	30 ns
$(1)^1B_1$	$(1)^3A_2$	-0.51	1.15	0.96	1.5 ms	150 ns
$(1)^3A_2$	$(1)^1B_2$	-0.99	1.25	2.1	4 ns	1.7 ns
$(1)^3A_1''$	$(1)^1B_2$	-1.29	0.21	0.068	10^{84} s	10^{17} s
$(2)^3A_2$	$(1)^1B_2$	-1.17	0.21	0.041	10^{65} s	10^{13} s
$(1)^1B_1$	$(2)^3A_2$	-0.33	0.72	0.012	33 ms	180 μs
$(1)^1A_1$	$(1)^3A_2'$	-1.00	0.30	0.42	10^{18} s	110 ms
$(1)^1B_2$	$(1)^3A_2'$	proceeds via $(1)^1A_1$			10^{23} s	1.8 s

Internal conversion between states that are both local minima on the potential energy surface is modelled using transition-state theory

$$\frac{1}{\tau} = k = \frac{k_\beta T}{h} \exp\frac{-\Delta E^\ddagger}{k_\beta T},$$

estimating the activation energy $\Delta E^\ddagger$ as before. Data and calculated lifetimes are summarised in TABLE S21 and displayed on Fig. 6 for 77 K, whilst those calculated at 295 K are shown in FIG. S14. For avoided crossings, this expression ignores the lowering of the transition-state energy associated with resonance between the reactants and products and hence underestimates reaction rates, in a way that is temperature dependent. For conical intersections, this expression overestimates reaction rates as it does not take into account the additional energy required for the reaction to circumvent the conical intersection. Test calculations indicate that this additional energy is likely to be small as strong mixing of wavefunctions is typically predicted as symmetry is lowered from that of the conical intersection.

TABLE S21. Estimation of internal conversion lifetimes.

from	to	pathway	ΔE_0 / eV	λ / eV	τ at 77 K	τ at 295 K
$(2)^1A_2$	$(1)^1A_2$	TS	-0.19	0.98	16 ms	85 ps
$(2)^1A_2$	$(1)^1B_2$	CI	-1.44	0.88	400 ns	5 ps
$(1)^1A_2$	$(1)^1A_1$	CI	-1.09	0.93	1.8 ps	0.2 ps
$(1)^1A_2$	$(1)^1B_2$	CI	-1.25	0.26	10^{49} s	30 m
$(1)^3A_2$	$(1)^3A_2'$	CI	-1.83	0.33	10^{99} s	10^{16} s
$(2)^3A_2$	$(1)^3A_2$	TS	-0.23	0.53	400 ps	0.9 ps
$(2)^3A_2$	$(1)^3B_1$	CI	-0.04	0.05	0.7 ps	0.2 ps
$(1)^3A_1''$	$(2)^3A_2$	TS	-0.13	0.06	14 ps	0.4 ps
$(1)^3A_1''$	$(1)^3A_2$	TS	-0.30	0.29	0.6 ps	0.2 ps
$(1)^3A_1''$	$(1)^3B_1$	CI	-0.14	0.09	1.8 ps	0.2 ps

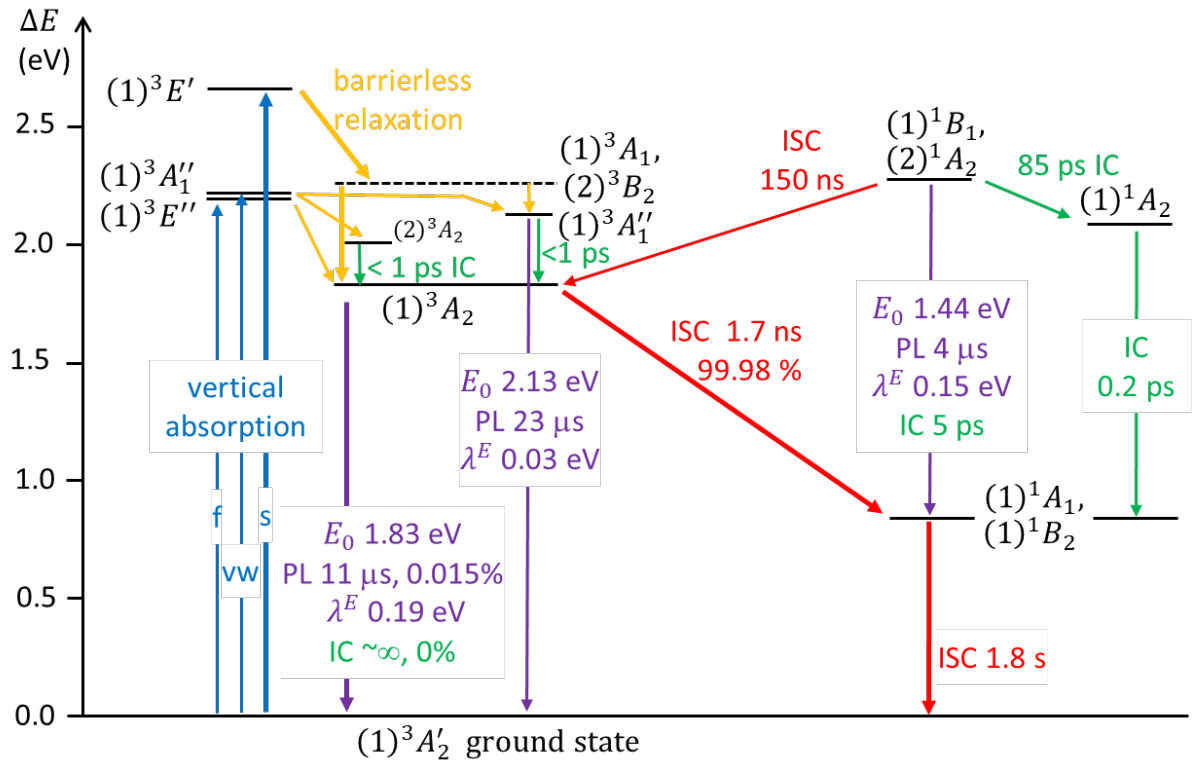

FIG. S14. Calculated photochemical and photoemission processes for the V_B^- defect of h-BN at 295 K, obtained using EOMCCSD calculations on the triplet manifold, DIP-EOMCC calculations on the singlet manifold, and MRCI-calculated transition dipole moments and spin-orbit couplings. Thicker arrows indicate the critically perceived processes during the photocycle. The indicated processes are: blue- vertical absorption (related absorption at lower energies down to the shown ZPLs and at higher energies will also occur, see Fig. S12), with Franck-Condon (Herzberg-Teller) allowed oscillator strengths in the ratio f:vw:s of 0(8):1:2000; orange- barrierless ultrafast relaxation to ZPLs; red- intersystem crossing (ISC), purple- photoluminescence (PL). Marked percentages indicate quantum yields. The energy levels and internal rate processes the doubly degenerate states that form transition states in C_{2v} symmetry are not shown, for clarity (see instead Fig. 4). States denoted with a solid line indicate that a local minima is established (triplet manifold) or believed (singlet manifold) to be involved, dashed lines indicate saddle structures that are unstable to out-of-plane distortion leading directly to $(1)^3A_2$. The use of different computational methods for the singlet and triplet manifolds appears to overestimate singlet-triplet splittings.

S10. ADDITIONAL SUPPORTING DATA AS ASCII TEXT

This data is located in file `supporting_data.zip`

A. Files ready to be read by spectroscopic simulation packages
These contain the initial state and final state nuclear coordinates, normal modes, Duschinsky matrices, and displacement vectors (hence Huang-Rhys factors and reorganisation energies) need to simulate spectra [88] using the Born-Oppenheimer, harmonic oscillator, and Franck-Condon approximations. All data is CAM-B3LYP/6-31G*

For the 2-ring compound:

```
dushin_13A2_13B1_curvi.log
dushin_13B2_11A1_recti.log
dushin_13B2_11A2_recti.log
dushin_13B2_11B1_recti.log
dushin_13B2_11B2_recti.log
dushin_13B2_13A1_curvi.log
dushin_13B2_13A2_recti.log
dushin_13B2_13B1_curvi.log
dushin_13B2_13B1_recti.log
dushin_13B2_21A2_recti.log
dushin_13B2_23A2_curvi.log
dushin_13B2_23B2_curvi.log
dushin_VB1-_13B2_13A2-recti.log
dushin_VB3-_13B2_13A2-recti.log
```

and for 1-ring and 3-ring compounds:

```
dushin_VB1-_13B2_13A2-recti.log
dushin_VB3-_13B2_13A2-recti.log
```

B. **Single file containing optimized coordinates**, energies, and free energies if available
`optimized_coordinates.txt`
containing data for:

```
3-ring D3h CAM-B3LYP/6-31G* (1)3A2' ground state
3-ring C2v CAM-B3LYP/6-31G* (1)3A2
3-ring C2v CAM-B3LYP/6-31G* (1)3B1
3-ring D3h CAM-B3LYP/6-31G* (1)3A1"
3-ring C2v CAM-B3LYP/6-31G* (2)3A2
3-ring C2v CAM-B3LYP/6-31G* (1)3A1
3-ring C2v CAM-B3LYP/6-31G* (2)3B2

2-ring D3h CAM-B3LYP/6-31G* (1)3A2' ground state
2-ring C2v CAM-B3LYP/6-31G* (1)3A2
2-ring C2v CAM-B3LYP/6-31G* (1)3B1
2-ring D3h CAM-B3LYP/6-31G* (1)3A1"
2-ring C2v CAM-B3LYP/6-31G* (2)3A2
2-ring C2v CAM-B3LYP/6-31G* (1)3A1
```

2-ring C2v CAM-B3LYP/6-31G* (2)3B2

2-ring C2v CAS(10,6)/6-31G* (1)3A2' ground state
2-ring C2v CAS(10,6)/6-31G* (1)1A1
2-ring C2v CAS(10,6)/6-31G* (1)1A2
2-ring C2v CAS(10,6)/6-31G* (1)1B1
2-ring C2v CAS(10,6)/6-31G* (1)1B2
2-ring C2v CAS(10,6)/6-31G* (2)1A1
2-ring C2v CAS(10,6)/6-31G* (2)1A2

10-ring D3h QM/MM CAM-B3LYP/6-31G*/AMBER (1)3A2' ground state
10-ring C2v QM/MM CAM-B3LYP/6-31G*/AMBER (1)3A2